

**A Single-Molecule Optical Trapping Assay: Measuring *E. coli* RecQ Helicase
Motion Using Force-Activated DNA Substrates**

by

Stephen R. Okoniewski

B.A., Northwestern University, 2013

M.S., University of Colorado, 2016

A thesis submitted to the
Faculty of the Graduate School of the
University of Colorado in partial fulfillment
of the requirements for the degree of
Doctor of Philosophy
Department of Physics

2020

This thesis entitled:
A Single-Molecule Optical Trapping Assay: Measuring *E. coli* RecQ Helicase Motion Using
Force-Activated DNA Substrates
written by Stephen R. Okoniewski
has been approved for the Department of Physics

Thomas Perkins, Department of Molecular, Cellular, and Developmental Biology

Meredith Betterton, Department of Physics

Loren Hough, Department of Physics

Joel Kralj, Department of Molecular, Cellular, and Developmental Biology

Deborah Wuttke, Department of Biochemistry

Date _____

The final copy of this thesis has been examined by the signatories, and we find that both the content and the form meet acceptable presentation standards of scholarly work in the above mentioned discipline.

Okoniewski, Stephen R. (Ph.D., Physics)

A Single-Molecule Optical Trapping Assay: Measuring *E. coli* RecQ Helicase Motion
Using Force-Activated DNA Substrates

Thesis directed by Professor Thomas Perkins, Department of Molecular, Cellular, and
Developmental Biology

In this thesis, I detail the work I have done in studying both force-activated DNA substrates and the RecQ DNA helicase from *E. coli*. The first half of the document introduces some background for these topics as well as the experimental methods used, with a focus on my high-precision single-molecule optical trap. In the chapter on force-activated DNA substrates, I explain the rationale for developing them, prior strides towards completing them, and then our work. Multiple substrate types are explored and validated, and several single-molecule helicase assays are done as proof of construct efficacy. The last chapter deals with my research on the single-molecule unwinding behavior of the RecQ helicase. The main focus of the chapter is optimizing my assay conditions so I can resolve single base-pair steps of RecQ, in order to better understand its fundamental stepping mechanics and see whether the kinetic models posed in previous papers are correct. I end the thesis by discussing some novel interactions between RecQ and its DNA substrate which lead to unexpected unwinding behaviors.

Dedication

I dedicate this thesis to my parents, Robert and Shirliann Okoniewski.

I love you guys.

Acknowledgements

I would first like to acknowledge the funding support I received during my graduate career. A CU/NIH Molecular Biophysics training grant (T32 GM-065103) funded me during my second and third years, and an NSF Graduate Research Fellowship (DGE 1144083) funded me during my fourth, fifth, and sixth years. In addition to financial support, these awards also provided valuable training and professional development opportunities. Thank you for the support you have given to my growth as a scientist and to the work described herein.

Thank you next to my advisor, Tom Perkins, without whom this thesis would not exist. His knowledge and experience in the many avenues of scientific life have been immensely helpful, as have his deep technical and communicative skills.

Thank you to Lyle Uyetake, our group's research technician, for all the talent and effort he put into creating the many DNA constructs and helicase proteins I used. Without his help, this work would have been so much more difficult.

Thank you to Rebecca Montange, the post-doc who first trained me in using our group's optical trapping instruments, wet lab protocols, and code base. Her assistance made my early days easier and her wry comments made them entertaining.

Thank you to the post-docs Rob Walder, Devin Edwards, and David Jacobson for serving as constant sources of advice and humor. And thank you again to Rob for spearheading the azide functionalization protocol. It improved the reliability of my DNA assays immensely.

Thank you to Matt Siewny and Patrick Heenan, my fellow graduate students in the group, for the advice and understanding they gave while we went through this process together. There really is nothing like someone going through the same stuff as you to give you solace.

Thank you to Arnulf Taylor, the junior graduate student I have trained to replace me. His hard work and dedication made the final days of my thesis easier, and I feel confident I'm leaving this project in good hands.

Thank you to the many undergraduates that have aided me in this work. Specifically, thank you to John van Patten and Ayush Adhikari for the long process of empirically converting Rob's azide protocol to my optical trapping coverslips, and for all the times they made azide coverslips for me. Thank you to Jaeyvn Faulk and Toby Bollig for the time they spent passing on the knowledge of how to create fiducial mark coverslips.

Thank you to JILA electronics shop wizard Carl Sauer for the many times he built and/or fixed the electronic components of my optical trapping instrument. He was a lifesaver. Thank you to JILA Keck Lab manager David Alchenberger for the clean room and SEM training he provided, and for the times he fixed various components of my instrument.

Thank you to Keir Neuman and Yeonee Seol at the NIH for generously providing me with RecQ protein aliquots and plasmids, as well as discussions on using and studying RecQ.

And lastly, thank you to Joe Falke and everyone involved in the Biophysics training program at CU Boulder. As previously stated, the many seminar and presentation opportunities provided by the program were instrumental to my scientific development, and the biophysics community that the program fostered has been a wonderful part of my time here.

Contents

Chapter

1	Introduction	
1.1	Single-molecule force spectroscopy and optical trapping	1
1.2	DNA mechanics and overstretching	6
1.3	RecQ family helicases.....	13
2	Experimental Methods	
2.1	Optical trapping instrument	20
2.1.1	Optical components	21
2.1.2	Detection Electronics.....	28
2.1.3	Software communication	31
2.1.4	Laser stabilization	33
2.1.5	Stage stabilization	37
2.2	Sample chamber manufacture.....	40
2.2.1	Single-channel flow chambers.....	40
2.2.2	KOH-etched coverslips.....	43
2.2.3	Fiducial mark fabrication.....	43
2.2.4	Azide functionalization.....	46

2.3	Biological assays.....	49
2.3.1	General DNA preparation	49
2.3.2	Tethered bead assay	51
2.3.3	RecQ helicase purification and preparation.....	52
2.4	Data collection and analysis.....	56
2.4.1	Bead position setting and calibration.....	56
2.4.2	Trap calibration and linearity.....	60
2.4.3	DNA tether centering and calibration	65
2.4.4	Overstretching assay	67
2.4.5	Active force-clamp assay.....	69
3	Force-activated DNA Substrates	
3.1	Introduction to force-activation	71
3.2	Validation of two force-activated DNA substrates.....	75
3.2.1	1002 nt 50% GC substrate	76
3.2.2	Hairpin-unwinding substrate.....	81
3.3	Single-molecule measurement of <i>E. coli</i> RecQ on-rate.....	86
3.4	Advanced substrates and %GC-dependent unwinding velocity assay	89
4	RecQ helicase unwinding	
4.1	The physical unwinding step size	97
4.1.1	Introduction to RecQ stepping.....	98
4.1.2	Optimizing optical trapping conditions	99

4.1.3	Optimizing biochemical conditions	111
4.1.4	Final RecQ stepping results	122
4.2	Unwinding “popping” behavior	130
4.3	Additional non-standard interactions of RecQ and DNA.....	140
Bibliography		147

Appendix

Acronym / Abbreviation Index	155
Protocols Index	159
Streptavidin to CML beads: Coupling Procedure	160
Cleaning Coverslips	162
Making HSQ Post Coverslips	163
Silane-PEG-Azide Functionalization Protocol	165
Tethered Bead Assay: DBCO Edition	166
RecQ Protein Purification	167

Figures

Figure

1.1	Aspects of optical trapping theory and application.....	4
1.2	The basic structure of DNA	8
1.3	DNA stretching and overstretching	11
1.4	The RecQ DNA helicase.....	16
2.1	Diagram of the pre-fiber optical setup for each laser	23
2.2	Diagram of the post-fiber optical setup	25
2.3	Labeled pictures of the microscope column and base	26
2.4	The electronic components of the optical trapping detection system.....	30
2.5	The operation of the AOM servo loop for reducing laser noise	35
2.6	Operation and results of the stage stabilization servo loop.....	39
2.7	Single-channel flow chamber and accessories.....	41
2.8	HSQ-based fiducial mark fabrication	45
2.9	Azide functionalization process and accessories	48
2.10	RecQ helicase purification gel	55
2.11	Procedures for positioning and calibrating a bead	58
2.12	Trap stiffness calibration and linearity	62
2.13	Surface-coupled geometry calculations and DNA centering.....	66

3.1	Introduction to force-activated DNA substrates	73
3.2	Forced dissociation of a 1002-nt DNA segment at ~65 pN.....	77
3.3	Quantifying force activation in the 50% GC construct.....	79
3.4	Challenges and solution to the 20-bp hairpin construct.....	82
3.5	Force activation of a DNA hairpin substrate	84
3.6	Determining the size of the activated hairpin	85
3.7	Force-activation enables an efficient single-molecule on-rate assay.....	88
3.8	Design and application of 120 bp force-activated hairpin substrates	93
3.9	66% GC unwinding velocities and validation	94
4.1	DNA mechanistic properties and step simulations	101
4.2	Surface-coupled geometry optimization	107
4.3	Optimizing the trap stiffness	109
4.4	RecQ processivity varies with [ATP]	112
4.5	RecQ interacts with non-hydrolysable ATP analogs.....	115
4.6	Slowing RecQ unwinding with ATP α S and divalent swaps.....	120
4.7	The <i>E. coli</i> RecQ helicase takes 1-bp physical unwinding steps.....	124
4.8	The high-resolution step size distribution strongly peaks at 1 bp.....	125
4.9	Fitting simulated magnetic tweezer steps	130
4.10	ATP-less RecQ popping of DNA hairpins.....	132
4.11	Quantifying the popping phenomenon.....	135
4.12	Structural implications of the popping behavior.....	137
4.13	RecQ can induce sharp extension drops prior to unwinding	141
4.14	RecQ can stall force-induced hairpin unzipping.....	144

Chapter 1

Introduction

1.1 Single-molecule force spectroscopy and optical trapping

The fundamental unit of life is the cell. From the smallest single-celled bacteria to the largest flora and fauna, all biological organisms are made up of these basic units. But these units are not simple. A single cell is an incredibly complex system of hundreds of millions of biochemical molecules (e.g., amino acids, nucleic acids, lipids, sugars, both alone and in higher-order structures) and hundreds of billions of chemical atoms and molecules (e.g., water, ionic salts, protons), all interacting with each other and the external environment. To understand the fundamental aspects of biology, these physiochemical components and interactions must be understood. The complexity of this task has given rise to many different scientific fields, each focusing on a slightly different facet of life's basic operation. For instance, many fundamental biological processes depend upon physical forces and motions between single biomolecules and biomolecular complexes. This is the purview of my field: single-molecule force spectroscopy.

Single-molecule force spectroscopy (SMFS) is a biophysical field that aims to understand the dynamics and energetics of biomolecular processes by mechanically manipulating individual biomolecules. Common topics in the field include investigating the polymer physics of biopolymers (*1-12*), the pathways and energy landscapes involved in secondary, tertiary, and

quaternary biopolymer structures (13-23), and the various aspects of molecular motor activity, including mechanical steps, kinetic rates, dynamic pauses, and stall forces (24-35). SMFS work is typically carried out using one of three instruments: optical traps, magnetic tweezers, or atomic force microscopes (AFM). Each has their own advantages, disadvantages, and preferred systems (36), but all three work off of the same idea: attach controllable probes to two ends of a biomolecule, and manipulate those probes to induce and record mechanical forces and extensions. To perform the work described in this thesis, I used an optical trapping instrument.

Broadly, an optical trap refers to any instrument capable of using light-based forces to trap objects in some region of 3D space. Many excellent reviews and books on the theory, construction, and operation of optical traps exist (37-43). Here I give only a broad outline of the basic theory, and later describe my particular instrument in detail (section 2.1). The first optical traps were pioneered by Arthur Ashkin and coworkers in the 1970s and '80s, culminating in the first single-beam gradient optical trap in 1986 (44). This type of optical trap (used in my instrument) is formed by tightly focusing a laser beam to a diffraction-limited spot. This creates a focus with a very high intensity (i.e., high electric field strength, since $I \propto E^2$) and a steep electric field gradient surrounding it (electric field strength quickly drops off in all directions). It is well-established that electric dipole moments are drawn towards regions of high electric field strength in order to minimize the total electric potential energy of the system, so long as the moment and field vectors align (Figure 1.1A, (45) Eq. 4.24). In other words, the electric potential energy at a point in space can be generally expressed as:

$$U = q\phi - \mathbf{p} \cdot \mathbf{E} + \dots, \quad (1.1)$$

where U is the electric potential energy, q is the net charge, ϕ is the electric potential, \mathbf{p} is the electric dipole moment, and \mathbf{E} is the electric field. It is also well-established that an

electromagnetic wave's oscillating electric field can induce electric dipole moments within dielectric objects, such that the moment and field vectors *always* perfectly align (so long as the dielectric object's refractive index is greater than the surrounding medium's index). This means that a tightly-focused laser beam will (a) induce oscillating dipole moments within any nearby dielectric object, and (b) draw the moments (and therefore the object) towards the beam focus (Figure 1.1B, left). The magnitude of this drawing force depends on the magnitude of the object's electric dipole moment and the magnitude of the electric field gradient near the focus. Because of this, the drawing force is often called the "gradient" force.

Dielectric objects can be trapped within the focal region if this gradient force is greater than any other forces on the object, including the scattering force due to radiation pressure from the laser beam and the thermal forces due to any external fluid medium (e.g., air or water). The point in space where an object becomes stably trapped is called the trap center. For a well-aligned laser beam, this trap center is located at the lateral center of the beam (collinear with the focal point), but just downstream of the focal point axially. This is because the average radiation scattering force is nonzero (unlike the thermal force), and pushes the dielectric object away from the focal point (which would be the true trap center if no scattering force was present) until the axial gradient force balances the scattering force (Figure 1.1B, right). If the trap is formed by focusing a collimated TEM₀₀ laser beam with a high numerical aperture (NA) objective lens, the electric potential energy of the trap will be 3D harmonic near the trap center. This means that, along each axis, the energy and force can be expressed as:

$$U_i = \frac{1}{2} k_i x_i^2 \quad F_i = -k_i x_i, \quad (1.2)$$

where i specifies the x , y , or z axis, x_i is the distance from trap center along that axis, F_i is the force, and k_i is a parameter called the trap stiffness. So long as a dielectric object stays within

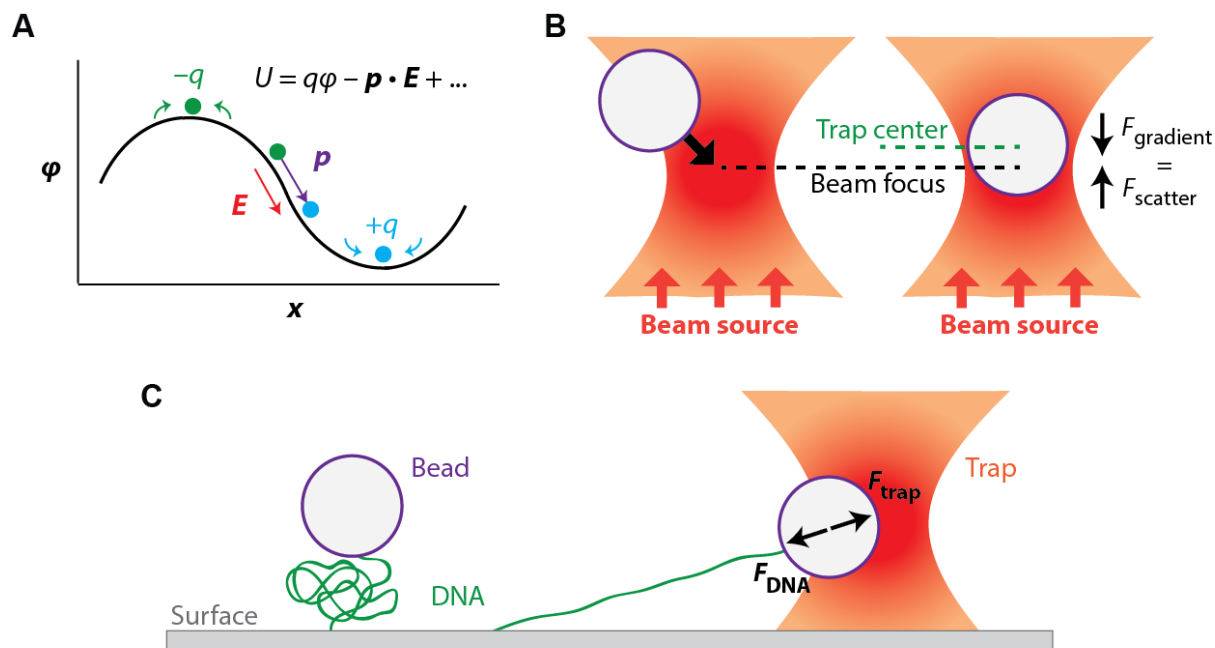


Figure 1.1: Aspects of optical trapping theory and application.

A) Example 1D plot of electric potential vs position, meant to intuitively demonstrate why electric dipoles seek regions of high electric field. To minimize the electric potential energy of the system, positive charges (blue) seek the lowest electric potential, while negative charges (green) seek the highest potential. Electric dipoles (purple) are composed of positive and negative charges, with the dipole vector pointing from negative to positive. To minimize energy, the positive part seeks low potential while the negative part seeks high potential. This can be optimally satisfied by aligning the dipole vector with the largest electric field vector (the negative gradient of the electric potential). B) Left: A tightly-focused laser beam will induce electric dipole moments within dielectric objects and draw them towards the high electric field of the beam focus (pulling the dielectric object along, as well). Right: For stable trapping, the gradient forces of the trap must be stronger than all other forces, including the scattering force due to beam propagation. This scattering force will push the object away from the beam focus until the axial gradient force equals it in magnitude, stably trapping the object and defining the trap center. C) Basic diagram of a surface-coupled optical trapping assay. Within a liquid medium, DNA molecules are bound to a glass surface at one end and a dielectric microsphere (bead) at the other. Thermal forces from the medium buffet both the bead and DNA, such that the lowest energy state is where the DNA adopts a compact, high entropy conformation (left). By trapping the bead and moving the stage relative to the trap, the DNA molecule can be manipulated and stretched. In this geometry, the average force on the bead from the trap is equal and opposite to the force on the bead from the DNA (from both entropic and enthalpic contributions). By knowing where both the surface and bead are at all times, the force and extension of the DNA can be measured.

the harmonic region of the trap (which usually extends at least 50 nm in all directions), its potential energy and force can be expressed simply through a constant and its distance from the trap center. Since this region produces a force that is linear with distance, it is also called the linear region of the trap (outside this region, trap stiffness is no longer constant with distance).

In biophysics applications, the most common object to trap in a single-beam gradient optical trap is a dielectric microsphere, typically shortened to simply “a bead”. By attaching one end of a biomolecule of interest to a fixed surface and another end to a bead, the molecule can be stretched and manipulated by trapping the bead within the optical trap (Figure 1.1C). Spheres are used because they are easy to manufacture and calibrate. This latter trait is especially important, since it is necessary to exert controlled, well-calibrated forces. As an example of the ease of use enabled by spheres, we can make a rough calculation to determine what variables affect an optical trap’s linear trap stiffness k . To begin, from Eq. (1.2) we know that the potential energy U_i along a specific axis can be parameterized by the trap stiffness k_i . From Eq. (1.1) we know that U_i at a point in space goes as $-(\mathbf{p} \cdot \mathbf{E})_i$. Say the dipole moment is induced in a dielectric sphere of refractive index n immersed in some medium of refractive index n_m . For a homogeneous external electric field \mathbf{E} , calculating this moment is a graduate-level exercise:

$$\mathbf{p}_o = 4\pi\epsilon_0 n_m^2 \left(\frac{b^2 - 1}{b^2 + 2} \right) r^3 \mathbf{E}, \quad (1.3)$$

where ϵ_0 is the electric permittivity of free space, $b = n/n_m$ is the ratio of the sphere and media refractive indices, and r is the sphere radius. The optical trap is certainly not a homogeneous \mathbf{E} field (if it was, there would be no trapping), but again this is only a rough calculation to obtain dependencies. Note that \mathbf{p}_o points in the same direction as \mathbf{E} only so long as $b > 1$, i.e. so long as the sphere has a larger refractive index than the surrounding medium (which for most SFMS

assays is water-based, so $n_m \cong 1.33$). In addition, we can combine Eq. (1.3) with Eqs. (1.1) and (1.2) to find trap stiffness dependencies:

$$|U_i| \propto (\mathbf{p} \cdot \mathbf{E})_i \propto \left(\frac{b^2 - 1}{b^2 + 2} \right) r^3 E_i^2 \propto \left(\frac{b^2 - 1}{b^2 + 2} \right) r^3 I_i \propto k_i. \quad (1.4)$$

Thus we find three variables that determine k : the trapped bead's volume (r^3), the polarizability of the bead's dielectric material relative to the medium ($b = n/n_m$), and the intensity of the laser beam (I). While studies have shown a more complex dependence between bead size and trap stiffness than the one above (46), up to a point it is true that large beads are better for exerting large forces. It also turns out that the linear proportionality between trap stiffness and laser intensity does hold in practice (section 2.4.2). With respect to dielectric material, polystyrene or silica beads are typically used, as they have n values larger than 1.33 and can be functionalized with many biomolecule attachment chemistries.

1.2 DNA mechanics and overstretching

In my optical trapping experiments, the tethered biopolymer is almost always DNA, or some modified form of DNA. Typically, "DNA" refers to double-stranded DNA (dsDNA), which is composed of two single-stranded DNA (ssDNA) polymers coiled around each other in a double helix configuration (Figure 1.2). The monomer unit for ssDNA polymers is the nucleotide, composed of a deoxyribose sugar, a phosphate group, and one of four nucleobases: adenine (A), thymine (T), cytosine (C), or guanine (G). Deoxyribose is a five-carbon sugar, and in a nucleotide the phosphate group and nucleobase are bound to the 5' and 1' sugar carbons, respectively (Figure 1.2, right). Within a single strand, the nucleotide units are joined by covalent phosphodiester bonds between the 5' phosphate group of one unit and the 3' hydroxyl group of the next. This results in a strong but flexible sugar-phosphate backbone, with all of the

nucleobases pointing outward. Note that a linear, finite strand of ssDNA will have a 5' phosphate group exposed at one end and a 3' hydroxyl group exposed at the other. By convention, we call the nucleotide with the exposed 5' phosphate group the first unit in the strand, and the one with the exposed 3' sugar the last. We read the base sequence in a strand by reading 5' to 3'. In a molecule of dsDNA, the bases between two strands noncovalently bind to each other, with A bases binding to T bases and C bases binding to G bases. Note that each strand runs reverse to the other, such that the 5' unit of one will bind to the 3' unit of the other. If the strands are perfect complements (every A/T/C/G base in one binds to a T/A/G/C in the other), then it is only necessary to specify the sequence of one of the strands in order to know the sequence of both.

The canonical A-T and G-C base pairs, also called Watson-Crick base pairs, are energetically favorable and stabilize the double helix structure. Part of that stability comes from the noncovalent bonds within the base pairs: A-T pairs form via two hydrogen bonds, while G-C pairs form via three (Figure 1.2, right). Base stacking interactions between the rings of nearest neighbor bases on the same strand provide a significant amount of additional stability. From these two mechanisms, G-C pairs provide the largest stability, while A-T pairs provide the least (47). On the other hand, non-canonical base pairs (anything not A-T or G-C) are energetically unfavorable and disrupt the structure. Much of this disruption is due to geometric constraints in the double helix. A canonical double helix has a constant diameter of 2 nm (48), since both A-T and G-C pairs have the same width. Non-canonical base pairs have a larger width, and thus protrude part of the backbone out from the rest of the helix, straining the structure. If too many are present (e.g., if the strands of the dsDNA did not anneal correctly), the helix will be too unstable to survive the constant thermal forces of the surrounding aqueous medium, and will fray apart into its component strands.

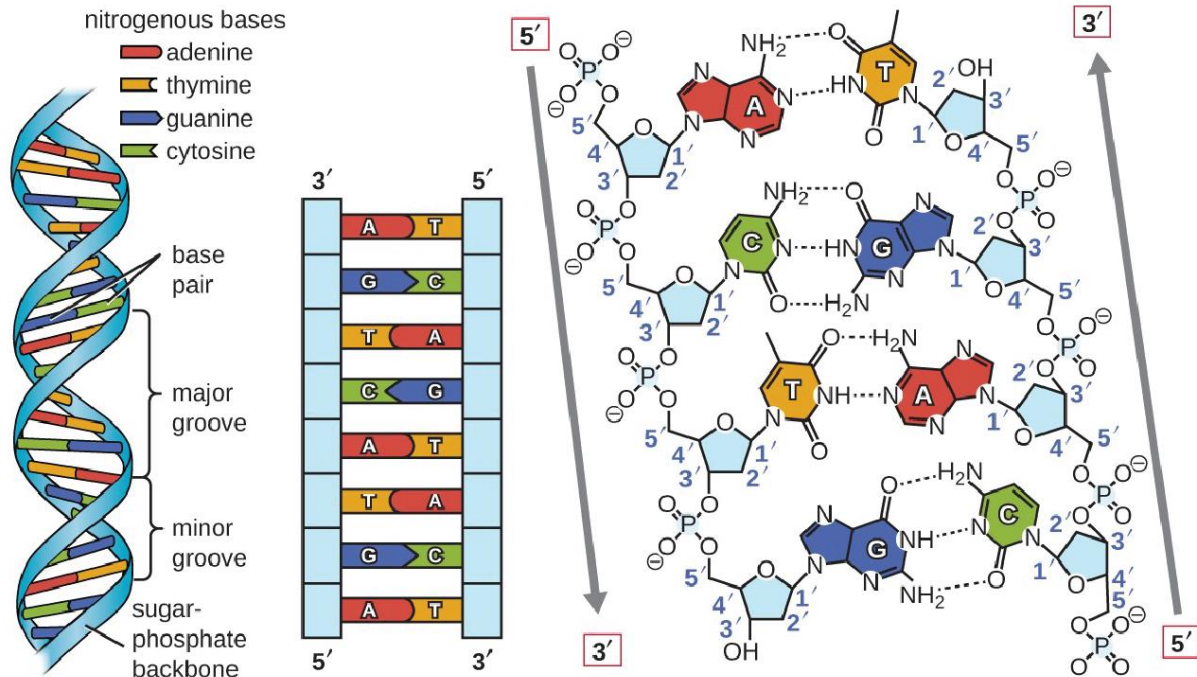


Figure 1.2: The basic structure of DNA.

Left: Double-stranded DNA is made up of two polymers of nucleotides noncovalently bound in a double helix. A nucleotide is made up of a phosphate group, a five carbon sugar ring, and one of four nitrogenous nucleobases (Adenine (A), Thymine (T), Guanine (G), Cytosine (C)). Each single strand of DNA is composed of a sequence of these nucleotides, and has a definite polarity (5' to 3'). Center: In a double helix, the strands run anti-parallel to each other, and ideally contain only Watson-Crick basepairs (A pairs with T and G pairs with C). Right: A more detailed picture of the chemistry involved in the double helix of DNA. Note that each phosphate in the backbone of DNA has a negative charge, which leads to the full strand being highly negatively charged. Reproduced from Figure 6 of Lumen's Open Education Resource for Microbiology: Structure and Function of DNA.

(<https://courses.lumenlearning.com/microbiology/chapter/structure-and-function-of-dna/>).

The polymer properties of dsDNA and ssDNA have been well-characterized and are critical for interpreting DNA-based data from an optical trap. The most important property is the average, zero-tension distance between adjacent monomer units, called the contour length (L_c). For dsDNA, the contour length specifies the average distance between adjacent base pairs (bp) (also called the helix rise). Early crystallographic studies clearly showed $L_c^{\text{dsDNA}} = 0.338 \text{ nm/bp}$ (49). For ssDNA, the contour length specifies the average distance between the backbone phosphate groups of the nucleotide (nt) monomer units (since the actual bases can rotate freely). Single-molecule studies have shown $L_c^{\text{ssDNA}} = 0.56 \text{ nm/nt}$ (3, 50). In addition, two other polymer properties are important for interpreting data: the persistence length (L_p) and the stretch modulus (S). The persistence length characterizes the bending stiffness of a polymer, and is reported as the average, zero-tension distance at which two units cease to be directionally correlated. For the negatively charged dsDNA and ssDNA polymers (each phosphate group has $-1e$ charge), L_p depends on the temperature and ionic conditions surrounding the polymers. At standard salt and temperature conditions ($\sim 150 \text{ mM}$ monovalent and $25 \text{ }^\circ\text{C}$), $L_p^{\text{dsDNA}} = 50 \text{ nm}$ (2, 7) and $L_p^{\text{ssDNA}} = 0.75 \text{ nm}$ (3, 50). The stretch modulus characterizes the enthalpic stiffness of a polymer, i.e. how difficult it is to forcefully stretch a polymer beyond its zero-tension contour length, and is reported as a characteristic force. At standard conditions, $S^{\text{dsDNA}} = 1200 \text{ pN}$ (5, 7) and $S^{\text{ssDNA}} = 800 \text{ pN}$ (3, 50).

These polymer parameters are used in mathematical models that relate the force (F) exerted on a biopolymer to its resulting extension (x). For dsDNA, the most common model is the extensible worm-like chain (eWLC). From (5), it is given as:

$$F = \frac{k_B T}{L_p} \left(\frac{x}{L_c^T} - \frac{1}{4} - \frac{F}{S} + \frac{1}{4 \left(1 - \frac{x}{L_c^T} + \frac{F}{S} \right)^2} \right), \quad (1.5)$$

where k_B is Boltzmann's constant, T is the temperature, and L_c^T is the total contour length of the polymer, i.e. L_c multiplied by the number of monomer units in the polymer. Above $F = 2$ pN, the above expression can be approximated to a simpler one (which I often use) (5):

$$x = L_c^T \left(1 - \sqrt{\frac{k_B T}{4L_p F} + \frac{F}{S}} \right). \quad (1.6)$$

This expression has the benefit of being an explicit function $x(F)$, as opposed to the implicit function $F(F, x)$ in Eq. (1.5). For ssDNA, an eWLC model or the extensible freely-jointed chain (eFJC) model can be used successfully (51), so long as one does not mix parameters between the two. I use eFJC models for my data, and from (3), the model is given as:

$$x = L_c^T \left(\coth \left(\frac{2L_p F}{k_B T} \right) - \frac{k_B T}{2L_p F} \right) \left(1 + \frac{F}{S} \right). \quad (1.7)$$

These models can fit the force-extension data collected in an optical trap, and thereby interpret its biological meaning. However, it is important to keep in mind that these models do have their limitations and quirks. For example, when the force-extension curve from a moderate length dsDNA or shorter (≤ 1.5 μm total contour length) is fit by the eWLC model, the model will often report L_p values smaller than expected (11). This is a model quirk, and does not represent any true change in the polymer's persistence length.

These polymer models also have limited ranges of applicability. For example, the eWLC model for dsDNA only works up to ~ 35 pN (Figure 1.3A), capturing the low-force entropic stretching (0-10 pN) and the medium force enthalpic stretching (10-35 pN). Specifically, when the two polymer endpoints are fixed close together (low extension), the polymer can adopt many

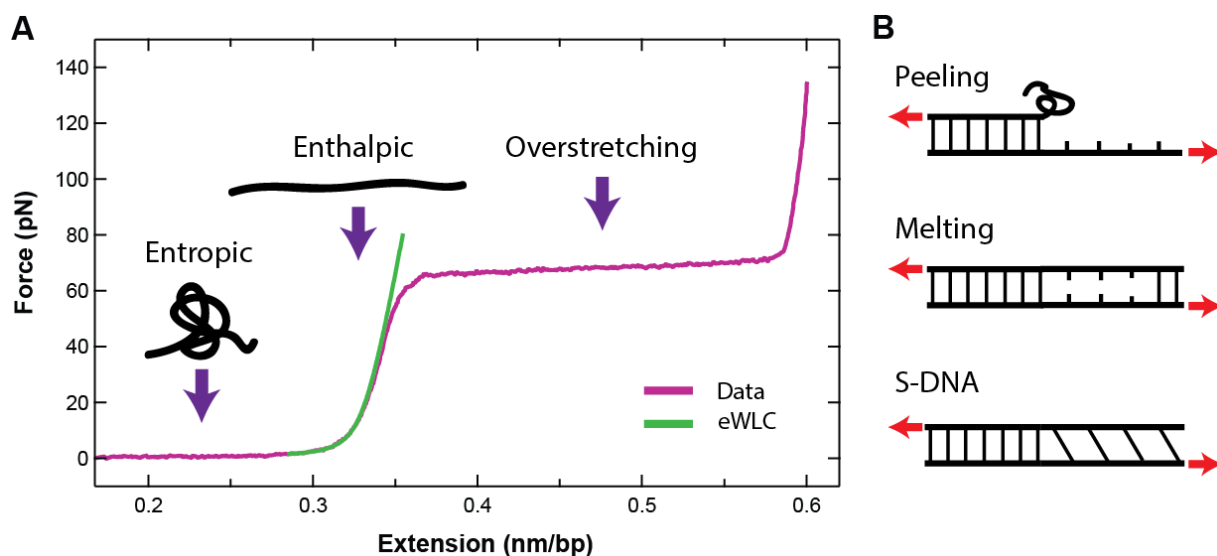


Figure 1.3: DNA stretching and overstretching.

A) Force-extension curve for dsDNA. When there is no external force applied across a DNA polymer, it will adopt a tangled, condensed form in solution, maximizing its entropy. It takes very little applied force to stretch the polymer in this entropic regime, and so the force-extension curve is very nearly flat. As the extension of the DNA nears its contour length (0.338 nm/bp), further stretching becomes more difficult, and the necessary force begins to rise dramatically. In this enthalpic regime, the polymer has no entropic freedom, and further pulling stretches chemical bonds within the structure. Below ~ 35 pN, this behavior is well-described by the eWLC polymer model. As the force reaches ~ 65 pN, the polymer undergoes a dramatic overstretching event, where the extension rapidly grows by 70%. After this transition finishes, a second enthalpic regime begins and continues until the dsDNA strands peel apart or a chemical bond breaks. B) The three mechanisms of DNA overstretching. Red arrows indicate where the tension is being applied. If free ends or nicks are present in the polymer, the strands will begin to peel apart. This conversion of dsDNA into ssDNA is what causes the extension increase in overstretching. If no free ends or nicks are present, bases can either internally melt apart or rearrange themselves into a new, extended form (S-DNA). Both of these mechanisms also increase the extension to largely the same degree.

coiled-up configurations (high entropy). This allows it to easily absorb the buffeting thermal forces of the aqueous medium, leading to low forces exerted on the fixed endpoints. As the two ends are moved further apart, the polymer can adopt fewer configurations (low entropy), and so thermal forces are transmitted more fully to the endpoints. Correspondingly, more external force is required to keep the endpoints from moving. Once the tether is pulled nearly straight, continued pulling stretches the base stacking interactions and backbone chemical bonds of the dsDNA molecule (enthalpic stretching), requiring large increases in force for small increases in extension. The eWLC model predicts that this continues on indefinitely, but dsDNA only follows this behavior up to ~ 35 pN. Past this point, the molecule actually begins to soften (more extension for less force), due to coupling between the actual stretching and helical twisting induced by the stretching. Applying a correction for this effect to the eWLC enables accurate modelling up to ~ 60 pN (52).

In the 60-70 pN range, a dsDNA molecule undergoes an incredible increase in extension, stretching up to 1.7x its total contour length with little increase in force. This phenomenon, first observed in 1996, is called the overstretching transition of dsDNA (3, 4). It took two decades of further research to reach the consensus that three separate mechanisms are responsible for overstretching (53-63) (Figure 1.3B): (i) the peeling apart of dsDNA into ssDNA from free ends or nicks, (ii) the internal melting of base pairs within the dsDNA, and (iii) the conversion of dsDNA into a new structural configuration called S-DNA ("normal" dsDNA is also called B-DNA). Which mechanism(s) take place during the transition depends on the temperature and salt conditions surrounding the dsDNA molecule, as well as its topological structure. For example, at standard temperature and salt conditions (~ 25 °C and 150 mM monovalent), a molecule will undergo the peeling mechanism if any free ends or nicks (backbone breaks) are present (59-61).

Near these spots, base pairing and base stacking interactions begin to destabilize and dissolve due to the high tension, allowing one strand of the double helix to peel away and leave the remaining one under tension. Continual peeling and conversion of dsDNA into ssDNA causes the dramatic extension increase. If the dsDNA molecule is topologically closed (i.e., does not have free ends or nicks), peeling is prohibited. With this configuration and high temperatures (~37 °C), the base pair destabilization induced by the force still occurs, but now both ssDNA strands remain under tension, sharing the load (60, 61). Alternatively, under standard conditions and closed topology, the force destabilizes base interactions enough for them to shift and reform into a new, extended S-DNA conformation (the form of which is still debated) (60, 61).

1.3 RecQ family helicases

Within a cell, DNA is continually acted upon by a multitude of proteins. Structural proteins organize and de-organize the DNA into higher-level structures like nucleosomes and chromosomes. Replication proteins copy the DNA so that its genetic code can be included in both copies of a dividing cell. Transcription proteins process the DNA genetic code into RNA molecules that either get translated into proteins or serve their own roles in the cell. And critically, repair and recombination proteins remove damage from DNA, allowing all of the proteins above to perform their functions normally. There are many families of repair proteins, each of which specialize in addressing certain kinds of DNA damage. The protein family of interest to this study is the RecQ helicase family.

The RecQ family is a set of proteins conserved from bacteria to humans which unwind the complex, intermediate DNA structures that form during many processes used to maintain the genome (64-66). For example, they are known to play a critical role in multiple steps of

homologous recombination, a repair process for an often-lethal type of DNA damage called double-stranded breaks, where nicks in both backbone strands lead to the molecule fissuring into two separate parts. Due to their important DNA repair role, mutations in human RecQ helicases are associated with a number of diseases (e.g., Bloom, Werner, and Rothmund-Thomson syndromes) which, among other symptoms, lead to cancer predisposition and premature aging (64-66). Thus, the RecQ helicase family, one of the major families that make up the SF2 helicase superfamily (67-69), is both biologically important (malfunction causes disease) and functionally complex (unwinding of multiple DNA substrate types). Of the dozen known enzymes in the RecQ family, the one most of interest to this study is the founding member from *Escherichia coli*, simply called RecQ.

Functionally, RecQ is an ATPase and 3' to 5' DNA helicase, meaning it hydrolyzes molecules of ATP for energy and unwinds dsDNA by moving along one of the strands in a 3' to 5' direction (70). Early biochemical studies showed that RecQ has ATPase activity on circular and linear ssDNA (meaning that it can translocate along ssDNA, as well) and can unwind blunt end dsDNA at high concentrations (70). It is a mildly processive helicase, in that it can unwind on the order of 100 bp before dissociating from the polymer (71, 72). A cell mutation study showed that RecQ activity suppresses illegitimate recombination in *E. coli*, and that other recombination pathways cannot fix the problems caused by removing RecQ (73). A suite of biochemical studies found that at 37 °C and low salt concentration, RecQ initiates and disrupts recombination events (together with RecA and SSB), and forms D-loop and Kappa DNA intermediates (74); nucleates, unwinds, and catenates covalently closed circular DNA at high concentrations with the aid of Topo III (75); and displays varying large-scale unwinding activity depending on ATP, Mg²⁺, and SSB concentrations (76).

The first RecQ crystal structure was published in 2003 using a truncated variant called RecQ^{AH} (77). It showed that RecQ is a multidomain protein with a catalytic core composed of a pair of RecA-like domains, followed by RecQ-family-specific auxiliary domains: a zinc-binding domain and a winged-helix domain. The final domain of RecQ, the helicase-and-RNaseD-C terminal (HRDC) domain, had to be removed for the original crystallization but was later crystallized separately (78) (Figure 1.4A). The two RecA-like domains are common to the SF1 and SF2 helicase superfamilies, and are used for ATP hydrolysis and ssDNA translocation (67, 68). A high degree of conformational flexibility has been observed between the two domains, specifically during different steps of the ATP hydrolysis cycle (79) (Figure 1.4B). The domains are observed to rotate relative to one another along an axis defined by the ATP binding cleft; it is thought that this rotation is how the helicase steps along ssDNA, transducing ATP energy into “inchworm” translocation. The mechanics of this translocation for 3’ to 5’ SF1 helicases are known: the HD2 domain remains tightly bound to ssDNA during the ATP binding step of the kinetic pathway. This causes the ssDNA to slide across the HD1 domain during the subsequent rotation caused by ATP binding, and puts the domain in a position to bind a downstream nucleotide. After the hydrolysis step of the pathway, it does exactly that, tightly binding the nearest nucleotide while HD2 domain releases its previous nucleotide and binds a nearer one. Through this process inchworm steps are taken (79). Later studies expanded on these structures to show that in RecQ an aromatic-rich loop couples ATPase and translocation activities in the catalytic core (80) and that the winged-helix domain serves as a binding pocket for SSB (81, 82), in addition to modifying core activity.

Recently, crystal structures of RecQ family proteins bound to DNA substrates have been obtained, a daunting task for the last two decades (79, 83, 84). While *E. coli* RecQ has still not

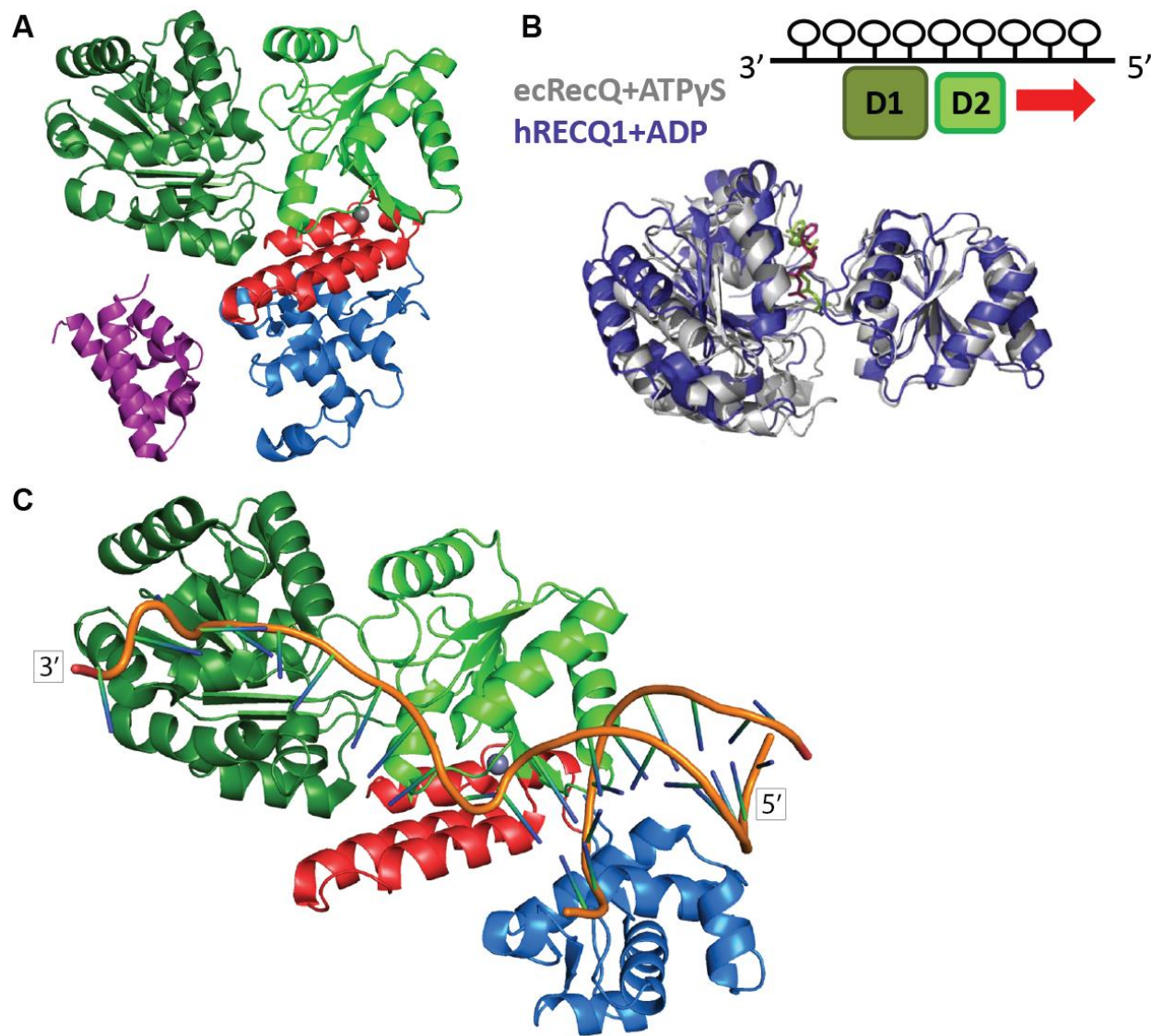


Figure 1.4: The RecQ DNA helicase.

A) The structure of RecQ^{ΔH} (PDB 1OYW) and its HRDC domain (PDB 1WUD). Full RecQ has never been crystallized. The two RecA-like motor core domains are dark and light green, the zinc-binding domain is red, and the winged-helix domain is blue. The zinc ion appears as a grey sphere with the zinc-binding domain. B) RecQ translocates along ssDNA in the 3' to 5' direction through an ATP hydrolysis cycle. Two motor core structures are shown: *E. coli* RecQ with ATP γ S bound (grey; PDB 1OYY) and human RECQ1 with ADP bound (purple; PDB 2V1X). Figure reproduced from Vindigni et al., 2010 with permission from Elsevier. These structures show how the left domain (D1) of the motor core changes between the ATP and ADP phases of the hydrolysis cycle, relative to the D2 domain. This motion drives RecQ translocation. C) The crystal structure of *C. Sakazakii* RecQ bound to a forked DNA substrate. The winged-helix domain undergoes a conformational change to bind the dsDNA portion of the substrate, while the ssDNA portion appears to be pulled away at a 90° angle (PDB 4TMU).

been crystallized with a substrate, another bacterial RecQ from *C. sakazakii* has been crystallized with a forked ss-dsDNA substrate (83). The catalytic core of this protein (CsRecQ^{ΔH}) has ~86% sequence homogeneity to EcRecQ^{ΔH}, making it the closest homolog to *E. coli* RecQ in the RecQ family. Interestingly, the protein appears to bind its substrate by rotating its winged-helix domain and keeping the DNA fork bent at ~90° (Figure 1.4C). Unlike many other helicases, including some RecQ family proteins, there is no beta-sheet hairpin or other structural motif present to aid unwinding. Thus, dsDNA unwinding seems to occur only due to the tension placed across the double helix as the RecA-like domains pull it out of the binding pocket via its attached ssDNA. The mechanistic implications of this structure are still being explored.

One topic of interest for *E. coli* RecQ is whether it binds and unwinds DNA as a monomer (single protein) or multimer (many connected RecQ proteins working in concert). The first paper on the topic found that at 0 mM monovalent and 1 mM divalent salt, high temperature (37 °C), and high concentration (100 nM), RecQ helicase activity is cooperative with ATP concentration (Hill coefficient 3.3), indicating a multimer of at least three helicases (76). However, a different group found that between temperatures of 4–37 °C and up to concentrations of 20 μM, RecQ exists as a monomer both in solution and during unwinding (85-87). A later collaboration between this group and another lab found RecQ monomers have a “functional” cooperativity at 37 °C and modest-to-no cooperativity at 25 °C; this functional cooperativity can result in Hill coefficients greater than 1 despite the sole presence of RecQ monomers (88). However, the first group revisited the subject, found a Hill coefficient of 2.1 for ssDNA translocation activity, and then posited that translocation requires at least a dimer (89) (with no discussion of the result of (88)). In a recent paper, they also assert that unwinding involves a host of multimeric species (90). Thus, the multimeric status of RecQ is still an active area of research.

Another topic of interest is the fundamental physical, chemical, and kinetic step sizes of RecQ during ssDNA translocation and dsDNA unwinding. The physical step size of a helicase is defined as the physical distance it travels during a single reproducible cycle of motion. For translocation, this means the number of nt it can stably step across, and for unwinding this means the number of bp it unwinds. The chemical and kinetic step sizes are defined similarly, but instead of being per cycle-of-motion, they are explicitly per ATP hydrolyzed and per rate-limiting step of activity, respectively. Whether or not these three values are the same or different depends on the helicase. The first bulk measurement of the unwinding chemical step size of RecQ found a value of 1 bp (87) (corrected from their original result of 4 bp). Other bulk studies found that both the translocation and unwinding chemical step sizes are very close to 1 (71, 72). However, there have been observations of a 5 bp kinetic step size for RecQ, the detailed mechanics of which are still unknown (91). In addition, a recent single-molecule FRET assay gave the first measurement of RecQ's unwinding physical step size. Contrary to expectations, this assay appeared to show RecQ taking steps of multiple sizes, from 0.5 bp to 3.5 bp (92). Thus, finding the true unwinding step size of RecQ is still an active area of research.

The dynamic stepping behavior of RecQ is also an active area of research, and includes phenomena of interest such as the pauses taken during unwinding, the potential for backsliding on DNA substrates, the prevalence of strand switching during unwinding, and the effects that substrate geometry, RecQ mutations, and buffer conditions have on the above. For instance, a recent magnetic tweezers study showed that the HRDC domain induces significant pausing on hairpin substrates, but only minor pausing on gapped, linear substrates (while not affecting the instantaneous unwinding rate at all) (93). Strand switching, where a single RecQ moves along one strand of a dsDNA substrate only to abruptly transfer over to the other strand, is posited to

be an important mechanism for how RecQ rescues stalled replication forks (94). It is expected that precise single-molecule methods like optical traps will be able to further elucidate these dynamic phenomena, which are difficult to observe using classical ensemble assays.

Especially important to this work are the similarities and differences between native RecQ and the truncated protein RecQ^{ΔH}. As stated above, the HRDC domain induces pauses of varying intensities, meaning that the truncated RecQ^{ΔH} experiences fewer pauses and thus has a higher mean unwinding rate than its native structure. RecQ^{ΔH} also has ~2x higher ATPase activity and ~3x lower ssDNA binding strength than native RecQ (72, 93). On the other hand, the ssDNA binding on-rate is roughly the same between the two (95), as well as the coupling stoichiometry, processivity, and instantaneous unwinding rate (72, 93).

Chapter 2

Experimental techniques

In this chapter, I detail the experimental techniques I used in my thesis work. First, I go through the basics of my surface-coupled optical trapping instrument, including the active stabilization methods used to give it sub-nm precision (section 2.1). Next, I cover the fundamental part in all of my samples, single-channel flow chambers, including the various ways we treat and modify coverslip surfaces (section 2.2). This is followed by the biological work that goes into readying biophysical experiments, including DNA preparation and tethered bead assays (section 2.3). Finally, with the instrument and samples explained, I detail the process of performing an experiment, including the alignment and calibrations needed as well as my basic measurement assays (section 2.4).

2.1 Optical trapping instrument

In this section, I give a basic overview of my optical trapping instrument. I first go through the optical components that make up the majority of the physical instrument, including the lasers, the free-standing optical elements, and the inverted microscope in which experiments are performed (section 2.1.1). I next detail the detection electronics, including the quadrant photodiodes (QPDs), the JILA electronic boards, and the National Instruments (NI) data acquisition

electronics that communicate with the instrument's computer (section 2.1.2). I then cover the NI software used to collect data and control the various parts of the instrument (section 2.1.3). Finally, I explain in detail the operation of the servo loops used for laser stabilization (section 2.1.4) and stage stabilization (section 2.1.5).

Note that all of the instrument components are located in an acoustically quiet basement room (NC30) that is temperature regulated (± 0.2 °C) with its own separate airflow. The temperature is typically set to 22 °C. All of the free-standing optical components are installed inside plexiglass boxes on floating optics tables to insulate them against environmental noise. All of the electronic boards are mounted in and powered by a NIM rack.

2.1.1 Optical components

The first components pertinent to the instrument are the lasers we use for trapping and detection. The trapping laser beam is generated by a solid-state neodymium-doped yttrium orthovanadate (Nd:YVO₄) laser (Spectra-Physics, Millennia IR, $\lambda = 1064$ nm, 10 W). For high power and lasing stability, the laser is set to operate at 7.8 W output power (7.77 W set on the laser controller). For additional intensity stability, the cooling system in this laser was modified: the internal fan was replaced by an 18.6 L/s external fan (connected via custom-built air ducts) that operates continuously instead of in cycles. The laser emits a single-mode, Gaussian TEM₀₀ beam; this mode is ideal for trapping, as it can be focused to the smallest diameter beam waist, and therefore produces the strongest, most harmonic trap. Two diode lasers are used to produce the detection laser beams for the instrument. A $\lambda = 808$ nm laser (Lumics, 100 mW) makes the beam that monitors the position of optically trapped objects, and a $\lambda = 845$ nm laser (Lumics, 200 mW) makes the beam that monitors the position of fiducial marks on the coverslip surface of

the sample chamber. Lab tradition refers to these lasers as the 810 nm and 850 nm, respectively. Both diode lasers are operated via custom-built electronic temperature/current controller boxes, which are primarily used to set the diode current in each laser and stabilize the diode's temperature. The beams of both lasers are sent through fiber Bragg gratings to increase their wavelength stability and optically isolate them from back reflections, such that they both emit a single-mode TEM₀₀ beam. The wavelengths of these three lasers were chosen for their commercial availability, relative transparency in water, biological safety, and band separation. This last characteristic is critical, given that all three beams have to be combined and later separated using dichroic mirrors.

Since lasers often emit beams which are not fully linearly polarized, the polarization of each beam is purified directly after emission using a half-wave plate and a polarizing beam splitter (PBS) cube. PBS cubes reflect one direction of linear polarization and transmit the other, so we use a half-wave plate to shift the polarization of the laser output so that maximum power is put into our direction of choice (Figure 2.1; transmitted for the diode lasers, reflected for the trapping laser). This fully polarized beam is then sent into an acousto-optic modulator (AOM), the fundamental component of the active stabilization loop that reduces laser noise and sets the final laser intensity in the sample plane. The servo loop will be covered in more detail in section 2.1.4. For now, it is enough to know that the AOM acts as a tunable diffraction grating that outputs a 1st-order beam of variable power. This beam is coupled into the rest of the system while the 0th-order and higher order beams are discarded. Each laser beam is then coupled into a polarization-maintaining fiber-optic patch cable (OZ Optics) using a converging lens and a 5-axis ultra-stable fiber coupler (Thorlabs PAF-X-5-B). This cable, another part of the AOM servo loop, propagates the beam to the main part of the optical setup.

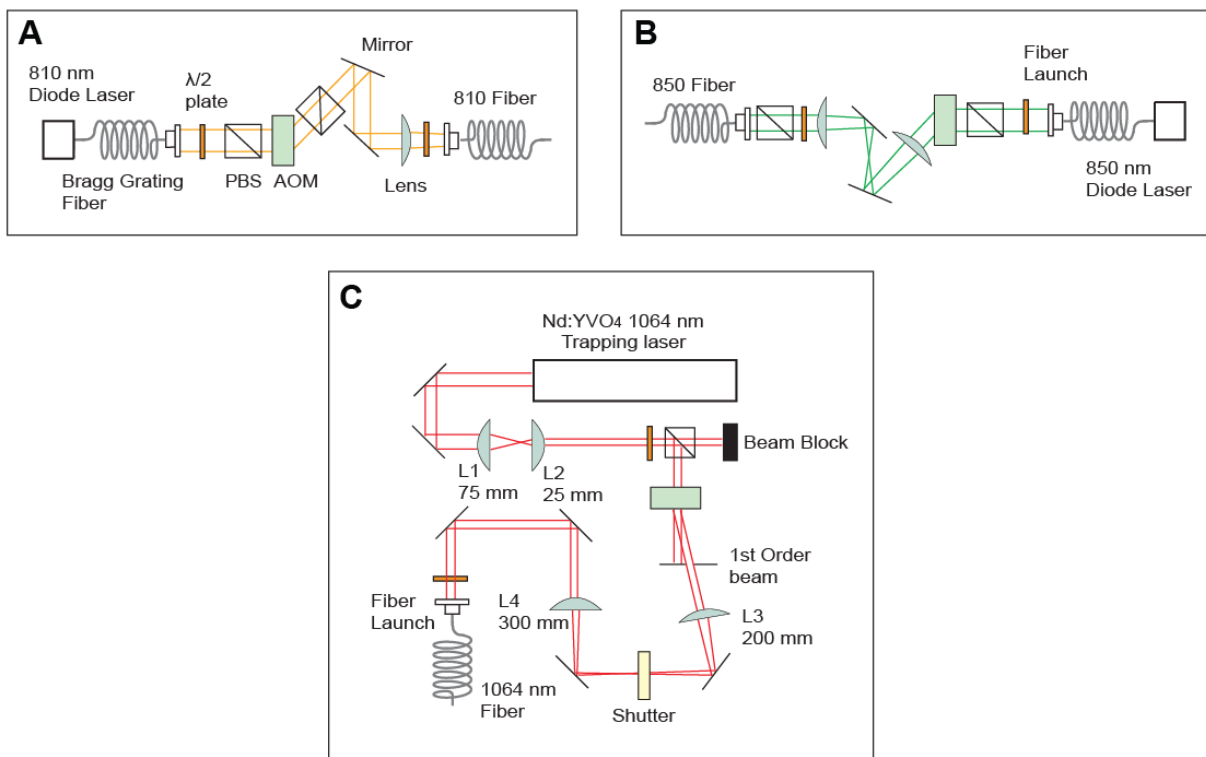


Figure 2.1: Diagram of the pre-fiber optical setup for each laser.

A) The 810 nm bead detection laser setup. B) The 850 nm post detection laser setup. C) The 1064 nm trapping laser setup. Note the 850 nm and 1064 nm beams are resized using two-lens telescopes. Additionally, all beams are focused onto their fiber launches to mitigate pointing noise, especially the 1064 nm beam. This figure was taken and modified from Figure 2.1 of Amanda E. Carpenter's thesis from the Perkins lab. Acronyms: AOM (acousto-optic modulator), PBS (polarizing beam splitter).

Each beam is launched out of its fiber-optic patch cable using a free-space fiber launch system (Thorlabs KT110). A converging lens and PBS cube are rail-mounted to this system; the lens recollimates the beam and the PBS cube repolarizes it. Each beam is then passed through a 90/10 beam sampler, so that 10% of its power is sent into an analog PIN photodiode detector for the AOM servo loop (Figure 2.2). The 1064 nm and 810 nm beams are then passed through electronic shutters which can quickly block or unblock the beams. Likewise, the 1064 nm and 850 nm beams are reflected off of electronically controllable PZT mirrors (PI S330.2SL PZT mounts) so that their positions within the sample plane can be precisely adjusted (the 810 nm beam is kept fixed in the sample plane, and is used as a point of reference). All three beams are then combined together using dichroics, passed through a two-lens telescope to resize their beam widths, and sent into an inverted microscope (Nikon TE2000-S). Entry into the microscope forms a sort of dividing line within the instrument. Everything before it, including the as-yet described AOM servo loops (section 2.1.4), all serve to produce three laser beams with minimal intensity, mode, position, and polarization noise, whose intensity and position can be precisely changed by the experimenter. Those three beams are the sole outputs of this section of the instrument, and they now act as inputs into the microscope section.

A diagram of the critical microscope components is given in Figure 2.2, while a labeled picture of the microscope is given in Figure 2.3. The microscope's base and condenser column are reinforced with custom-built monolithic aluminum slabs to improve their mechanical stability. Additionally, custom-built monolithic parts are used as reinforced mounts for the objective lens and sample stage. The objective lens is an oil immersion, high numerical aperture (NA) lens (Nikon CFI Plan Apochromat 100x oil IR, 1.4 NA, working distance 0.13), as is the condenser lens above the stage (1.4 Nikon HNA Oil). The sample stage is a 3-axis PZT stage (PI

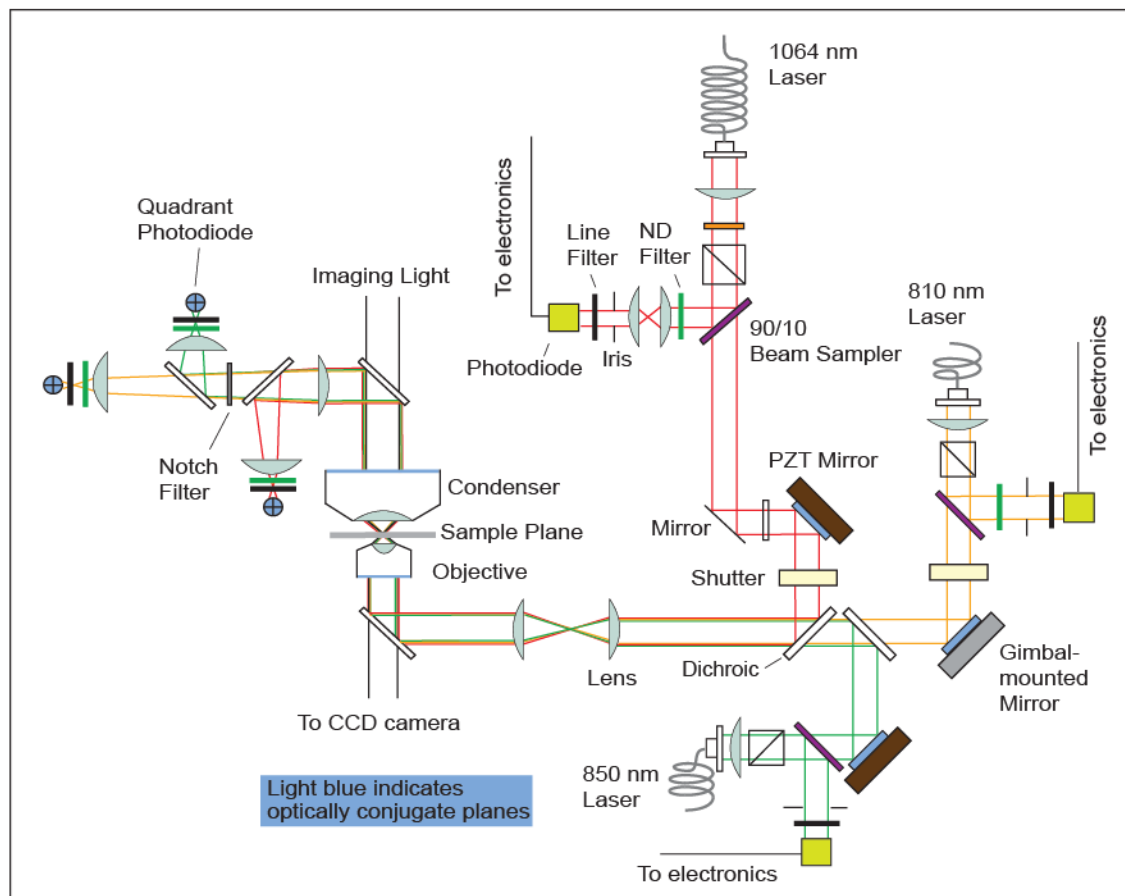


Figure 2.2: Diagram of the post-fiber optical setup.

This diagram shows the beam paths of the 1064 nm (red), 810 nm (orange), and 850 nm (green) beams. This figure was taken and modified from Figure 2.2 of Amanda E. Carpenter's thesis from the Perkins lab. Acronyms: CCD (charge-coupled device), ND filter (neutral density filter), PZT (lead-zirconate titanate piezo-electric transducer).

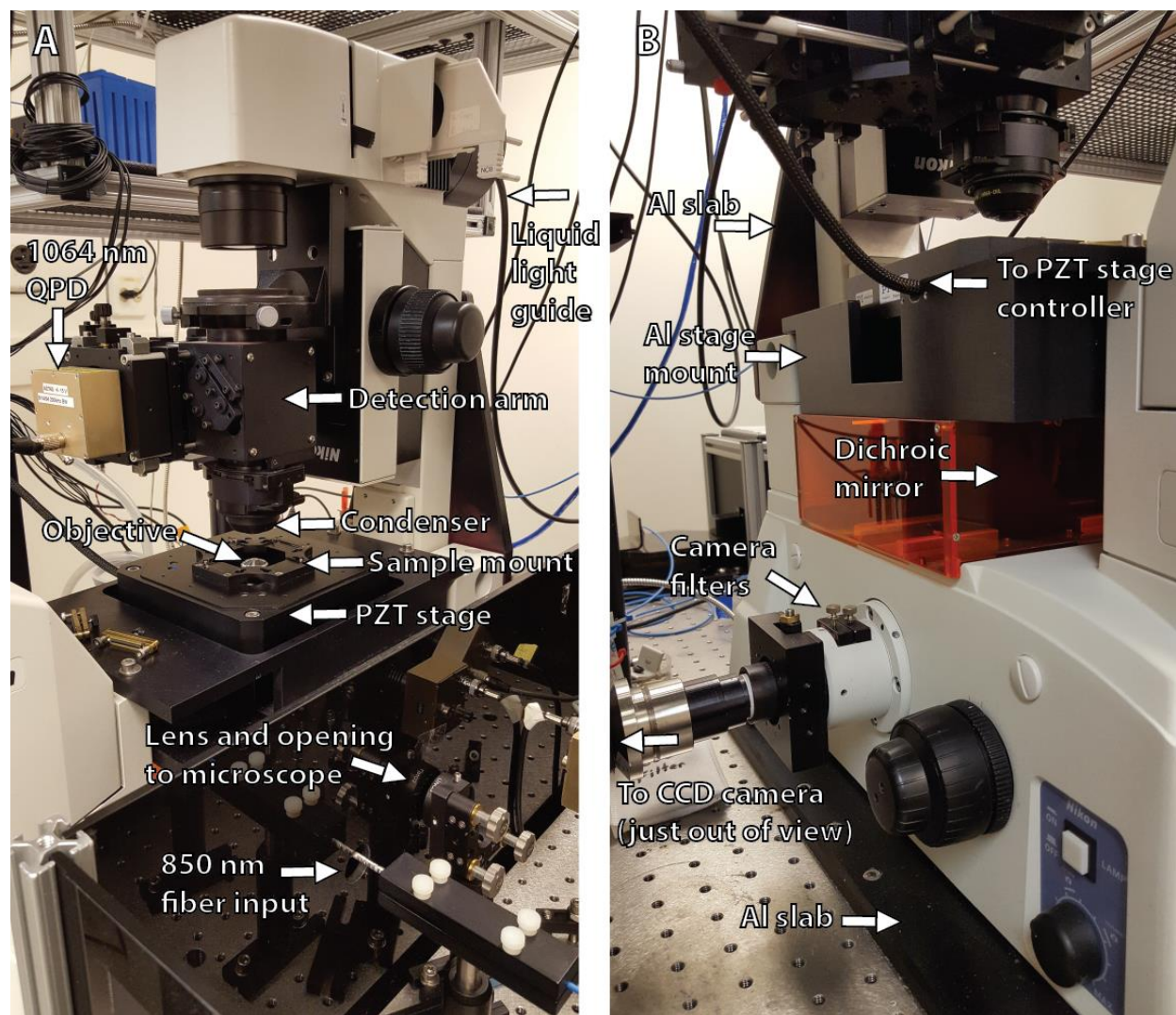


Figure 2.3: Labeled pictures of the microscope column and base.

A) Right side of the microscope and part of the plexiglass box that contains the post-fiber, free-standing optics. B) Left side of the microscope and part of the closed path leading to the CCD camera. Acronyms: Al (Aluminum), CCD (charge-coupled device), PZT (lead zirconate titanate piezo-electric transducer), QPD (quadrant photodiode).

P-517.3CD) with a microscope slide mount attached to its top, and is controlled by a digital piezo stage controller (PI E-710.P3D). At the top of the microscope column, a liquid light guide connects to a mercury arc lamp located several feet away. With appropriate filters in place, this lamp shines 532 nm light down the column, through a dichroic mirror in the detection arm that reflects infrared light and passes visible light, and into the sample plane. The lamp is kept far from the microscope to prevent its heat from inducing mechanical noise. Beneath the objective lens, another dichroic mirror reflects the three infrared laser beams into the objective lens and to the sample plane. It also passes the visible 532 nm light from the sample plane to a CCD camera (DAGE-MTI CCD100S) that is attached to the side of the microscope. This camera records the sample plane image and sends it to a monitor screen to be displayed.

As stated above, the laser beams couple into the microscope column using a dichroic, which reflects them towards a high NA objective lens. The two-lens telescope they pass through to enter the microscope shapes the 1064 nm beam width so that it just overfills the back aperture of the objective (~8 mm diameter). This ensures the 1064 nm beam is focused tightly in the sample plane, and thus achieves its highest trapping strength. In addition, the objective lens and the two PZT mirrors (for the 1064 nm and 850 nm beams) are spaced such that the plane defined by the objective back aperture is optically conjugate to the planes defined by the mirror surfaces. This means that pure rotations in one plane (e.g., the PZT mirror plane) produce pure translations in the other (e.g., the aperture plane). This propagates to the sample plane, so that pure rotations of the PZT mirrors result in pure translations of the 1064 nm and 850 nm beams in the sample plane; this is critical for accurate beam placement and later calibrations.

The beams are focused by the objective lens, propagate to the sample plane where they achieve their tightest focus (and where experimental samples are mounted and manipulated), and

continue on into the condenser lens. During experiments, the free space between the objective lens and the sample, as well as the sample and the condenser lens, is filled by immersion oil (Nikon type A oil, $n = 1.515$) to achieve better beam propagation. Also, the objective and condenser lenses are aligned for Kohler illumination, which provides the sample plane with the most isotropic illumination from the mercury arc lamp. While propagating through the sample chamber, the beams will partially scatter off of dielectric objects. The scattered portions of the beams propagate onward with the unscattered portions, and they interfere with each other (96). This interference is critical for object detection, as will be discussed below. The beams emerge collimated from the condenser and reflect off of the dichroic mirror into the detection arm of the microscope column (Figure 2.4A). This detection arm is an optical cage system that includes two dichroic mirrors and three quadrant photodiodes (QPDs). The two dichroics separate the three beams into three different beam paths (undoing the combination performed before entering the microscope). A QPD detector sits at the end of each of these beam paths. The operation of these detectors, and the electronic manipulations that are performed on their signals, will be covered in the next section, as this is the point where the optics part of the instrument ends and the electronics one begins.

2.1.2 Detection Electronics

The quadrant photodiode (QPD) at the end of each beam path has a planar photon detection area divided into four equal quadrants. The photon intensity incident on each quadrant is converted into a separate analog voltage signal and output through stress-relieved cables. The QPDs themselves are spaced along the beam paths (z position) so that back-focal plane detection is possible, and their perpendicular (xy) positions are set so that the non-scattered, incident beam

hits each quadrant with equal intensity. Three-dimensional position detection of microscopic dielectric objects is possible due to the interference between scattered and unscattered light when such an object partially blocks the beam's propagation path (96). If the object is positioned off-center from the beam axis in xy , the scattered and unscattered light will interfere such that the beam intensity distribution is shifted in xy . These shifts are detected by the QPD, as the intensity on each quadrant changes (while the total incident intensity remains the same). On the other hand, objects that move along the beam path (z position) shift the overall intensity (96, 97), but not the xy intensity distribution. The calibrations necessary to convert these intensity changes into real-space position changes are described later (Section 2.4.1).

Each QPD's four voltage signals are then sent to a separate custom-built JILA circuit board that performs a number of signal manipulations. This includes turning the quadrant signals into x , y , and z signals and passing them through a low-pass anti-aliasing filter. If we name the quadrants counterclockwise from the top right 1, 2, 3, and 4 (Figure 2.4B), then the z signal is just the sum signal ($V_1 + V_2 + V_3 + V_4$) while x and y are $(V_1 + V_4 - V_2 - V_3)$ and $(V_1 + V_2 - V_3 - V_4)$, respectively. The x and y signals are normalized by the sum signal (z signal) to ensure they stay independent of sum signal fluctuations. The low-pass filter frequency is set to half the data acquisition frequency to prevent aliasing when the signals are later converted from analog to digital. The board then outputs the xyz signals (Figure 2.4C).

The x and y signals go straight into a BNC breakout box that passes the signals into a connector block (NI SCB-68) and to our PXI data acquisition (DAQ) and control system. This system consists of a PXIe chassis/controller (NI PXIe-1082) that powers and buses data between a number of electronic DAQ boards. The x and y signals are sent into a multifunction input-output (IO) board (NI PXIe-6368) that samples and converts them from analog to digital using a

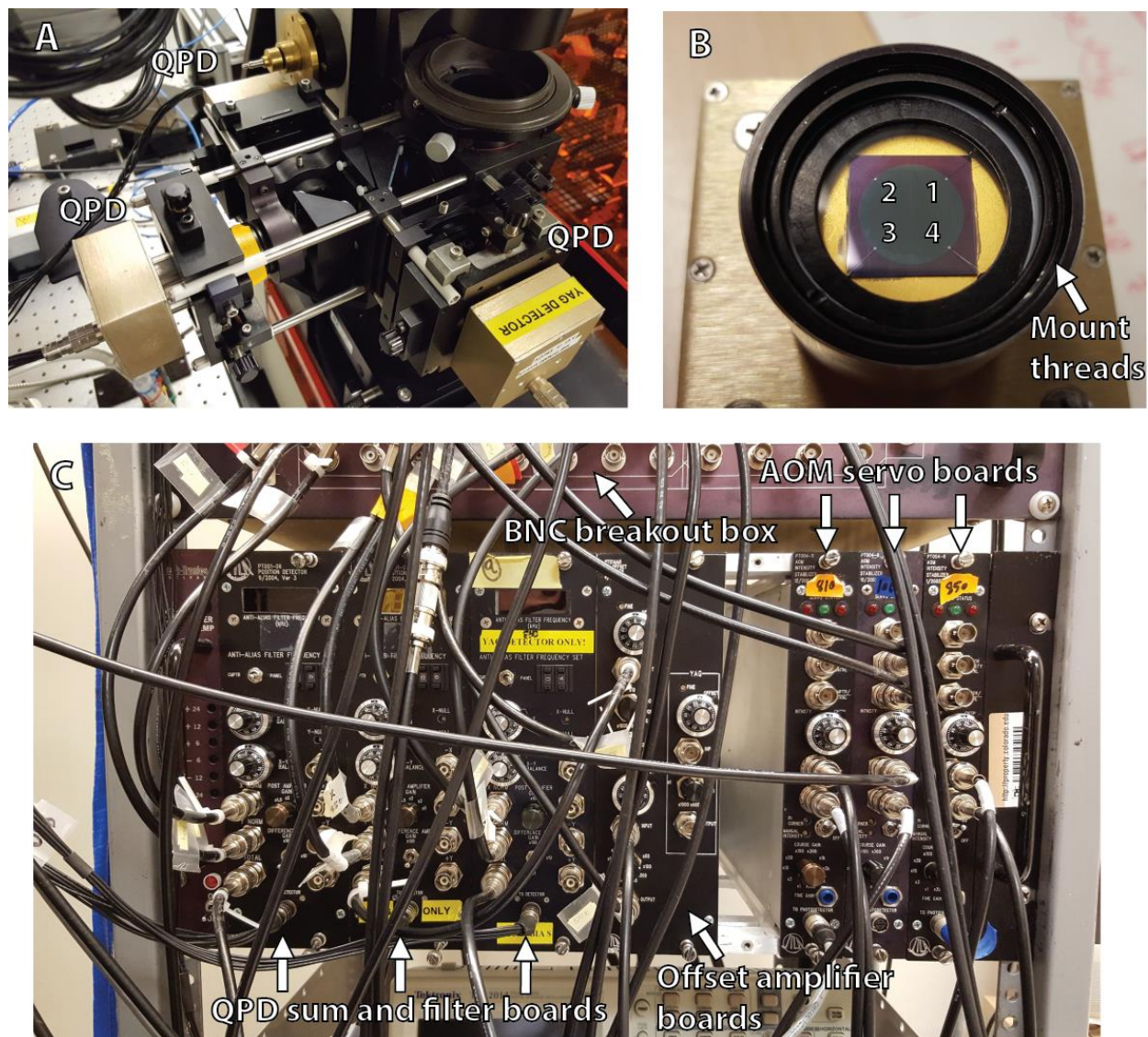


Figure 2.4: The electronic components of the optical trapping detection system.

A) Top view of the detection arm containing the three QPD detectors. B) Face-on view of a QPD, with the four detection quadrants labeled. C) Custom-made JILA electronic boards installed into a NIM rack. Above is one of the BNC breakout boxes used to condense signals into a single, multi-channel NI cable. Acronyms: AOM (acousto-optic modulator), BNC (Bayonet Neill–Concelman connector), NI (National Instruments), NIM (nuclear instrumentation module), QPD (quadrant photodiode).

16-bit analog-to-digital converter (ADC). It receives its sampling frequency from another board in the chassis, the PC communication board (NI PXIe-PCIe8375), that transmits commands from the instrument's computer to the chassis. This communication process will be discussed more in Section 2.1.3. The 16-bit ADC digitizes the full range of the signal channel, which is 20 V (-10 to 10 V) on this instrument, and assigns a 16-bit integer to each sampled voltage. This gives a sampling resolution of 0.3 mV. For good spatial resolution, we want to make sure that the voltage change which arises from objects moving $\sim 1 \text{ \AA}$ is much larger than 0.3 mV. Happily, for the xy signals it is 7x–8x larger.

However, this is not true for the z signal, as the sum signal voltage fluctuations due to z motion are extremely small. Thus, the signal must undergo an addition stage of processing before it can be sent to the multifunction IO board. From the summation and filtering board, the z signal is sent to another custom-built JILA electronics board which offsets and amplifies the signal. The offset is used to zero the signal so it can maximally amplified, and the amplification gain is usually set to 1000x. After amplification, the z signal is sent to the same breakout box as the xy signals, and follows the same path to the ADC board. Once sampled and converted, the now digital signals are bused to the PC communication board and sent into the PC.

2.1.3 Software communication

All electronic communication between the PC and the rest of the instrument is done through the coding platform LabVIEW (National Instruments). In LabVIEW, one can create a wide variety of programs (called VIs, or Virtual Instruments) for real-time control and data processing. As seen in the last section, all measured analog voltages are eventually sent to the PXIe chassis to be digitized and directed to the computer. LabVIEW is the platform that both requests collection of

these signals and serves as their final destination. Data transfer between LabVIEW and the PXIe chassis is mediated by another NI program, the Measurement & Automation Explorer (MAX). This program serves as a device manager, and is the link between the NI DAQ hardware (the chassis and its various boards) and the NI software (LabVIEW). Thus, data collection follows this general workflow: A LabVIEW VI is written to specify which voltage channels one wishes to read and at what sampling frequency. During an experiment, this VI runs on the computer and sends the task to MAX, which sends the task to the PXIe chassis, which sends the task to the multifunction IO board. The IO board samples the analog input voltages and digitizes them, then sends them back through the same pipeline until they are collected and recorded in LabVIEW. There they can be processed in real-time, used to make control decisions for other parts of the instrument, and saved to disk.

In addition to recording input signals, LabVIEW also serves as the output signal source for controlling various parts of the instrument. The same basic workflow applies: code is written that requests an output voltage signal be sent. When run, the code communicates the task through MAX to the chassis and multifunction IO board, which then converts the digital signal to an analog output voltage using a digital-to-analog converter (DAC). The signal is sent to a port on a BNC breakout box, which connects to part of the instrument. This is how the 1064 nm and 810 nm shutters are opened and closed, how the 1064 nm and 850 nm PZT mirror mounts are rotated (via the PZT mount controller), and how the intensity control on the 1064 nm AOM servo board is adjusted (to give real-time trap stiffness control).

LabVIEW is also used to control the PZT stage. However, this type of communication does not involve MAX as an intermediate. Instead, we use low-level VIs originally created by the stage's manufacturer to send commands from LabVIEW to the stage controller. This type of

communication uses the GPIB protocol (General Purpose Interface Bus) along a USB cable straight from the computer. GPIB is well-established and reliable, but uses ASCII strings to send information. These strings limit signal speed, which can be problematic in control applications such as active stabilization. The resolution to this issue is addressed in section 2.1.5. However, for all other purposes GPIB communication is fast enough, with the benefit of also being simple.

2.1.4 Laser stabilization

The laser beams we use for trapping and detection, while stable by manufacturer standards, are not inherently stable enough to differentiate between noise and the small signals arising from Å-scale biophysical motions. Therefore, we use stabilization servo loops to actively remove noise from each laser system. Laser beams can suffer from a variety of noise sources: intensity noise, polarization noise, mode noise (i.e., power in non-TEM₀₀ modes), and pointing (i.e., beam position) noise. The stabilization servo loop is based on a simple idea: convert as much noise as possible into intensity noise, and then use an acousto-optic modulator (AOM) to mitigate that intensity noise. Below I detail the operation of this feedback loop and its various components. Note that while each of the three lasers in this instrument has its own loop with its own settings, in operation they are almost exactly the same.

The first and last component of the servo loop is the AOM (Figure 2.5A,B). It consists of a crystal attached to a piezoelectric transducer. When an AC signal is applied to the transducer, it rapidly expands and contracts at the driving frequency. These vibrations hit the attached crystal, producing a travelling sound wave within it (which is made up of sections of more and less dense matter). Such sections possess higher and lower refractive index, respectively, and so act like a diffraction grating to any light passing through the crystal. The amount of light diffracted from

the incident beam (0th order) into higher order beams (1st order and larger) depends on the amplitude of the sound wave, which is set by the amplitude of the AC voltage signal driving the transducer. This signal is produced by a separate device, the AOM's modulation driver, and has a fixed frequency of 80 MHz (changing the driving frequency moves the diffracted beams in space, which is not something we want). This is how the AOM acts as a tunable diffraction grating that outputs a 1st-order beam of variable power (as previously stated in section 2.1.1). This 1st-order beam, which can have a power between 0 and 75% of the incident beam, is coupled into the rest of the system while the other beams are discarded. Thus the intensity of the final beam can be rapidly changed by changing the amplitude of the driving voltage. This is how the servo loop will compensate for intensity noise (Figure 2.5C gives the full diagram).

The next servo loop component is the polarization-maintaining fiber-optic patch cable that couples the 1st-order beam. We use an angle-cleaved input connector to reduce reflections, and a flat output connector to ensure the beam emerges in a Gaussian TEM_{00} mode. The diode beams are focused towards their cables using a single converging lens, while the 1064 nm setup uses two lenses (Figure 2.1). These lenses mitigate the pointing noise that arises during large servo changes. To understand how this noise arises, note that using a large drive voltage induces thermal heating in the AOM crystal, expanding it. This expansion changes the spacing of the diffraction grating (akin to changing the driving frequency). This moves the 1st-order beam, hence pointing noise. While the fiber cable propagates the beam to the main part of the optical setup, its most important job is converting pre-fiber pointing and mode noise into post-fiber intensity noise. This occurs because both noise sources reduce the input coupling efficiency, meaning less light gets into the fiber. Specifically, pointing noise moves the beam away from the optimal fiber coupling spot, and mode noise puts some beam intensity into non- TEM_{00} modes

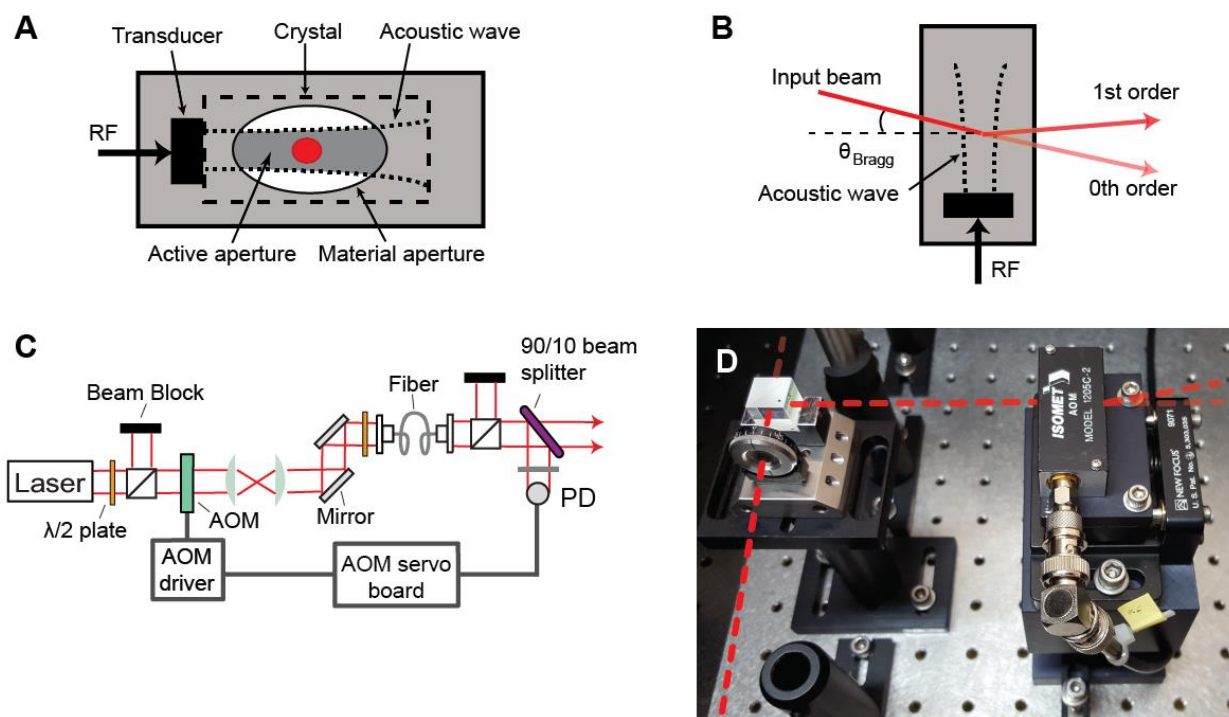


Figure 2.5: The operation of the AOM servo loop for reducing laser noise.

A) Side-view cartoon of the AOM. The RF drive signal drives the PZT transducer (black box) to vibrate, which propagates into the crystal (dashed lines) as a sound wave (dotted lines). The active aperture (dark grey region where the sound wave and material aperture overlap) can diffract any beams (red) that pass through it. B) Top-view cartoon of the AOM. Maximum diffraction occurs when the input beam enters the AOM at the Bragg angle. C) Diagram of AOM servo loop beam path and components. D) Top-view picture of the initial components of the servo loop. The half-wave plate and PBS cube (beam block out of shot) send a linearly polarized beam to the AOM, which is mounted onto a 4-axis tilt aligner for easy Bragg angle alignment. Reproduced from Okoniewski et al., 2017 with permission from Springer Nature. Acronyms: AOM (acousto-optic modulator), PBS (polarizing beam splitter), PZT (lead zirconate titanate piezo-electric transducer), RF (radio frequency).

which do not propagate well. At fiber output, the beam is recollimated and passes through a PBS cube. This cube turns any polarization noise into intensity noise, since only light intensity with the correct polarization passes through.

With mode, pointing, and polarization noise converted into intensity noise, part of the beam is siphoned off by a 90/10 beam splitter and sent to a PIN analog photodiode detector (YAG-444AH). These photodiodes are set up to have 60 MHz bandwidths and 5 ns rise times for 1064 nm incident light when a large -180 V reverse bias is applied (reverse biasing silicon photodiodes helps eliminate wavelength-dependent filtering effects, which are especially prevalent at 1064 nm). We reduce this reverse bias to -30 V, which gives the photodiodes more thermal stability at the cost of decreased detection bandwidth and response times. However, we find this bias to be a good compromise since the servo loop bandwidth is already limited by the AOM, as discussed below. The photodiode converts the incident beam intensity into a current, which is transformed into a voltage by an attached trans-impedance amplifier.

The photodiode signal is sent to a proportional-integral servo circuit board (Figure 2.4C). This board works to keep the photodiode voltage (the real laser intensity) equal to a pre-determined reference voltage (the requested laser intensity). It does this by modulating its only output, the voltage it sends to the AOM modulation driver, whenever the photodiode voltage changes. Changing the input voltage to the AOM modulation driver changes the driving signal amplitude it sends to the AOM transducer, which thereby changes the intensity of the diffracted 1st-order beam. This is the mechanism by which laser stabilization is achieved: all beam noise is converted into intensity noise and compensated for by changes to the AOM diffraction efficiency. The reference voltage used by the servo board determines the final beam intensity in the sample plane; for the diode lasers, that voltage is internally set in the board, since detection

beam intensity does not need to be changed during an experiment. For the trapping laser, that voltage is determined in LabVIEW by the user and sent out through the pathway described in section 2.1.3. This design enables rapid changes to the trap stiffness during experiments.

The bandwidth of this servo loop is ultimately limited by the time it takes to propagate changes in driving signal amplitude across the AOM crystal via sound waves. This limit will depend on the beam diameter size inside of the crystal (Figure 2.5), since more time is needed to propagate the sound waves across larger beams. We use beam diameters ~ 2 mm in size, which gives us a servo bandwidth of ~ 200 kHz.

2.1.5 Stage stabilization

In a surface-coupled optical trapping instrument, the system under study (usually DNA with modifications or associated proteins) gets attached to the sample chamber surface at one end and an optically trapped bead at the other. Position drift of the surface relative to the trapping and detection beams stretches or relaxes the DNA tether. These length changes convolve into and mask real biophysical signals, reducing the overall signal-to-noise ratio (S/N). Therefore, in addition to stabilizing laser beam noise, we often add an additional level of stabilization for high-resolution assays: active stabilization of the sample surface with a 3D PZT stage.

The idea behind stage stabilization is simple: we add rigid, dielectric fiducial marks to the surface of our sample chambers so that their position can be read by the 850 nm detection beam. If the fiducial mark (and therefore the surface) drifts away from a set position within the beam, a servo loop calculation is made to move the surface back into position using the PZT stage. The construction of these post-like fiducial marks is detailed in section 2.2.3. This section focuses on the operation of the servo loop itself.

To stabilize the surface during an experiment, the following general steps are performed (Figure 2.6A). Right before data is about to be taken, the 850 nm detection beam is roughly centered over a fiducial mark using its PZT mirror. A LabVIEW VI is then used to precisely center the beam over the mark and calibrate its voltage response into real-space positions. Once the beam is centered and calibrated onto a mark, another VI records the mark's position inside the beam at one instant of time. The VI then continually takes the difference between that position and the mark's current position. If that difference is nonzero, a correction signal is sent to the PZT stage. The simple version of the servo loop uses proportional correction, where the position difference is multiplied by a constant gain factor to produce the correction signal. More advanced servo calculations, like integral or differential corrections, are not used. This original version also uses GPIB communication, the ASCII-based protocol described in section 2.1.3 that issues all normal PZT stage commands. This servo loop calculates and sends the proportional correction within a LabVIEW VI, and runs at a typical bandwidth of 100 Hz. With this servo loop, the stage position can be stabilized with sub-nm precision in all three axes (Figure 2.6B).

While this proportional, software- and GPIB-based servo loop is sufficient for many applications, we also developed a more advanced version, modified from previous work (98). The major improvement is that servo calculation and stage command operations are moved from computer-based software to circuit board hardware. Specifically, the servo loop calculations are run on an FPGA (Field Programmable Gate Array) circuit board (NI PXI 7854R) installed within our NI chassis. An FPGA is a circuit board whose electronic components can be programmed into a variety of circuit diagrams. This programmability makes the FPGA a versatile tool for performing extremely fast calculations. A computer is needed to initially program the board, but otherwise the FPGA runs independently using its own internal clock, enabling much faster and

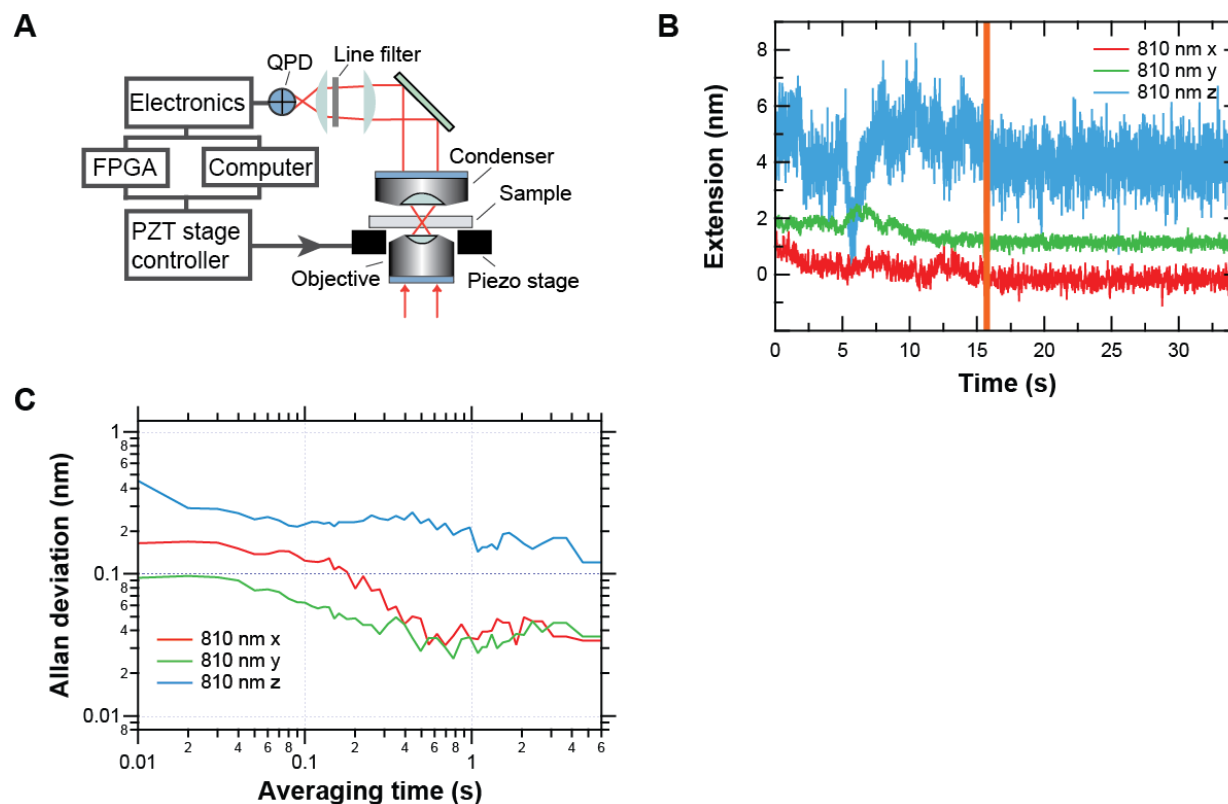


Figure 2.6: Operation and results of the stage stabilization servo loop.

A) Diagram of the beam path and components of the stage servo loop, including the choice of using either a software-based (computer) or hardware-based (FPGA) servo calculation method. Reproduced from Okoniewski et al., 2017 with permission from Springer Nature. B) 100 Hz beam 1 post data. All gains 0.1. Note that z axis separately amplified. C) Allan deviations of stabilized parts of traces in (B). Acronyms: FPGA (field programmable gate array).

more deterministic operations than computer-based software. The FPGA also enables PIO (parallel input-output) communication with the stage controller, as opposed to GPIB. The PIO protocol uses simple binary signals for commands instead of GPIB's large ASCII characters, enabling faster communication. Another improvement is that an integral correction term is now calculated in addition to the proportional one; while proportional calculations are reactionary (i.e., they respond to immediate drift), integral calculations try to preemptively prevent drift by observing drift trends (from past proportional responses) and correcting for them in advance. All of these improvements combine to make a servo loop that runs deterministically at 500 Hz (near the resonance frequency of the stage, the current bandwidth limit) without software-based interruptions or timing limitations.

2.2 Sample chamber manufacture

In this section, I discuss the sample chambers I use in all of my experiments. I first cover their general design and construction (section 2.2.1), then go through the various ways we modify the coverslip surface. First, I cover the protocol for cleaning and etching coverslips (section 2.2.2). Next, I detail the process of fabricating fiducial marks onto the surface for high-resolution assays (section 2.2.3). Finally, I go through the protocol for azide functionalizing coverslips so that they can be used in click-chemistry reactions (section 2.2.4).

2.2.1 Single-channel flow chambers

The single-channel flow chambers used in my experiments have a simple design and can be assembled at a lab bench by hand in a few minutes. An example chamber is pictured in the middle of Figure 2.7. The single channel has dimensions of 25 x 5 x 0.15 mm³, which

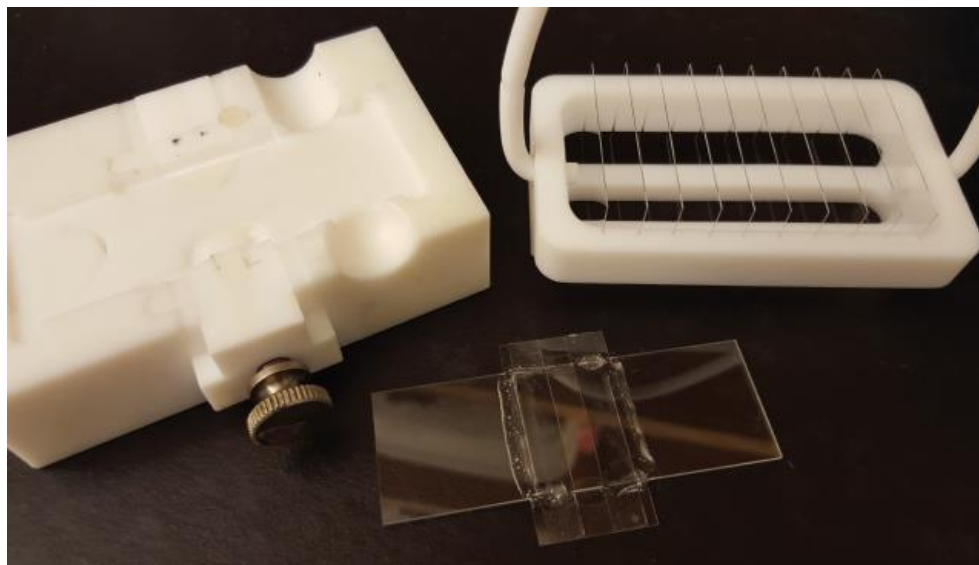


Figure 2.7: Single-channel flow chamber and accessories.

Left: A custom-machined Teflon microscope slide mount. The two black dots near the top indicate where the tape edges should be placed. Center: An example single-channel flow chamber, constructed out of a microscope slide, a coverslip, double-sided sticky tape, and epoxy. Right: A Teflon coverslip holder with detachable handle. Reproduced from Okoniewski et al., 2017 with permission from Springer Nature.

corresponds to a volume of $\sim 15 \mu\text{L}$. The channel is used to flow various buffers and reagents into and out of the chamber. The method used to create surface-bound DNA tethers in these flow chambers is given in section 2.3.2. I typically build anywhere from two to six chambers on an experiment day, depending on the amount of data I want to collect.

To build a chamber, we first insert a microscope slide (Corning $75 \times 25 \times 5 \text{ mm}^3$) into a custom-machined Teflon mount (pictured on the left side of Figure 2.7). We next cut a $\sim 7 \text{ cm}$ long piece of double-sided sticky tape (Scotch, $\frac{1}{2}$ inch wide) in half lengthwise. Using tick marks drawn onto the Teflon mount as a guide, we stick the two tape halves to the slide 5 mm apart, perpendicular to the slide's long axis. To ensure smooth sticking, we press the tape down into the slide with a pair of rubber-tipped tweezers. We then take a cleaned/modified coverslip (Corning $22 \times 40 \text{ mm}^2$, thickness $1 \frac{1}{2}$) and lay it along the two tape halves, again orthogonal to the slide's long axis. To ensure smooth sticking and remove air pockets, we remove the slide from the mount and use the tweezers to press the coverslip into all parts of the tape. We then use a razorblade to cut off any excess tape overhanging the coverslip. These steps are repeated as needed to make the number of desired sample chambers. We then mix together 5-minute epoxy (Devcon) to rigidify the chambers, applying it to all gaps between the slide and coverslip (except for the two channel openings). The liquid epoxy wicks into the gaps between the surfaces and hardens, providing a rigid, liquid-tight, single-channel sample chamber.

The single channel is composed of a coverslip surface bottom, microscope slide top, and sticky tape sides. Unlike the coverslip, the microscope slide is not cleaned before use, nor is any treatment performed on the sticky tape. And while no contamination has ever been observed from these components, it is common practice to rinse the channels of newly-constructed chambers by flowing through $200 \mu\text{L}$ buffer (typically 20 mM NaCl, 20 mM HEPES pH 7.5). In

addition, note that the channel dimensions are extremely large compared to the tethered beads commonly trapped in the instrument. This means that the coverslip surface is the only surface to have a hydrodynamic effect on the solution surrounding the beads (see section 2.4.1).

2.2.2 KOH-etched coverslips

Before coverslips can be modified by fiducial mark fabrication or azide functionalization, they must first be cleaned and etched. Cleaning removes contamination and etching smooths the surface to enable more consistent, isotropic functionalization reactions and improved non-specific protein binding (e.g., antidigoxigenin; see section 2.2.4). Note that etching must be performed before fiducial mark fabrication, since the etch can partially dissolve the marks.

We use a concentrated solution of 3 M KOH (potassium hydroxide) dissolved in 70% ethanol and 30% water for microscopic cleaning and etching. A beaker of this solution is placed in a sonicator, as well as a beaker of acetone and two beakers of 18 M Ω purified water. The sonicator is used to enhance the diffusion and impact of the solutions' molecules. The protocol has the coverslips (placed in the Teflon holder shown to the right in Figure 2.7) submerged sequentially in the beakers of acetone, KOH, water, water for 3 min intervals. After each interval, the coverslips and holder are washed down with either an ethanol or water squirt bottle. After the four beakers, the coverslips are squirted down once more with water then ethanol, dried in a microwave, and stored in parafilm-wrapped containers.

2.2.3 Fiducial mark fabrication

For the best stabilization performance, we want symmetric fiducial marks that are rigid and strongly attached to the coverslip. This way, detected drift is due to surface drift and not relative

motion between the mark and surface. To this end, we manufacture fiducial marks out of hydrogen silsesquioxane (HSQ; Dow Corning FOx-16), a negative resist solution that crosslinks when exposed to concentrated electron or extreme ultraviolet (EUV) beams. By coating a coverslip with HSQ and selectively irradiating cylindrical sections of the coating with a controlled electron beam, we can induce only those sections to crosslink. Once that is done, the coverslip can be submerged in a TMAH (tetramethylammonium hydroxide) solution to etch away the noncovalent HSQ while preserving the covalent sections. These cylindrical sections are the fiducial marks, and due to their shape we commonly refer to them as “posts”.

The fabrication process outlined above can be divided into three parts: coat the coverslip with HSQ, crosslink HSQ sections with an electron beam, and remove the unwritten HSQ (Figure 2.8). We coat coverslips using a spin coater, a small mount which can spin rapidly and hold anything placed onto it using vacuum suction. We place a coverslip onto it, start the spin process (2000 rpm for 45 s), and immediately pipette 200 μL HSQ into the middle of the coverslip. The spinning isotropically spreads the liquid HSQ over the entire surface, which ensures that the fiducial marks all have the same final height (typically ~ 600 nm for 200 μL HSQ). We then place each coverslip onto a 180 $^{\circ}\text{C}$ hotplate (dry side down) to harden the HSQ by partially dissolving its volatile carrier solvent. This makes later manipulation and transport easier and ensures the coating keeps its even thickness.

To crosslink HSQ sections, we beam-write with a scanning electron microscope (SEM). This instrument uses an electron beam gun to image and write, and is equipped with a low-vacuum sample chamber that uses water vapor to de-charge dielectric samples. Charging occurs when a sample cannot conduct away the bombarding electrons from the SEM, i.e. non-metallic samples. Excess sample charge can deflect the incoming electron beam and generate many

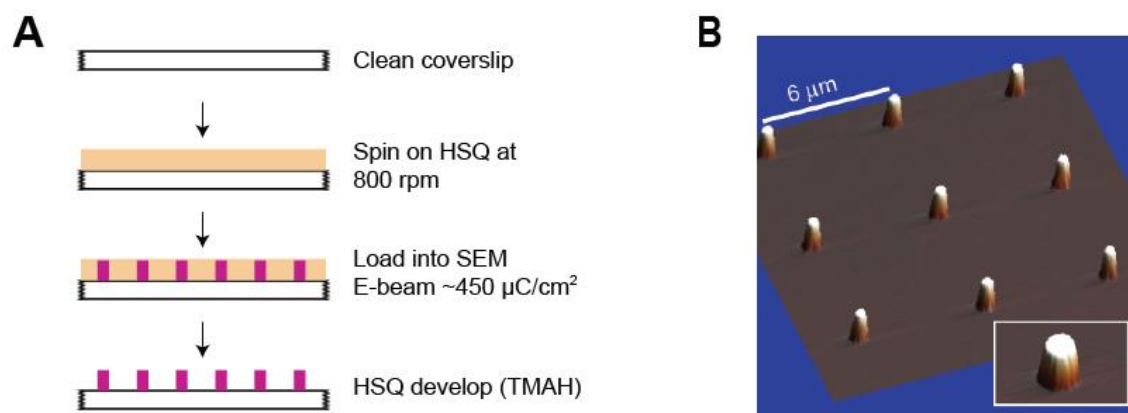


Figure 2.8: HSQ-based fiducial mark fabrication.

A) The general steps for fabricating glass-like fiducial marks onto a glass coverslip: clean the surfaces, spin on the HSQ, irradiate the HSQ with an electron beam to create the posts, and develop away the excess HSQ. B) An example image of a fabricated coverslip with posts, taken by AFM. Reproduced from Okoniewski et al, 2017 with permission from Springer Nature. Acronyms: AFM (atomic force microscopy), HSQ (hydrogen silsesquioxane), SEM (scanning electron microscope), TMAH (tetramethylammonium hydroxide).

undesirable effects, and is a serious concern in SEM work. Previous versions of this protocol did not have access to a low-vacuum SEM to automatically de-charge the HSQ, and so used an aluminum coating on top of the HSQ to de-charge the sample. Happily, that is no longer necessary, and we simply insert an HSQ coverslip into the SEM mount after some preliminary alignment steps. After further time aligning SEM components, we run a program (written in the development platforms DesignCAD and NPGS) that beam writes a $1.5 \times 1.5 \text{ mm}^2$ square array of cylindrical posts into the HSQ, $\sim 600 \text{ nm}$ in diameter spaced $15 \text{ }\mu\text{m}$ apart. Once done, the coverslip is removed from the SEM chamber and the process is repeated as necessary.

The development process is very simple. All beam-written coverslips are loaded into a Teflon coverslip holder (the same kind used in the KOH treatment) and submerged in a TMAH development solution (Dow electronic chemicals MF CD-26, 2.4% TMAH) for 15 min. This is long enough to remove all of the non-crosslinked HSQ from the coverslips, leaving an array of cylindrical posts. The coverslips are then washed with water and dried with nitrogen gas.

2.2.4 Azide functionalization

Surface-coupled experiments require one end of a DNA molecule to be attached to the sample chamber coverslip surface. In early experiments, this was accomplished through a noncovalent digoxigenin / antidigoxigenin interaction. Specifically, a solution of $100 \text{ }\mu\text{g/mL}$ antidigoxigenin antibodies in PBS 1X was flowed into the single channel and incubated for 1 h. During this time, the antibodies nonspecifically bind to the coverslip surface, coating it with potential digoxigenin binding sites. After a buffer wash, $75 \text{ }\mu\text{g/mL}$ of bovine serum albumin (BSA) was then incubated in the chamber for 1 h to nonspecifically bind to and passivate the remaining patches of glass surface. After another wash, 300 pM DNA with a digoxigenin tag on one 5' end was incubated

for 2 h; the dig binds to the antidig, coupling the DNA to the surface. While this method is a standard way to attach DNA to surfaces, it has many clear problems: it relies on nonspecific sticking, noncovalent bonds, and multiple incubations.

Azide functionalization addresses all of these problems (99). In this method, silane-PEG-azide molecules (Nanocs Inc. PG2-AZSL-600 or PG2-AZSL-3400, where the end number specifies the molecular weight) are covalently bound to the surface, making it both nonstick (via the PEG) and available for covalent bioconjugation. When DNA molecules with DBCO (dibenzocyclooctyl) labels attached to one of their 5' ends are incubated with these surfaces, the DBCO and azide groups undergo a copper-free click chemistry reaction to produce a covalent linkage. The DNA is therefore attached to the surface via two covalent linkages and a PEG molecule of selectable size. The azide functionalization process is detailed below (Figure 2.9). Once functionalized, these coverslips are stored dry at 4 °C in a parafilm-sealed container. They retain their full efficiency for up to two weeks, and a workable efficiency for up to a month.

To begin the functionalization process, cleaned coverslips are UV irradiated to improve the reaction efficiency between the silane (SiH_4) and the coverslip surface (SiO_2) groups. This is done by incubating the coverslips in a UV ozone chamber (Novascan Technologies, PSD-UV8) for 30 min. Next, the coverslips are submerged in a ~0.15 mg/mL solution of silane-PEG-azide dissolved in toluene. For this step, we machined a custom Teflon mount that held the coverslips and displaced a large volume of fluid (Figure 2.9). With this mount, up to 12 coverslips can be functionalized at a time using only 100 mL of the silane-PEG-azide solution. The coverslips are left submerged in this solution in a covered beaker for 30 min at 60 °C (fluid temperature) on a hot plate. This incubation time and temperature were empirically determined to give the best functionalization results. Once the incubation is done, the coverslips are sequentially washed

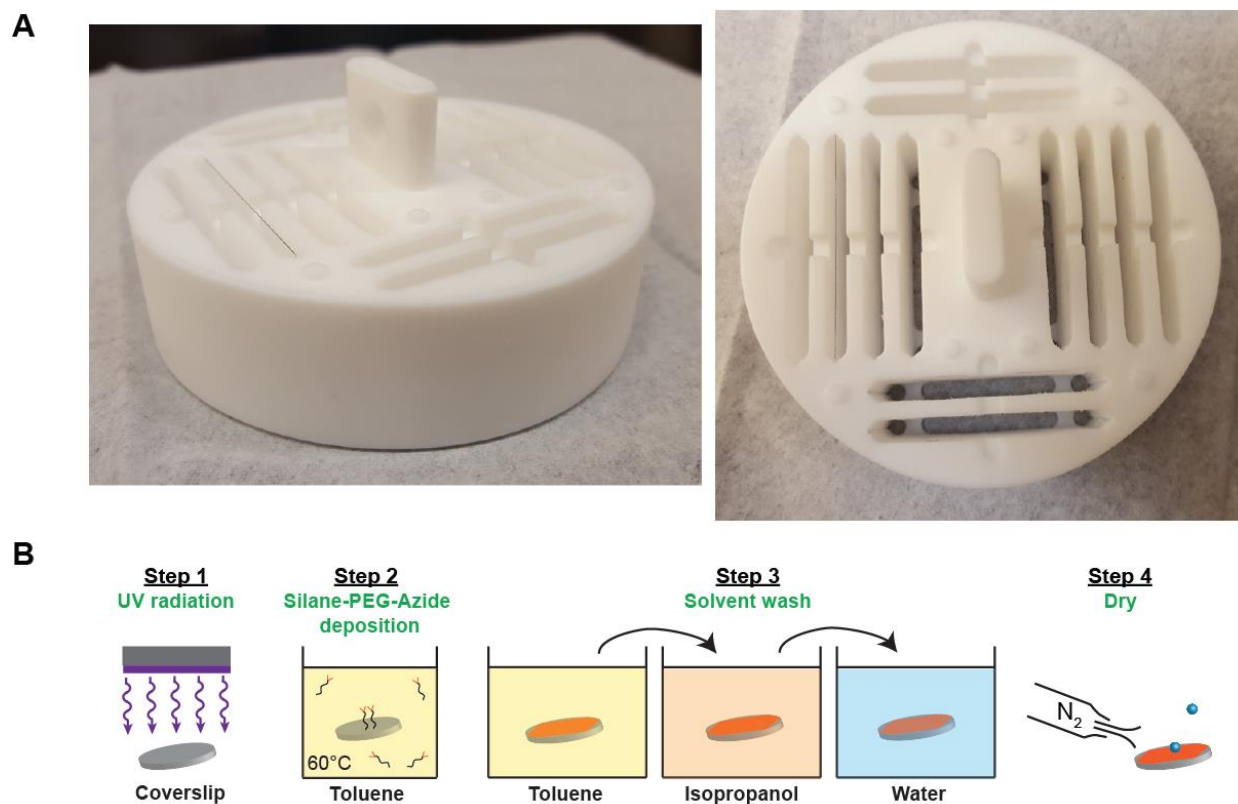


Figure 2.9: Azide functionalization process and accessories.

A) A custom-machined Teflon coverslip holder for the azide functionalization process. The holder was designed to displace a large amount of fluid, so the amount of silane-PEG-azide per coverslip used is minimized and overall costs reduced. A coverslip is placed in the second-left slot as an example. B) The steps of the functionalization process. A circular AFM coverslip is depicted as an example; in practice, the above Teflon holder is used with rectangular coverslips. Adapted from Walder et al., 2017 with permission from the American Chemical Society. Acronyms: PEG (polyethylene glycol), UV (ultraviolet).

with toluene, isopropanol, and 18 M Ω purified water. The initial transfer between the silane-PEG-azide solution and the toluene is performed rapidly to prevent drying (which can create ruinous PEG agglomeration). The coverslips are then removed from the block holder, transferred to a regular holder, and dried with nitrogen gas.

2.3 Biological assays

In this section, I discuss the biological preparations that go into surface-coupled optical trapping experiments. I first detail some of the general steps that go into preparing the micron-scale DNA used in my experiments (section 2.3.1). I next cover how to prepare the fundamental assay for my trap, the tethered bead assay (section 2.3.2). I then go through the storage and preparation procedures for the *E. coli* RecQ helicase proteins studied in this work (section 2.3.3).

2.3.1 General DNA preparation

In my experiments, I tend to work with DNA molecules 3000–6000 bp long, as they are geometrically easy to use in my instrument. And while much of my work utilizes specially engineered DNA regions, these regions never exceed ~1000 base pairs (bp) in length. The remaining length of each molecule, the relatively inactive “handle” regions, are derived from an M13mp18 plasmid (New England Biolabs). A complete DNA molecule is typically composed of two handle regions and one engineered region; often, the engineered region is contained within the handle primers. These regions are combined using matching endonuclease sites and ligation, after each individual region has been amplified by polymerase chain reaction (PCR). The basic workflow for building a complete DNA molecule is this: PCR amplify all component regions, cut them with their endonucleases, and then sequentially ligate pairs of the products together.

Then the full product is inserted into a plasmid, and biotin- and DBCO- labelled primers are used to amplify the construct. The following paragraphs give a detailed workflow.

The first step to building a complete molecule is to PCR amplify its component regions. We perform the PCR using a Bio-rad T100 Thermal Cycler, and typically use either KOD hot start polymerase (Novagen 71086-4) or Taq polymerase (Life Technologies 10342-053). DNA primers are bought from Integrated DNA Technologies. While the primer sequences and PCR conditions vary from construct to construct, all PCR products are purified using a Qiaquick purification kit (Qiagen 28106), then loaded onto a 1% agarose/TAE (Tris-HCl, Acetic acid, EDTA) gel where the product band is excised. The product is then processed by a Bio-Rad Freeze 'N Squeeze (Bio-Rad 732-6165), concentrated with a Millipore Amicon Ultra 0.5 mL 10K filter column (Millipore UFC501096) with TE (Tris-HCl, EDTA) buffer exchanges, then subjected to another Qiaquick kit to remove residual agarose.

The purified PCR products are then cut with their respective endonucleases, exposing complementary ssDNA “sticky ends” that can anneal to one another. Two of the products are combined together in equimolar ratio so that they anneal, then are ligated with T4 DNA ligase (New England Biolabs). Ligations are incubated at 16 °C for 16 h in 50–100 μ L volumes, with 5% ligase (the maximum amount possible) and 1–2 pM of each DNA. The ligated product is then run on a 1% agarose/TAE gel and the band is excised and purified as above. If a third PCR product exists, the process is carried out again between that component and the previous ligation product. Fully ligated constructs are then incubated with Taq polymerase at 72 °C for 10 min to generate A overhangs for TA cloning.

To make PCR amplification of this final construct easier, it is cloned into a bacterial plasmid using TOPO[®] XL PCR cloning kit (Life Science K4700-10). The plasmid is transformed

into competent *E. coli*, grown up in Luria Broth, and then isolated (Qiaprep Spin Miniprep Kit, Qiagen 27106). After verification by sequencing and PCR, these plasmids are used as templates for the biotin- and DBCO-labeled primers. The steps for that PCR are the same as above.

2.3.2 Tethered bead assay

To perform experiments in a surface-coupled optical trap, DNA must be attached to the sample chamber surface at one end and a dielectric bead at the other. This section describes the protocol used to generate those attachments, specifically a covalent azide-DBCO bond from the DNA to the surface and a noncovalent streptavidin-biotin bond from the DNA to a bead. The assay requires sample chambers (section 2.2.1) made with azide-functionalized coverslips (section 2.2.4), as well as streptavidin-coated beads. I prepare such beads using a well-established protocol (100) which covalently coats polystyrene beads ($r = 250$ or 375 nm, Invitrogen / Molecular Probes, C37241) with streptavidin (SA) molecules (Vector Laboratories, SA-5000).

To begin, the DNA stock must be diluted in a DNA deposition buffer and incubated in the sample chamber. However, we have found that the exact DNA and salt concentrations needed to produce good samples varies depending on the batch of silane-PEG-azide in use. We assume this batch variation is due to varying levels of trace chemical contaminants produced during silane-PEG-azide synthesis affecting the electrostatics near the sample surface. Roughly, we have found that DNA concentration values of 0.1 nM to 1 nM work, with monovalent salts of 20 mM to 100 mM. Our current protocol uses these conditions: 1 nM DNA in a buffer of 20 mM NaCl, 20 mM HEPES pH 7.5, and 1 mM EDTA pH 8. At times, I have found it helpful to add 2 mM MgCl₂ and 2 mM EDTA pH 8, as well, but this varies batch-to-batch. We prepare 15 μ L of this dilute DNA solution per chamber. Once made, this solution is set aside and 200 μ L of

dilution buffer (without DNA) is flowed through each chamber using aspirator suction to clean the flow channel. The DNA solution is then flowed in and the samples are left to incubate in humidity chambers for 1 h at room temperature.

During this incubation, a 2.5 pM solution of SA-coated beads is prepared from 250 pM stock. To remove any free streptavidin present in this bead solution (which diffuses much faster than the beads and could bind to the DNA first), a buffer exchange is performed. 1 μL of SA-bead stock is mixed with 100 μL of a buffer we call MTWB-150 [20 mM Tris-HCl (pH 7.5), 150 mM NaCl, 0.4% Tween-20], spun down in a centrifuge at 14 krpm for 5 min, and its supernatant removed. The beads are then reconstituted in 100 μL MTWB-150 and inserted into a sonicator for ~40 min to ensure monodispersity (clumped beads attached to a tether cannot be used). The assay is timed so that bead sonication ends at the same time as the DNA incubation. The sample channels are then washed with 200 μL PBS 1X and 200 μL MTWB-150 to remove the non-bound DNA, and 15 μL of the SA-bead solution is flowed into each sample. The sample are then incubated for 20 min at room temperature so that the SA-beads can diffuse and bind to the biotin labels on the surface-bound DNA molecules. After this incubation, the chambers are washed with 200 μL MTWB-150 and 200 μL working buffer (whatever that happens to be for the experiment at hand) to remove the excess beads.

2.3.3 RecQ helicase purification and preparation

Initially, we did not make the RecQ proteins ourselves, but instead received stock aliquots from Yeonee Seol and Keir Neuman at the National Institutes of Health. The method they used to create these proteins has been detailed (*101*). Specifically, we were gifted 8.5 μM protein aliquots containing 30 mM Tris-HCl (pH 7.5), 200 mM NaCl, 1 mM BME, and 10% glycerol,

and stored them at $-80\text{ }^{\circ}\text{C}$. The first batch we received worked very well; however, I found that subsequent RecQ batches had much lower unwinding activity, indicating that part of the batch contained inactive / misfolded proteins. After trial and error checks between ourselves and our collaborators, we still could not identify the exact reason for the lower activity. We then decided to make the RecQ proteins ourselves, with Yeonee and Keir kindly providing us the plasmids to make wild-type RecQ and the HRDC-deleted RecQ truncation. Specifically, our lab technician Lyle did the wet work in producing the proteins, while I researched and compared different RecQ production methods and tested the batches for activity.

Lyle followed the protocol in (101) exactly when making our first batch of RecQ^{ΔH}, and the final product turned out exactly like the recent aliquots we had received from the NIH: lower activity than expected. My standard method of testing RecQ activity is a single-molecule optical trapping assay where I check whether the frequency of unwinding at 200 pM RecQ (at saturating ATP) is comparable to our initial gold-standard aliquots and prior on-rate measurements (further detailed in section 3.3). However, to ensure these new RecQ batches were tested accurately, I also performed a bulk ATPase assay with the help of the Leinwand lab at CU Boulder. That assay confirmed the results of my single-molecule activity assay: the recent RecQ^{ΔH} batches from the NIH and our newly created one were performing poorly.

Lyle and I worked to debug the problem. Comparing the purification protocols of different groups showed a lot of small variations in buffers and storage conditions, but those did not improve our end product. I then noted that RecQ has a zinc-binding domain, which means that each RecQ protein needs one ion of zinc to fold properly. Perhaps the low observed activity was due to a resource shortage: there being many more recombinant RecQ proteins in the *E. coli* cells than there were available zinc ions. If that was the case, many of these expressed proteins

would not fold properly, and so lose their activity. To address this, Lyle first switched the cell growth media from Luria broth to Terrific broth, which has 5x more yeast extract in it (and thus zinc). This batch had more activity, though it is hard to tell whether the additional nutrients were truly the deciding factor. I then found a RecQ protocol that expressed the proteins at 18 °C for 16 h instead of at 37 °C for 4 h (102). Cool protein expression is generally done to ensure correct folding, and since misfolding was our hypothesized problem source, we immediately made a batch with Terrific broth and 22 °C (room temperature) expression. Cool protein expression should also result in fewer proteins being expressed per unit time, which would help alleviate zinc scarcity in folding if that turned out to be the problem. This batch's activity turned out very nicely, comparable to our original gold standard batch, and so we kept and adapted this protocol (provided in the Appendix). Figure 2.10 gives an example SDS-PAGE gel of both purified RecQ^{WT} and RecQ^{ΔH}.

To prepare an unwinding experiment, I first prepare a tethered bead slide (section 2.3.2). During the final bead incubation step, I remove a protein aliquot from storage, thaw it on ice, and dilute it down using a dilution buffer [30 mM Tris-HCl (pH 7.5), 100 mM NaCl, 10% glycerol]. Aliquots of ATP and DTT, stored at -20 °C, are thawed simultaneously. ATP is needed to fuel the RecQ protein's processive translocation and unwinding activity; DTT provides a reducing environment that can aid in protein stability (though I have found RecQ performs equivalently without DTT in solution). These components are used to make a working buffer containing 30 mM Tris-HCl (pH 7.5), 100 mM NaCl, 1 mM MgCl₂, 0.4% Tween-20, 1 mM DTT, and the desired final ATP and RecQ concentrations.

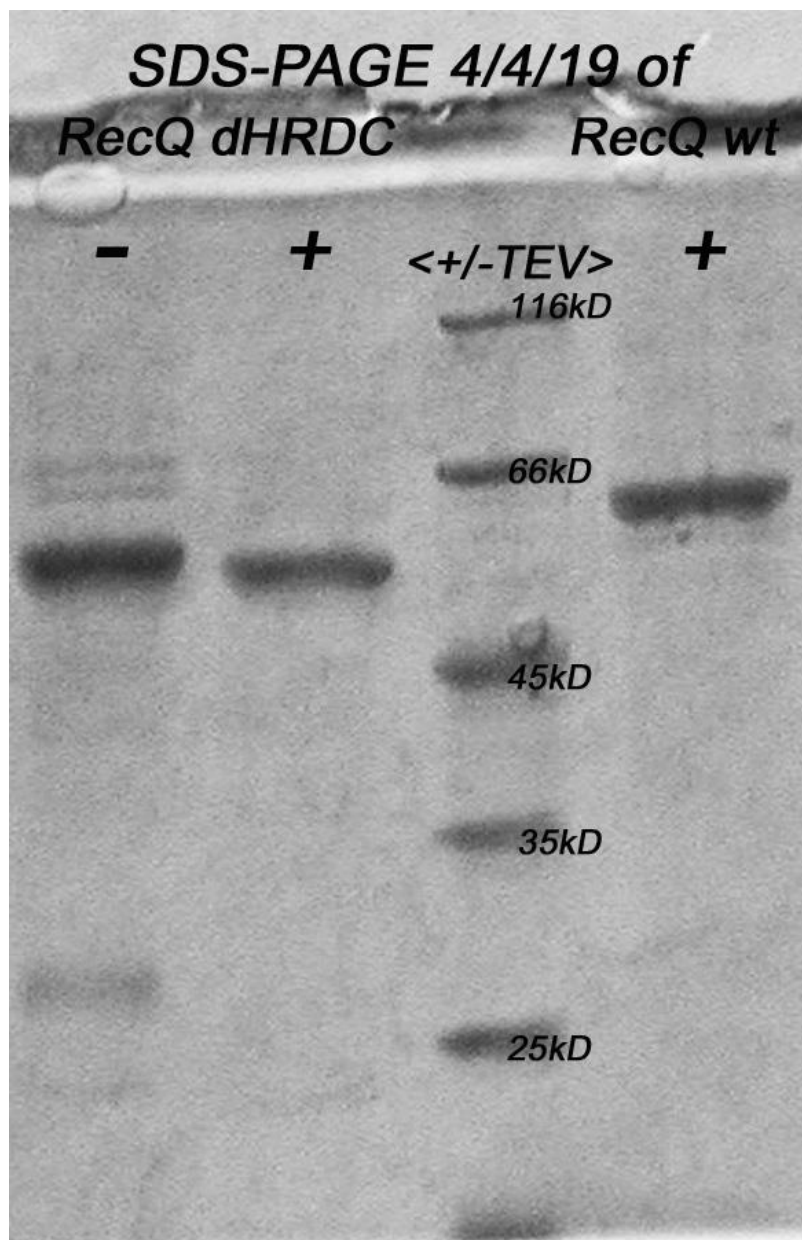


Figure 2.10: RecQ helicase purification gel.

An SDS-PAGE gel of RecQ^{ΔH} (lanes 1 and 2) and RecQ^{WT} (lane 4). Lane 3 is the size standard. Lane 1 is the initial 6xHis-TEV-RecQ^{ΔH} (obtained after step II.7 in our RecQ purification protocol in Appendix B). Lane 2 is the purified RecQ^{ΔH} after the tag has been cleaved off with TEV protease and a negative selection performed. Lane 4 is corresponding result for RecQ^{WT}. This gel assay was performed and recorded by Lyle Uyetake, the Perkins lab technician.

2.4 Data collection and analysis

In this section, I discuss the basic protocols we use to calibrate signals and perform experiments in the optical trap. First, I detail how we position a trapped bead (either free or attached to a DNA tether) in space and calibrate its detector beam voltage signal to its real space position (section 2.4.1). I then cover the methods we use to determine the optical trap's stiffness k_T and its linear region (section 2.4.2). Knowing both parameters is necessary to accurately measure the optical force exerted on a trapped bead. These first two sections thus explain how we measure a bead's position and force, our two fundamental measurements. Next, I go through how we center the surface-DNA attachment point directly under the trapped bead and simultaneously determine the rough worm-like chain (WLC) parameters for the DNA tether (section 2.4.3). I finish by discussing the two main types of experiments run on this instrument: overstretching assays (section 2.4.4) and force-clamp assays (section 2.4.5).

2.4.1 Bead position setting and calibration

To set the position of a trapped bead, one first has to actually trap a bead. This is fairly easy for beads attached to DNA tethers, as the surface can be imaged using the CCD camera. To do this, we use the fact that the trapping and detection beams reflect a small portion of their intensity off of the coverslip glass as they transmit through the chamber. This reflection hits the CCD camera and is strongest when the beam focus is on the surface. From this surface position, tethered beads can be seen and it is simply a matter of moving the stage so that a bead gets pulled into the trap. Free beads, on the other hand, can diffuse to any location in the sample chamber. To trap one of them, we move the stage (and thus sample chamber) down so that the trap focus goes deep into

the chamber (we find $\sim 6 \mu\text{m}$ above the surface is a productive location). We then wait for a bead to diffuse by and move the stage to trap it.

With a bead trapped, its average position will now match the position of the trap center. For the best detector response, we want this trap center to coincide with the center of the 810 nm detection beam. We thus need to center the lasers so that they are collinear. To do this, we use the 1064 nm beam's PZT mirror to move the beam in xy space (the 810 nm beam stays fixed). Recall that rotating the PZT mirror translates the beam in the sample plane. The mirror can be rotated either by hand (for large translations) or by the PZT mount controller, which we direct from the computer. Using a standard calibration procedure, sub-nm calibration precision can be achieved for controller-directed mirror motion (the procedure is detailed in A. E. Carpenter's thesis, section 2.4.8; it involves using a fiducial mark and the factory-determined, sub-nm position precision of the PZT stage).

If the trapping and detection beams are far from each other, we first roughly center the trapping beam over the detection beam by hand (using the reflections on the CCD camera); this typically only has to be done once. For fine alignment, we run a VI that automatically scans the trapping beam across the detection beam; first in a line along x and then along y . As the trapping beam moves, it takes the trapped bead with it, and the bead scatters light from the detection beam (Figure 2.11A). Thus, at every scan point we have (1) the real-space distance (in nm) of the trapping beam from its start point, and (2) the QPD x or y voltage signal of the detection beam. Due to the shape of the detection beam and bead, this signal takes the form of a derivative of a Gaussian, an antisymmetric function (Figure 2.11B). The center point of this function occurs when the bead is in the center of the detection beam (for a given scan axis). We therefore fit the

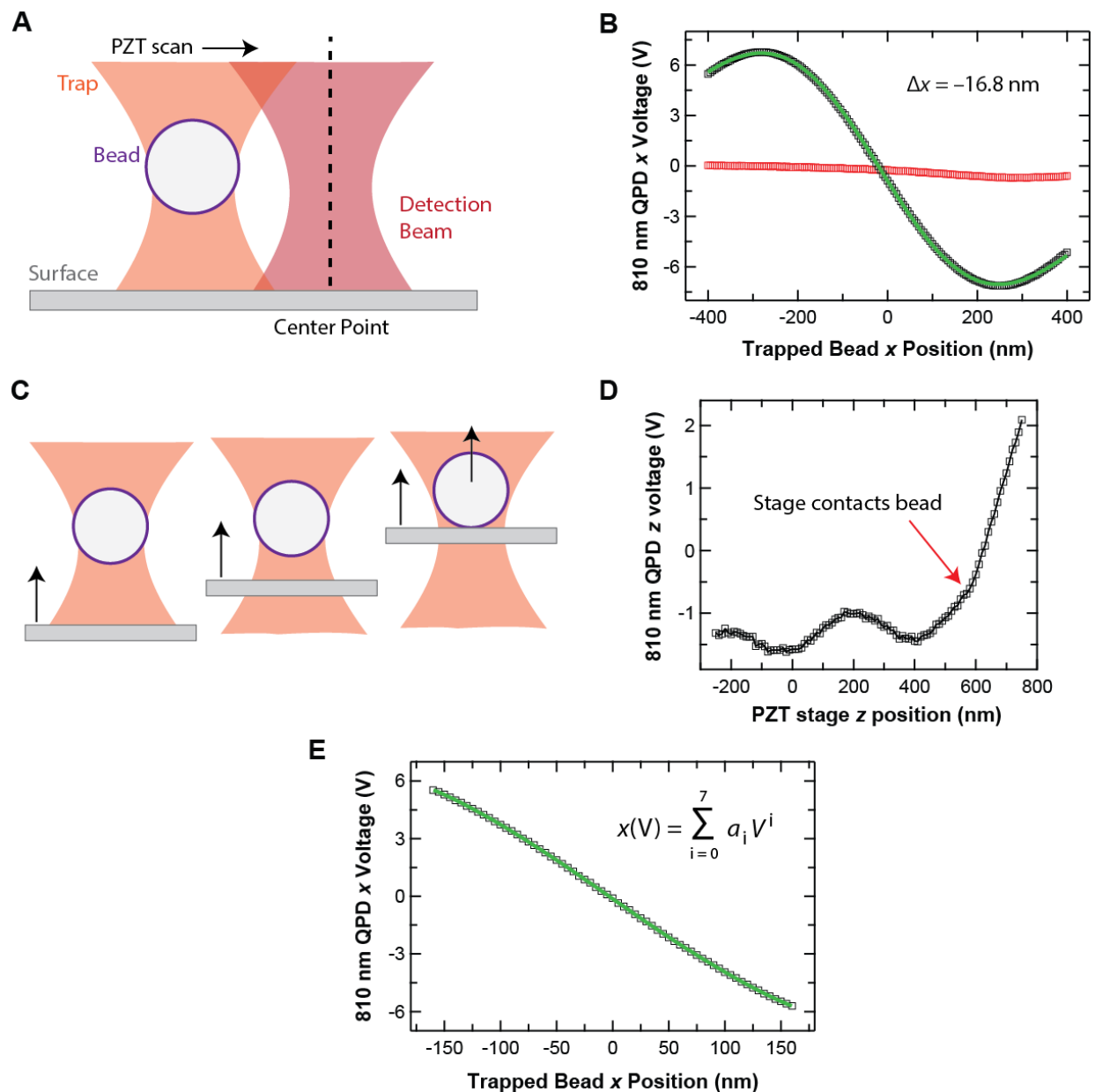


Figure 2.11: Procedures for positioning and calibrating a bead.

A) The beam centering procedure using a trapped bead. The trapping laser (orange) is moved through the detection laser (red) with bead in tow, via a PZT mirror. B) Example trace produced from the procedure. The x QPD signal (black) is fit (green) to find the position difference between the signal's center point and the scan's center point. The off-axis signal (y ; red) is also shown. There should be little crosstalk. C) Setting the bead height above the surface. Using the stage, the surface hits the trapped bead, displacing it, then is brought back down. D) Example height curve. The point of contact between surface and bead is when the signal changes from oscillating to sharply rising. E) A calibration curve for turning QPD voltages into position measurements. The data (black) is fit (green) by a 7th-order polynomial (equation inset).

data to find the position offset (in nm) of that center point, then instruct the trapping beam to move to that location. In this way, we center the trapping beam over the detection beam.

With the bead's (and trap's) xy position set, we next set its z position (i.e., the height of the bead above the surface). This z position will determine the amount of viscous drag on the bead as it diffuses within the optical trap, due to the frictional interaction between the fixed glass surface and the water. The closer the bead is to the surface, the larger the viscosity of the surrounding liquid. Happily, this relationship is quantitatively given in Faxen's Law (37), so as long as we can accurately set the z position of the bead, we will know the surrounding viscosity. For tethered beads, the z position also determines the relative contributions of the lateral and axial trap forces to the total trap force (sections 2.4.3 and 4.1.2).

We set the height by moving the sample chamber surface in z relative to the optical trap center. However, this motion is not completely independent. Recall that the lasers are focused by an objective lens directly before they enter the sample chamber (through immersion oil). Changing the position of the sample chamber affects how close or far it is from the objective lens, and therefore how focused the laser beams are when they enter the chamber. Thus, as the surface moves relative to the objective lens, the absolute position of the beams' foci in space changes (Figure 2.11C). Luckily, the relationship between these motions has been previously worked out (103). The trap center follows the sample chamber's position in a simple 0.2x proportional relation; if the sample chamber rises in z by 10 nm, then the trap will rise in z by 2 nm. Thus, when we want to change the distance between surface and trap center, we simply tell the stage to move 1.2x the desired distance.

To accurately set the height, we scan the PZT stage in z upward a set amount: enough for the surface to contact the bead, begin pushing it out of the trap, and then move back down to a

noncontact position. From that, we get an 810 nm QPD z voltage signal (Figure 2.11D). The signal point where the overall behavior changes (from weak oscillations to smoothly increasing) is where the surface first comes into contact with the bead. Once we have this absolute stage position (in nm), we can easily set the height. We decide what distance we want between the surface and the bead (typically 200-400 nm), and tell the stage to move down 1.2x that distance from the contact point.

With a bead fully positioned in space, our last task is to calibrate the 810 nm QPD voltage signals so that we know the real-space position they represent. This calibration procedure is very similar to the beam centering procedure. We use the 1064 nm PZT mirror to scan the trapped bead in x and y , and record the voltage response from the 810 nm. However, instead of just fitting the response with a derivative of a Gaussian to find an offset, we fit it with a 7th-order polynomial and extract eight calibration coefficients (Figure 2.11E). Now, whenever we collect a QPD voltage signal V_x , we simply multiply powers of it by the eight coefficients to get the real-space position x . With this, the bead is positioned and calibrated.

2.4.2 Trap calibration and linearity

Now that we can measure bead position, we next want to measure the force on the bead. Within the linear region of the optical trap, this force is simply $F = k_T x$, where k_T is the trap stiffness and x is the bead position. Therefore, we need to determine two quantities: the trap stiffness in the linear region, and the extent of the linear region. We calibrate the stiffness semi-frequently because it depends on the intensity and focus of the trapping beam, which can change over time due to laser and optics drift. We check the linearity rarely because, once the linear region is determined, we typically perform experiments far away from the edges of the region so that

linearity is assured. Specifically, the linear region is almost always larger than ± 60 nm from trap center along any axis, and we try to keep the bead within ± 40 nm (the trap stiffness calibration methods let the bead passively diffuse in the trap, reaching ± 5 nm at most).

We calibrate trap stiffness using the equipartition method and the power spectrum method. Since the data collection process for both methods is the same (they differ only in their analysis), we collect a single data set, perform both analyses, and compare the results to ensure consistency. The first step in a k_T calibration is to trap, position, and calibrate a bead. Once that is done, the 1064 nm AOM servo reference voltage V_{AOM} is set to a low value (0.25 V), which correspondingly lowers the trap intensity. The diffusion of the bead inside the trap is recorded for a time (typically for ~ 1.1 s at 120 kHz; Figure 2.12A), then V_{AOM} is increased by some linear increment. This process is repeated eight times, so that there are nine bead diffusion data sets associated with nine V_{AOM} values. The idea in this calibration is to derive a trap stiffness value from each diffusion data set and match it to its corresponding V_{AOM} value. A line is then fit to the k_T vs. V_{AOM} values, and its coefficients extracted (Figure 2.12B). With these coefficients, we can transform any desired k_T value into a V_{AOM} value and send it to the AOM servo board. Since the trap stiffness can differ in the x and y directions, we calibrate both directions and pick a single one to use in any given experiment.

To calculate k_T using the equipartition method, we use the fact that a system in thermal equilibrium with some bulk reservoir has an average thermal energy in each degree of freedom equal to $\frac{1}{2}k_B T$, where k_B is Boltzmann's constant and T is the temperature. The potential energy imparted to the bead by the optical trap counts as one of these degrees of freedom. As mentioned in the introduction, the optical trap forms a harmonic trapping potential, expressed as $\frac{1}{2}k_T x^2$, where x is the distance between the bead and trap centers along some axis, and k_T is the trap

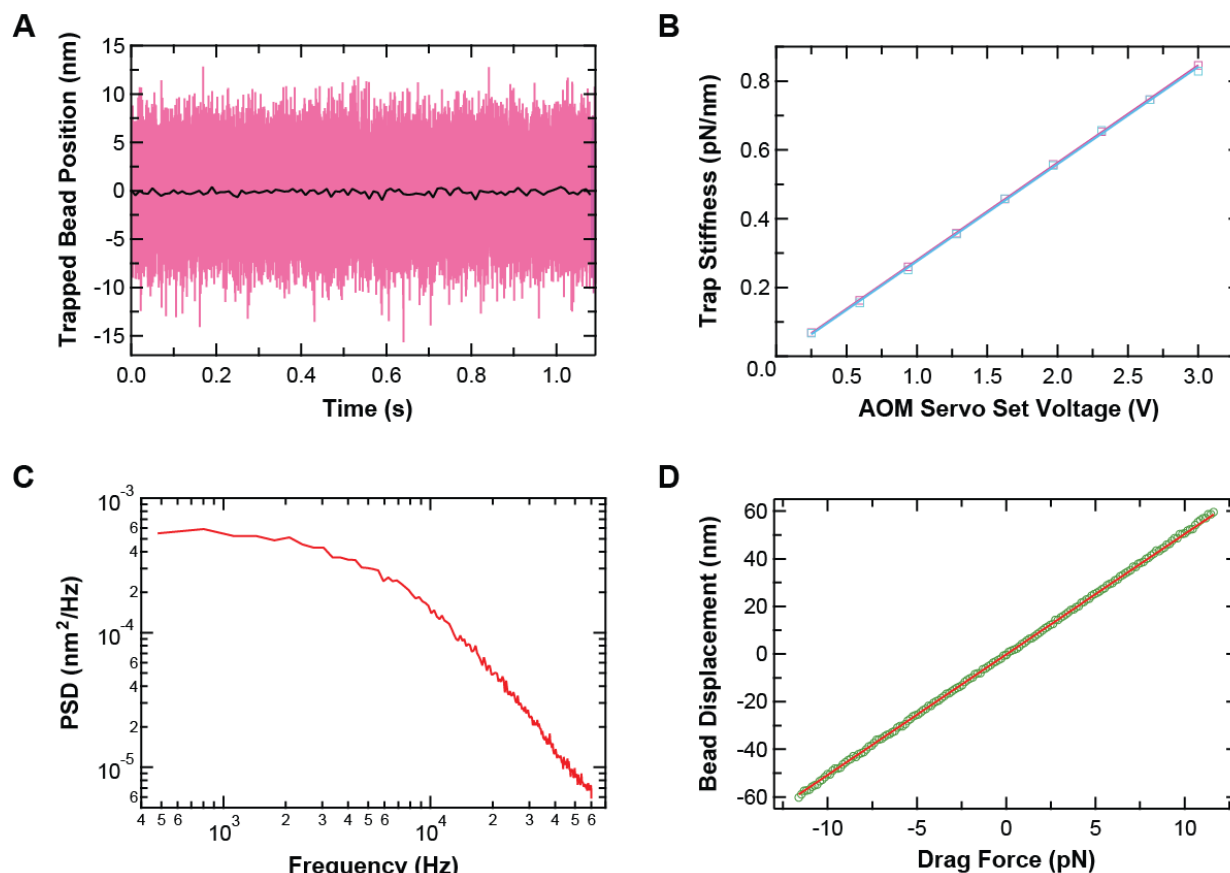


Figure 2.12: Trap stiffness calibration and linearity.

A) An example trace of bead diffusion while trapped in the optical trap. The data was taken using a 750 nm diameter bead, until $131072 = 2^{17}$ points were collected (120 kHz for ~ 1.1 s). Data sets in powers of 2 aid the FFT part of the power spectrum analysis. B) The trap stiffness vs AOM set voltage calibration curves for the optical trap's x-axis, obtained via the equipartition method (cyan) and power spectrum method (magenta). As expected, trap stiffness increases linearly with beam intensity (proportional to set voltage), and both methods agree well. C) The power spectrum of the bead diffusion data in (A), across the analyzed bandwidth. D) A drag measurement of a 750 nm diameter bead along the y axis of the trap. Trap stiffness was set to 0.2 pN/nm, and the drag coefficient was 9.67×10^{-6} pN(s/nm). Trap linearity can be clearly seen, and begins to start falling off near ± 60 nm. Acronyms: AOM (acousto-optic modulator), FFT (fast Fourier transform).

stiffness along that axis. The average potential energy is therefore $\frac{1}{2}k_T\langle x^2 \rangle$, where $\langle x^2 \rangle$ is the bead's position variance. This quantity can be easily calculated from the bead diffusion data, and k_B and T are known. Therefore, we can calculate the trap stiffness k_T .

The power spectrum method calculates k_T differently. We first take the power spectrum of the diffusion data using a Fast Fourier Transform (FFT). In rough terms, taking the power spectrum of a time signal (i.e., the diffusion data) decomposes the signal into its sinusoidal components (its Fourier series), extracts the coefficient of each component (their relative strength), and then plots those coefficients as a function of the Fourier component frequencies; an example for a trapped bead can be seen in Figure 2.12C. Thus the power spectrum, true to its name, shows the relative “power” of each component in the frequency spectrum of a time signal. The power spectrum of a trapped bead has a nearly Lorentzian shape, and can be analytically fit to extract Lorentzian parameters (104). The parameter of interest here is the power spectrum's corner frequency f_0 , the frequency at which the power is reduced to 1/2 the thermal baseline. The trap stiffness can be calculated from this frequency as $k_T = 2\pi\beta f_0$, where $\beta = 6\pi\eta_f r$ is the drag coefficient for the bead (η_f is the dynamic viscosity of the solution corrected by Faxen's law (105, 106) and r is the bead radius). Since both η_f and r are known, the viscous drag on the bead can be calculated, and so the trap stiffness can be derived.

Note that the trap stiffness partially depends on the size of the bead (section 1.1). As there is some size variation in our bead stock (usually ~3% in diameter), there will always be some error in using any one stiffness calibration for a number of different beads (46). This is typically not a problem, as absolute force measurements are not a primary concern in my work. However, for experiments where extreme force accuracy is desired, we typically calibrate the trap stiffness for each bead used (via equipartition, since power spectrum requires an explicit radius input).

Note also that these methods cannot be used to derive the trap stiffness along the z axis, since we cannot calibrate the QPD z voltage into real-space position (without having to manually scan the trapping beam focus through the detection beam). However, this is not a problem, as we only need to know the axial-to-lateral stiffness ratio ($k_{\text{T}}^z/k_{\text{T}}^x$ or $k_{\text{T}}^z/k_{\text{T}}^y$) (section 2.4.3). This ratio can be calculated by performing a power spectrum analysis on uncalibrated bead diffusion data in z and x (or y), and taking the ratio of the Lorentzian fit corner frequencies multiplied by the ratio of the axially corrected drag coefficients (106). When using $r = 375$ nm beads, this ratio is typically 0.5; when using $r = 250$ nm beads, it is typically 0.33.

To measure the extent of the linear region of the trap, we perform a viscous drag assay. In this assay, we trap, position, and calibrate a bead, then move the sample chamber at some fixed velocity along the x or y axis using the PZT stage. As the bulk liquid in the chamber moves, a drag force tries to drag the trapped bead along with the liquid; however, this force is countered by the trapping force. An equilibrium is reached at some position away from trap center, such that the trapping force $F = k_{\text{T}}x$ balances the drag force $F = \beta v$, where β is the drag coefficient of the bead and v is the velocity of the chamber relative to the stationary trap. The position x is measured and recorded, along with the corresponding velocity v . This is repeated at many different velocities, both positive and negative, as the magnitude of v is gradually increased. When completed, we plot equilibrium position vs. sample velocity, as seen in Figure 2.12D. In the linear region of the trap, k_{T} is constant and so there is a linear relation between position and velocity. At the end of the linear region, that relation starts to break down as k_{T} starts to change with position (seen at ± 60 nm in Figure 2.12D). Thus we determine the linear region.

2.4.3 DNA tether centering and calibration

Now that bead force and position measurements can be made, only one more quantity needs to be found before we can study DNA tethers in the trap: the location of the DNA molecule's other end, the surface-DNA attachment point. Figure 2.13A shows the basic geometry of a tethered bead in a surface-coupled optical trap; when an experiment begins, the surface-tether attachment point is located an unknown distance x_{stage} away from the trap center. Once that attachment point is known, geometric calculations can be performed (Figure 2.13B) to convert it, as well as the bead position and force, into the biophysical quantities we care about: the force and extension of the DNA molecule (5). That knowledge can then be used to quantitatively stretch and relax the DNA tether by controllably moving the attachment point relative to the trap using the stage.

We find the attachment point by centering it directly under the trap using a stretching procedure. This completes two tasks at once, since finding the attachment point in this manner also fully relaxes the DNA molecule (minimize tension) and readies the system for further experiments. The DNA centering procedure is identical to the beam centering one in concept: we scan something along the x and y axes, collect antisymmetric signals, and fit them to find their position offset values. Here, we use the PZT stage to move the unknown attachment point along each axis. The process is as follows: we assign the initial PZT stage position an x_{stage} value of 0 and calculate its resulting DNA force and extension (F - x) values. Then we move the stage a certain amount, update the x_{stage} value, and calculate the F - x values again. This is repeated until 10 pN is measured for the DNA force, then the process is repeated in the opposite direction until -10 pN is measured (Figure 2.13C). The position of zero force between the positive and negative force portions when the DNA-surface attachment point is directly underneath the trap. We find this position by fitting the signal with a two-sided worm-like chain (WLC) function which has

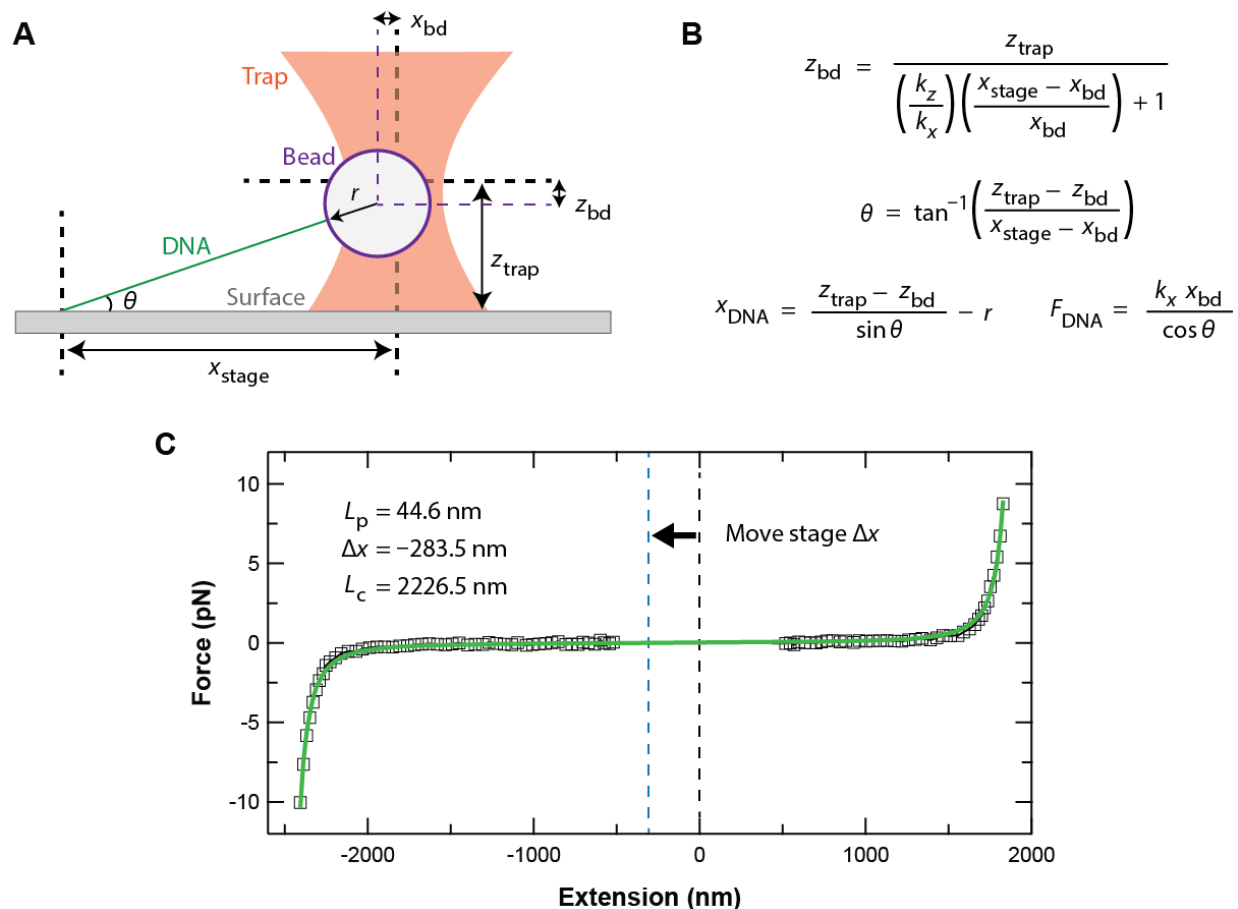


Figure 2.13: Surface-coupled geometry calculations and DNA centering.

A) Cartoon of the surface-coupled geometry used in this optical trap. The bead is pulled out of the trap center by the surface-bound DNA tether. B) Equations for various parameters of interest, given the geometry of (A). Note that these relations only hold true within the linear region of the trap. C) A two-sided, force-extension curve used for centering the DNA under the trap. Data (black) is fit (green) to a two-sided WLC curve. The fit reports the persistence length, extension offset, and contour length.

the zero-force offset value as a parameter. This process is performed on both axes iteratively to center the DNA tether under the trap (often two times is enough to center to ~ 1 nm accuracy). The WLC fit also allows us to simultaneously perform a rough calibration of the DNA tether to see whether it has the expected WLC DNA parameters. Specifically, we fit for the DNA tether contour length L_c and persistence length L_p . If these values are roughly correct, we know the bead is connected to the surface by a single, undamaged DNA molecule. If either value is significantly off, the bead is connected by multiple DNA molecules and/or damaged molecules. In that case, we stop the procedure and move on to a new tethered bead.

Note that the diagram in Figure 2.12A is roughly to scale, and demonstrates why we use DNA lengths of 3000–6000 bp (~ 1 – 2 μm at contour length 0.338 nm/bp). Since the axial-to-lateral trap stiffness ratio is roughly 1/2, the trap is twice as strong in the lateral direction as the axial one. To keep the bead firmly in the linear regime of the trap, we want the majority of the trapping force to come from this lateral force, which means we want to stretch the DNA tether nearly horizontally (small angle between surface and tether).

2.4.4 Overstretching assay

With the tethered bead system fully positioned and calibrated, biophysical experiments can now be performed. One of the most common and useful experiments I run is the overstretching assay. This assay dynamically stretches and relaxes a DNA tether, often through its overstretching (OS) transition. The assay is dynamic in that F - x data is collected *while* stretching takes place (i.e., while the PZT stage is moving), not before or after. In contrast, the DNA centering procedure only collects data after the PZT stage finishes moving. This dynamic nature introduces some timing challenges into the LabVIEW code, as discussed below.

At the start of the assay, we increase the trap stiffness from 0.2 pN/nm to 0.8 – 1 pN/nm, since we want to stretch the tether to a high force but still remain within the linear region of the trap. Unfortunately, increasing the trap stiffness (laser intensity) by so much so suddenly causes the objective lens to thermally expand. This thermal expansion moves the focus of the laser beams, so that the trap center (and thus bead) increase in z position relative to the sample surface. This increase in height, if not accounted for, can make tethers appear shorter than they actually are. This problem can be post-processed out, or mitigated by pre-warming the objective lens before the start of the assay. The trap stiffness *should not* be set higher during the centering and calibration procedures, since the DNA tether can be damaged. Specifically, 1064 nm light can interact with the polystyrene bead to produce reactive oxygen species, which can damage DNA (107). The production rate increases with laser intensity, so we try to only use intense beams when the bead is *not* directly above the whole biomolecule; this way reactive species are more likely to diffuse away than interact with the DNA molecule.

With the trap stiffness set, a long, concatenated GPIB command string is created and sent to the PZT stage controller. This string contains the full stage movement plan for the entire assay: move a set distance at a set speed and either (1) end, or (2) wait and pull back the same distance at the same speed. After this string is sent, the VI starts recording bead position and force data, as well as calculating where the stage should be at each time step. Note that we do not *measure* stage position during this dynamic assay; we infer it from the planned motion as a control parameter. The only time when this becomes a problem is during the wait between the forward and backward stage motion. Since this change in motion involves a lot of acceleration, extra time needs to be added to the GPIB command string to account for the delay imposed by the mechanical limitations of the stage's acceleration. Once the stage finishes its command,

calculated stage data and measured bead data are transformed into DNA F - x data. The raw and process data signals are then saved, along with all assay parameters.

2.4.5 Active force-clamp assay

A force-clamp assay continuously measures the extension of a DNA molecule while keeping the force on the DNA fixed to some value. Keeping the force fixed in this manner ensures that DNA extension changes are solely due to biological processes, and are not convolved with mechanical stretching from force changes. Both passive and active force-clamp procedures exist (26, 108). We typically use active force clamps in this lab, and have two methods: either the force is clamped by modulating the trap stiffness or stage position. Active force clamps work much like the laser and stage servo loops: a reference force is set, DNA tension is continuously measured, and if the current force differs from the reference force, the trap stiffness or stage position is changed to bring the current force back toward the reference.

The benefits of using trap stiffness as the clamp variable are its speed and ease of use due to the 1064 nm AOM servo loop, resulting in a high loop bandwidth (~1-10 kHz). It can also be easily paired with active stage stabilization to further improve detection accuracy. The costs are that the clamp is limited to the trap stiffness's small available range; prolonged force changes eventually cannot be stopped if they require the trap stiffness to exceed this range. Thermal noise also gets added to the system due to the constantly varying trap stiffness, which makes the clamp work even harder. Finally, the trap stiffness in this clamp obviously cannot be set to a stable, high value, which can be very useful for briefly reducing noise (see section 4.1.2). The benefits of using stage position as the clamp variable are its large available range of motion and lack of additional noise. For all systems under study here, stage-based force clamps cannot run out of

range. The trap stiffness is also a free parameter in this setup, allowing for brief noise reduction. The costs are its slower overall bandwidth (~ 100 Hz), due to the fact that changing the stage's position takes much more time than changing the trap stiffness.

To begin a force-clamp assay, the PZT stage is moved in rapid steps until the DNA force reaches the reference force (usually 8 pN). If active stage stabilization is used, the 850 nm beam is then centered over a nearby fiducial mark and calibrated so that its QPD voltage outputs can be read as positions. The force-clamp loop then begins to keep the DNA force within ± 0.05 pN of the reference force. During each iteration of the clamp loop, force and extension data are calculated from raw data and both (raw and processed data) are saved to disk. This process is continued until the loop is manually stopped by the user. If a stage-based clamp is running, the trap stiffness can be manually changed at will, which can be useful during high-resolution experiments as a way to increase signal-to-noise (see section 4.1.2).

Chapter 3

Force-activated DNA substrates

In this chapter, I detail the work performed on force-activated DNA substrates. First, I introduce the rationale for creating such substrates, including how they can improve certain SMFS experiments (section 3.1). Second, I describe two force-activated substrates that we designed, constructed, and validated: a construct that yields 1002 nt of 50% GC ssDNA when activated, and one that yields a 20 bp DNA hairpin and 33 nt of ssDNA when activated (section 3.2). Third, I go through the biophysical experiment we used to demonstrate the efficacy of these constructs: a single-molecule measurement of the on-rate of the *E. coil* RecQ helicase using DNA hairpin substrates (section 3.3). The work described in these three sections can also be found in Ref. (109). Lastly, I detail the more advanced substrates we have made, including 120 bp DNA hairpins with distinct runs of high and low GC content meant to improve %GC-dependent unwinding velocity measurements (section 3.4).

3.1 Introduction to force-activation

SMFS experiments that study protein–nucleic-acid complexes typically rely upon dsDNA as a substrate, and are often initiated by adding a critical component (e.g. nucleotide triphosphates) (110). However, a wide array of proteins, including motor proteins such as translocases and

helicases, may not bind directly to dsDNA, but instead bind to ssDNA and/or to ssDNA/dsDNA junctions. Unfortunately, preparing substrates containing sections of ssDNA within longer dsDNA molecules can be an inefficient process, which hampers their widespread application, particularly for optical-trapping-based assays that require micrometer-scale dsDNA.

An important innovation in high-resolution SMFS helicase studies was the development of the hairpin-unwinding assay (33). In this assay, a long dsDNA molecule containing a short hairpin and a small single-stranded nucleic-acid region is stretched (Figure 3.1A). The single-stranded region is typically slightly larger than the helicase's footprint, so that the helicase binds within a few nucleotides (nt) of the hairpin. Unwinding activity is detected via length changes in the taut DNA substrate. For every 1 base pair (bp) of the hairpin unwound, 2 nt of ssDNA are put under tension. Compared to directly measuring helicase motion along dsDNA (1 bp = 0.34 nm), the hairpin-unwinding assay provides a 3-fold mechanical amplification since the contour length of the taut DNA increases by 1.12 nm (2×0.56 nm/nt) (3, 50). Although initially applied to an RNA helicase (33) and the ribosome (34), such assays have been extended to studies of DNA helicases using both optical traps (111, 112) and magnetic tweezers (101, 113). Unfortunately, the standard protocol for making these substrates involves a three-way hybridization (Figure 3.1B, left) (33), typically a laborious and inefficient process in our hands and others (114, 115). Such assays are additionally complicated by the relatively low throughput of high-resolution optical traps (42) and by fluid flows necessary to initiate unwinding (e.g. introducing ATP).

An alternative way to generate ssDNA is to mechanically denature dsDNA using force. In the first experiment to demonstrate purely force-induced dissociation (i.e. no added chemical denaturants), an atomic force microscope (AFM) was used to rapidly stretch the DNA ($v = 0.15\text{--}3$ $\mu\text{m/s}$) (53). The resulting dissociation of a full ssDNA strand occurred at high force (120–250

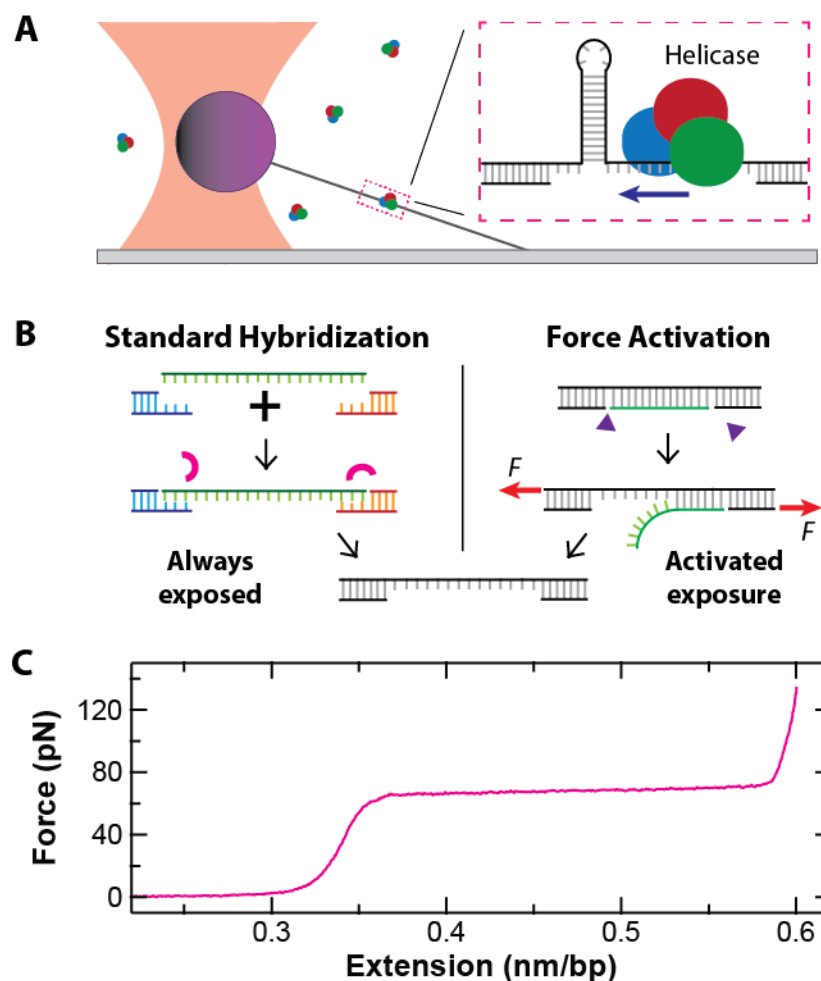


Figure 3.1: Introduction to force-activated DNA substrates.

A) A cartoon of a single-molecule hairpin-unwinding assay using a surface-coupled optical trap. Inset: a DNA hairpin is unwound by a helicase that initially binds to the small segment of ssDNA adjacent to the hairpin. B) Left: the standard method to create ss-dsDNA substrates for such assays is via a three-way hybridization. The small arcs represent ligase molecules. Right: a force-activated substrate contains a pair of enzymatically induced, site-specific nicks located on the same strand. Small triangles represent nicking enzymes. Stretching this dsDNA molecule partway into the overstretching transition induces dissociation. C) A force-extension curve for a 2- μm -long dsDNA molecule shows the overstretching transition at 65 pN as a function of the normalized extension (nm/bp). Reproduced from Okoniewski et al., 2017 with permission from Oxford University Press.

pN, depending on ν) relative to DNA's overstretching transition (65 pN) (3, 4). Recall that DNA overstretching is characterized by a 70% increase in dsDNA extension at 65 pN (Figure 3.1C) and often occurs by force-induced ssDNA dissociation starting from free ends or nicks, commonly referred to as 'peeling' (58, 60, 61). However, previous experiments that pulled dsDNA into and even just past the overstretching transition did not lead to its dissociation into two complementary strands (3, 4, 50, 58-61, 116) (except when the DNA was ≤ 30 bp long (117)). Strand stabilization during and after overstretching is speculated to arise from islands of repeated GC base pairs (54) that suppress local DNA melting and peeling (58, 60, 61). This conjecture explains the much higher forces required to induce strand dissociation in the rapid pulling assay (53, 54) and more recent results where sustained force above the overstretching transition was needed for dissociation (75 pN for ≥ 5 s) (116). This latter protocol, we note, did generate the controlled release of large segments of ssDNA defined by a single site-specific nick. Despite this success (116), several important issues remain in such substrates: (i) high sustained forces can lead to tether failure, (ii) force-activation efficiency decreases under ionic conditions that stabilize base-pair formation (e.g. 150 mM NaCl), and (iii) more sophisticated DNA structures, such as those needed for hairpin-unwinding assays, have not been realized.

To overcome these limitations, we developed two force-activated DNA substrates. In the first substrate (Figure 3.1B, right), a pair of enzymatically introduced nicks were separated by 1 kbp. The 50%-GC sequence between these nicks had no adjacent GC base pairs and, as a result, dissociated when we stretched the construct partway into the overstretching transition. Importantly, the construct contained no ssDNA until activated, providing user-controlled initiation of protein-ssDNA interaction at the single-molecule level. We designed a second DNA substrate to leverage this capability so that we could study helicases using the hairpin-unwinding

assay. Specifically, we sequentially activated individual molecules of this hairpin-unwinding substrate to measure the on-rate (k_{on}) of the *E. coli* RecQ DNA helicase binding to ssDNA, traditionally a difficult parameter to measure in a SMFS assay (101).

3.2 Validation of two force-activated DNA substrates

In the next two subsections, I detail the design, construction, and validation of two force activated DNA substrates: one which activates to reveal 1002 nt of exactly 50% GC ssDNA (section 3.2.1), and one which reveals a 20 bp tetraloop DNA hairpin and 33 nt ssDNA binding site for hairpin-unwinding assays (section 3.2.2). The construction of these substrates follows the general scheme laid out in section 2.3.1, with important differences pointed out as needed. The substrates were validated using the overstretching assay described in section 2.4.4. Detailed protocols on substrate construction can be found in the supplementary material of Ref. (109).

We analyzed the resulting force-extension curves by fitting the total extension as a sum of dsDNA and ssDNA extensions, using the Odijk eWLC for dsDNA (5, 118) and the extensible freely-jointed-chain (eFJC) for ssDNA (3). Our goal was to determine the amount of ssDNA generated after force activation. To constrain the fits, we fixed the dsDNA component of the total extension (using 0.338 nm/bp and the expected number of base pairs in the construct). This was necessary for accurate fits, since the dsDNA component was so much larger and would dominate the fits if left variable. We then fit for the ssDNA extension in both the initial and post-activation curves, which yielded ssDNA contour length values. The difference between the fitted ssDNA contour lengths yields the number of ssDNA nt created, while also removing any absolute offsets due to variability in bead size and linker length. In this process, we fixed the persistence length (L_p) and stretch modulus (S) for ss and dsDNA (ssDNA: $L_p = 0.75$ nm and $S =$

800 pN; dsDNA: $L_p = 45$ nm and $S = 1200$ pN). For the hairpin construct, we also took into account the hairpin's finite width of 2 nm. The reported uncertainties are the standard deviations in the fitted parameters as calculated by the fitting routine (WaveMetrics, Igor Pro 6).

3.2.1 1002 nt 50% GC substrate

We hypothesized that efficient strand dissociation at 65 pN could be promoted by engineering out GC islands. To do so, we developed a 1002 bp target sequence that had 50% GC content but no adjacent GC base pairs (i.e. strictly alternates between GC and AT base pairs). The exact sequence was designed using custom software that produced one hundred ten-bp segments by randomly selecting bases to insert into each AT or GC spot. The full sequence was then run through an autocorrelation routine to ensure no large sequence complements existed that could yield stable secondary structure formation. For this proof-of-concept demonstration, we chose a 1000-bp segment so that we balanced the cost of synthesis with investigating a sufficiently long DNA segment that would exhibit expected overstretching characteristics. Dissociation of this 1000-bp target sequence was facilitated by a pair of enzymatically induced, site-specific nicks (via restriction enzymes Nt.BspQI and Nb.BsmI), as shown in Figure 3.2A. The recognition site for Nb.BsmI added 2 nt to the 50%-GC sequence. This full sequence was ordered from Genscript (Piscataway, NJ, USA). To facilitate optical trapping, GC-clamp sequences and traditional endonuclease recognition sites (PflmI and BbsI) were added so that this designed sequence could be ligated into a larger construct.

This larger construct, consisting of a 1667 bp 'left handle' and a 3670 bp 'right handle,' was assembled from sections of the M13mp18 plasmid. Briefly, we individually polymerase chain reaction (PCR) amplified and purified the left handle, right handle and 50%-GC segments.

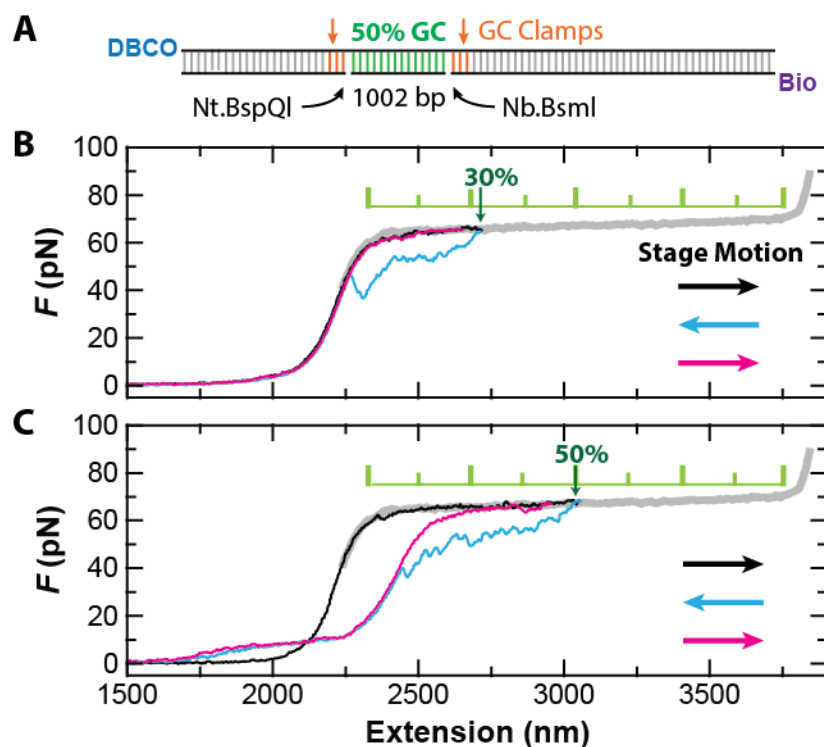


Figure 3.2: Forced dissociation of a 1002-nt DNA segment at ~65 pN.

A) Substrate schematic showing the 1002-bp 50% GC segment, nick sites, GC clamps, and 5'-end labels. Nt.BspQI and Nb.BsmI are enzymes that introduce site-specific nicks. B) A set of three sequential force-extension curves at 2 $\mu\text{m/s}$ pulling velocity shows hysteresis in the stretching cycle. However, no permanent ssDNA strand dissociation is observed when stretching the DNA molecule only 30% of the way through the overstretching transition (black). The stage motion was reversed immediately to relax the DNA to zero force (cyan), and then stretched again (magenta). C) A similar set of three force-extension curves, but with successful force-activation (identified by the permanent contour length changes observed in the cyan and magenta traces). ssDNA dissociates when the construct is pulled 50% of the way through the overstretching transition. The thick gray curve is a representative full overstretching curve. Reproduced from Okoniewski et al., 2017 with permission from Oxford University Press.

The PCR products of the left handle and the 50%-GC sequence were then cut at their PflmI endonuclease sites, combined together at an equimolar ratio and ligated. The purified ligated product and the right handle were then cut with BbsI and ligated together. We then cloned this fully ligated construct into a bacterial plasmid. The plasmid was transformed into competent *E. coli*, grown up, and isolated. The isolated plasmids were verified by sequencing. Importantly, the above process only had to be performed once. Once the full construct was in a plasmid, it was efficiently produced for single-molecule application via a single PCR followed by site-specific nicking, without the need for any ligation. Specifically, for our optical-trapping application, we used primers that were 5'-labeled with biotin and DBCO, similar to earlier work (99). The resulting purified and 5'-labeled PCR product was then nicked sequentially with the restriction endonucleases Nt.BspQI and Nb.BsmI.

To demonstrate force-activation, we used a pull-relax-pull overstretching assay (section 2.4.4) where the stage was moved at $v = 2 \mu\text{m/s}$. By varying the predetermined stretching distance, we controlled how far into the overstretching transition the DNA was extended (Figure 3.2B,C). As expected, the initial force-extension curve (black) for $F < 40 \text{ pN}$ was well fit by an eWLC model for dsDNA with contour length equal to that of the full construct (Figure 3.3). This agreement shows that the nicked DNA was fully double-stranded prior to force activation.

By pulling our engineered DNA construct halfway through the overstretching transition, we achieved essentially instantaneous dissociation of a 1002 nt ssDNA segment. Notably, rapid force-activation of this substrate required pulling the construct a minimum distance into the overstretching transition. For small ($\leq 30\%$) excursions into the overstretching transition, we observed the canonical hysteresis between the stretching and relaxation force-extension curves for such a dynamic assay (3). This hysteresis was caused by peeling of ssDNA from free ends or

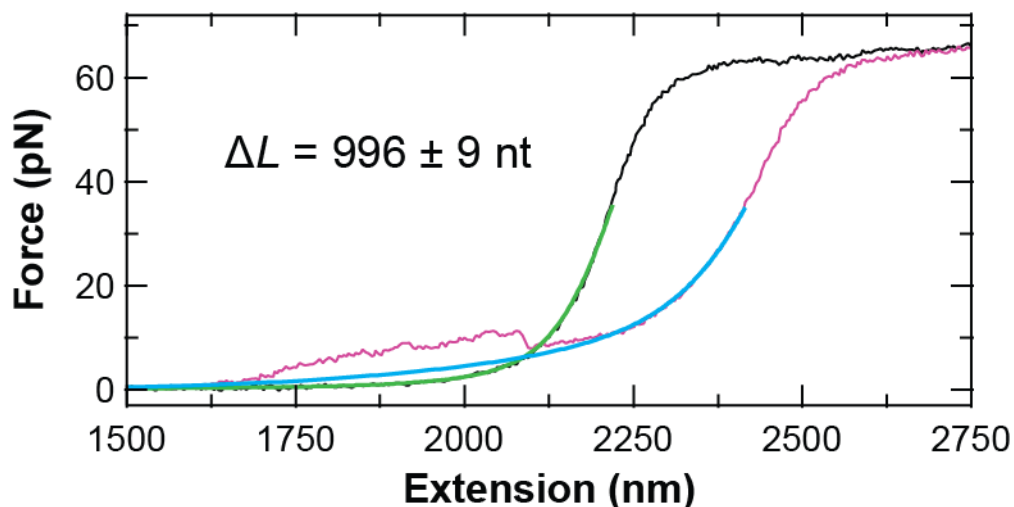


Figure 3.3: Quantifying force activation in the 50% GC construct.

Force-extension curves before (black) and after (magenta) force activation. The initial curve was analyzed using an eWLC model using a fixed dsDNA contour length ($2179.8 \text{ nm} = 0.338 \text{ nm/bp} \times 6,449 \text{ bp}$). The fit (green) to the fully dsDNA construct returned a “ssDNA contour length” value of $32.0 \pm 0.3 \text{ nm}$, which accounted for variation in bead size variation and linker lengths (biotin-streptavidin and silane-PEG-azide-DBCO). The force-extension curve of the activated substrate was fit the same way using a fixed dsDNA contour length of 1841.1 nm ($0.338 \text{ nm/bp} \times 5447 \text{ bp}$). This second fit (cyan) returned a ssDNA contour length of $589.6 \pm 5.1 \text{ nm}$. The difference in contour length was $557.6 \pm 5.1 \text{ nm}$. Using a ssDNA contour length of 0.56 nm/nt , this yields $996 \pm 9 \text{ nt}$ of ssDNA exposed during activation. This finding is in excellent agreement with the expected value of 1002 nt . For consistency, both fits were performed from 15 to 35 pN to avoid the low-force secondary structure unfolding seen in the activated substrate. Model eWLC curves were extended to 0 pN for presentation using the determined parameters. Uncertainties represent best fit \pm s.d. Reproduced from Okoniewski et al., 2017 with permission from Oxford University Press.

nicks, but such peeling intermediates quickly reformed fully duplex DNA once the force was sufficiently reduced (Figure 3.2B, cyan) (58, 59). On the other hand, when the construct was stretched 50% into the overstretching transition (Figure 3.2C), a permanent increase in contour length was observed between the initial and subsequent force-extension curves, a clear signal for activation. To determine the amount of ssDNA generated, we compared WLC fits for the initial and second stretching curves (black and magenta, respectively). This analysis yielded 996 ± 9 nt of ssDNA (best fit \pm SD), in quantitative agreement with the 1002 nt ssDNA expected from our construct (Figure 3.3). Importantly, every DNA construct that completed the more extensive stretching cycle was activated ($N = 22$).

The observed 30% maximum distance into the overstretching transition before permanent strand displacement suggests that peeling from free ends was concurrent with the force-induced dissociation of the target strand at $v = 2 \mu\text{m/s}$. This interpretation is based upon previous work, which showed peeling from free ends or nicks is required for hysteresis while hysteresis is not observed in a topologically closed but rotationally free substrates (59). To be quantitative, this 30% excursion is 2-fold larger than that needed to overstretch just the 1002-bp nicked region. Hence, we expect that there is peeling from the free ends of our construct as well as the site-specific nicks. Such peeling had no adverse effects in this construct, but extra GC clamps could be added to suppress it, if desired.

Beyond achieving efficient generation of ssDNA, these substrates also prove the conjecture that GC-islands lead to strand stabilization during and after overstretching (54). Unlike extensive previous studies that used natural sequences containing GC islands, our substrate had exactly a 50% GC content with no adjacent GC base pairs. Upon stretching, this engineered substrate still exhibited the standard overstretching transition at 65 pN, but we now

observed dissociation of a large strand (1 kbp) halfway through the overstretching transition. Overall, this result, in conjunction with aforementioned 20 years of previous studies on natural DNA sequences, shows that GC islands are critical to strand stabilization. Moreover, we expect that strand dissociation within the 65 pN plateau generalizes to arbitrary lengths of 50% GC segments above a minimum threshold of $\sim 20\text{--}30$ bp (117), though maximum distance into the overstretching transition before permanent strand displacement should vary.

3.2.2 Hairpin-unwinding substrate

Having established our ability to rapidly dissociate large segments of ssDNA, we next focused on forming the more complicated structure needed for hairpin-unwinding assays. To do so, we designed a substrate for a 3'-to-5' DNA helicase that consisted of a 33 nt binding site adjacent to a 20 bp hairpin stem capped by a 4 nt loop. We based the hairpin and binding site sequences on a previously published hairpin (20R50–4T) (20) and previously published oligo (called oligo #3 in Ref. (74)), respectively. Encoding the hairpin into the substrate was a technical challenge, since a 20-bp hairpin within a PCR primer is undesirable (Figure 3.4A). We solved this problem by encoding each half of the hairpin stem, as well as the loop region, into separate PCR primers. Each primer also had one nick site for the endonuclease Nb.BbvCI, and one primer contained the sequence for the helicase landing site. Critically, the restriction site for the endonuclease BstXI was encoded within the loop region of each primer (Figure 3.4B). Each primer was then used to create a separate PCR product, which we referred to as the 'left' and 'right' halves. The BstXI sites on both molecules were then cut, yielding complementary, non-palindromic 4-nt ssDNA overhangs. The left and right halves were then annealed and ligated (Figure 3.4C).

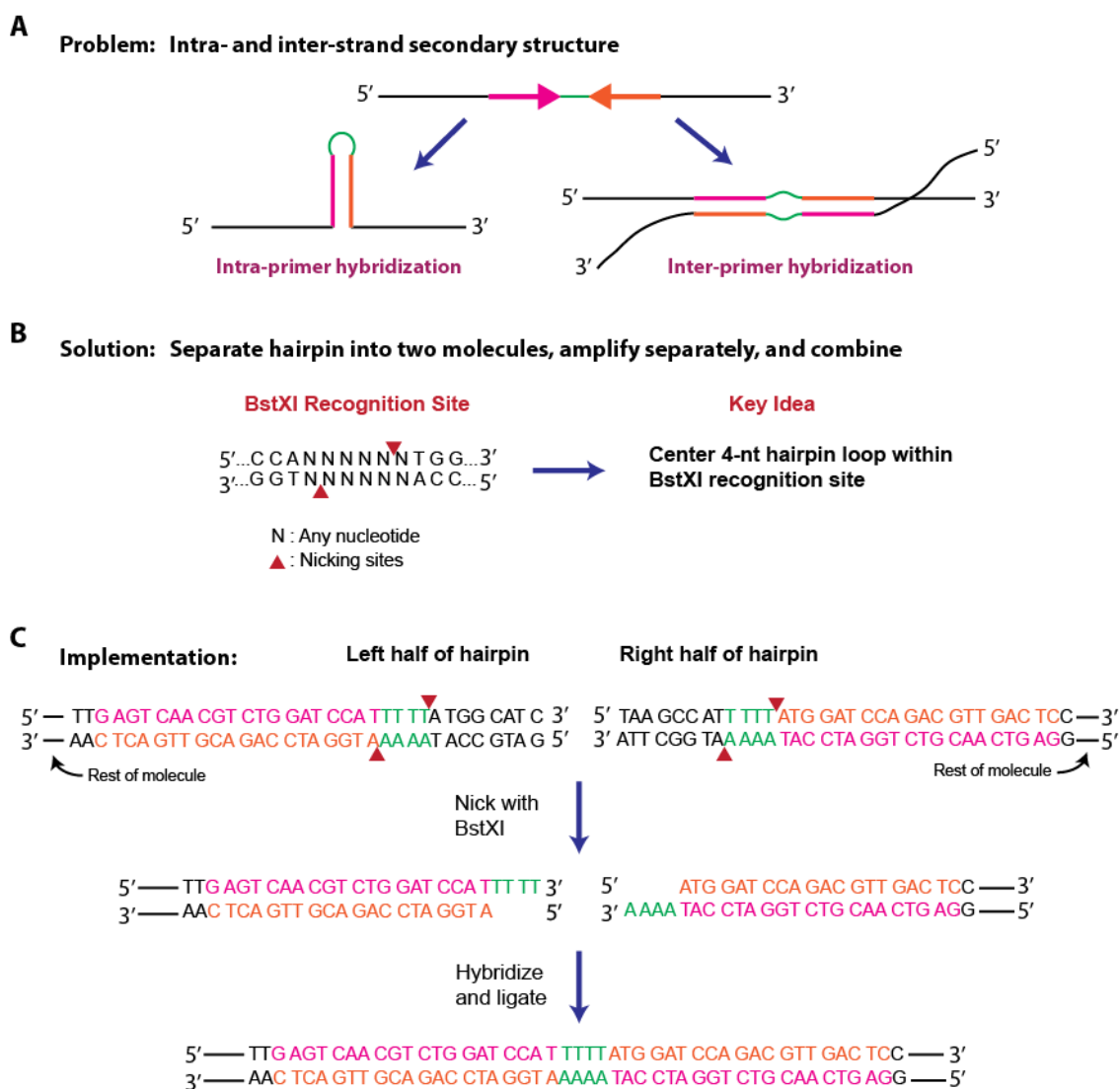


Figure 3.4: Challenges and solution to the 20-bp hairpin construct.

A) Cartoon depicting the challenge of using a PCR primer that fully encodes a hairpin. Specifically, undesirable intra- and inter-strand hybridization will form. Such behavior will negatively impact the subsequent PCR assays. B) To solve this, the hairpin is divided in half using the endonuclease BstXI. Its non-palindromic recognition sequence contains an internal 6-bp that accommodates any sequence, and leaves a 4-nt overhang after cleavage. By using a non-palindromic sequence (TTTT) in this region, self-annealing is avoided. C) Sketch of the steps and sequences used to yield a DNA construct containing an internal hairpin. The two DNA molecules encoding the two halves of the hairpin are nicked and then ligated together. Note, this hairpin sequence contains three instances of two adjacent GC base pairs, which did not interfere with force activation. Reproduced from Okoniewski et al., 2017 with permission from Oxford University Press.

The resulting final construct was inserted into a plasmid for subsequent use as a PCR template. We expect that the formation of a stable intrastrand hairpin within the template strand during PCR extension (~ 70 °C) will limit the length of the hairpin stem that can be produced by this strategy without additional post-PCR enzymatic steps. To improve the strength of the coupling between the DNA and the optically trapped, streptavidin-coated beads, our forward primer contained 4 biotins spaced every 9–10 bp. The reverse primer contained a 5'-DBCO. The 20-bp hairpin had 50%-GC content and the 33-nt section had 58%-GC content. We engineered GC clamps into the shorter dsDNA handle to suppress unwanted fraying. The final construct had a total size of 5529 bp (~ 1.8 μm) (Figure 3.5A).

Since the nicked strand contained only 83 nt, we first wanted to verify that the OS transition was still required for activation. We repeated the rapid stretch-relax-stretch protocol with a peak force of 55 pN, a high force just below the overstretching transition (Figure 3.5B). No hysteresis was observed. Hence, no peeling occurred. Next, we repeated the stretch-relax-stretch protocol but stretched the construct just into the OS transition (7%). In this case, hysteresis and a contour length increase in the force-extension curves was observed (Figure 3.5C). Importantly, folding and unfolding transitions consistent with hairpin formation and rupture were now observed (Figure 3.5C, inset). As expected at $v = 2$ $\mu\text{m/s}$, there was now hysteresis in the force-extension curves at low forces due to the non-equilibrium folding and unfolding of the DNA hairpin, similar to pioneering studies of RNA hairpins (17). We note that substrate activation was successful in 100% of attempts ($N > 300$) at two relatively high ionic concentrations that stabilize base pair formation (150 mM NaCl or 50 mM NaCl + 5 mM MgCl_2). To verify that the proper structure was formed, we analyzed segments of the second stretching curve prior to and after hairpin unzipping (Figure 3.6). This analysis yielded 45 ± 1 nt

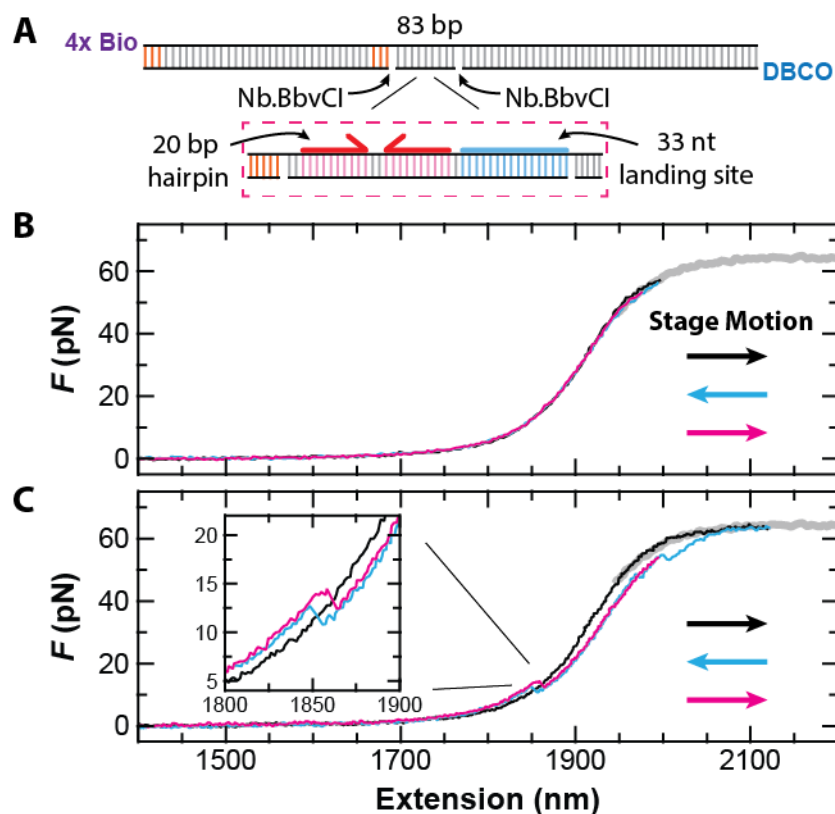


Figure 3.5: Force activation of a DNA hairpin substrate.

A) Schematic of the substrate with a more detailed view of the region around the strand to be displaced. Enzymatically induced nick sites (Nb.BbvCI), GC clamps, and 5'-end labels shown. B) A set of three force-extension curves at $v = 2 \text{ } \mu\text{m/s}$ from a stretch-relax-stretch cycle shows no hysteresis when the maximum force was kept just below the overstretching transition (black, cyan and magenta, respectively). C) A similar set of three force-extension curves but showing force-activation when the construct was pulled just 7% of the way into the overstretching transition. Inset: a magnified view of the force-extension curves shows hairpin folding (cyan) and unfolding (magenta) after activation. As expected, these curves span the initial force-extension curve of the fully dsDNA construct (black). Reproduced from Okoniewski et al., 2017 with permission from Oxford University Press.

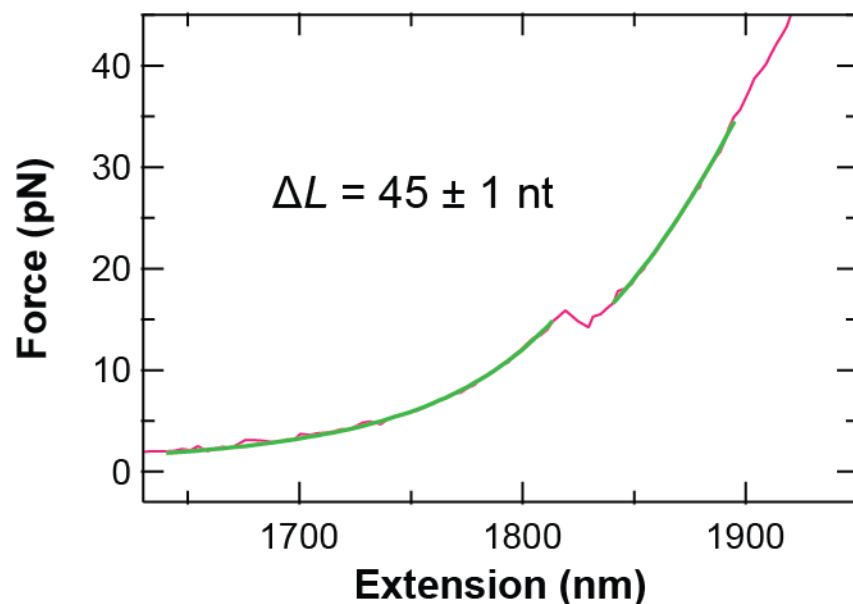


Figure 3.6: Determining the size of the activated hairpin.

A force-extension curve of the activated construct (red) shows a rupture of the hairpin at ~15 pN. The lower (2-15 pN) and upper (17-35 pN) sections were both fit using the same method described for Figure 3.3. Both fits (green) used a fixed dsDNA contour length of $1840.75 \text{ nm} = 0.338 \text{ nm/bp} \times 5446 \text{ bp}$. In addition, the first fit includes a 2-nm offset to account for the diameter of the DNA hairpin. These fits returned ssDNA contour lengths of $26.2 \pm 0.4 \text{ nm}$ and $51.6 \pm 0.2 \text{ nm}$ before and after hairpin unfolding, respectively. The contour length difference was $25.4 \pm 0.5 \text{ nm}$, which corresponds to $45 \pm 1 \text{ nt}$ using a 0.56 nm/nt ssDNA contour length. This result quantitatively agrees with the expected value of 44 nt. Uncertainties represent best fit \pm s.d. Reproduced from Okoniewski et al., 2017 with permission from Oxford University Press.

(best fit \pm SD), in agreement with the expected 44 nt introduced by hairpin rupture. Hence, we generated a valid substrate for the hairpin-unwinding assay via force activation.

3.3 Single-molecule measurement of *E. coli* RecQ on-rate

To demonstrate how force-activated substrates can enhance helicases studies, we measured the rate at which a protein binds to its target, the on-rate (k_{on}), for the *E. coli* DNA helicase RecQ binding to ssDNA. Determining on-rates is traditionally difficult in single-molecule assays (101), in part because the time associated with buffer exchange and flow-induced mechanical perturbations degrades high-resolution assays. Our force-activated substrate assay removed these issues, since we could start with a pure dsDNA construct—our inactive hairpin substrate—stretched to 8 pN and premixed with helicases and saturating ATP [i.e. 1 mM ATP versus $K_M = 16 \mu\text{M}$ (101)]. By rapidly activating the substrate ($v = 5 \mu\text{m/s}$), we can cleanly measure the time t_1 between activation and the start of unwinding (Figure 3.7A) using a 8 pN force-clamp assay (section 2.4.5). As expected, for all measurements unwinding was only observed after activation. The time t_1 is the sum of the time it takes the helicase to bind to the newly created 33 nt ssDNA (t_{on}) and the time it takes the helicase to translocate along ssDNA to the dsDNA hairpin and begin unwinding (t_{trans}). By measuring at saturating ATP but low enzyme concentration, we made t_{trans} small relative to t_{on} (~ 0.3 s vs. ~ 10 s, as the maximum expected $t_{\text{trans}} \approx 19 \text{ nt} / 70 \text{ nt/s}$) (72, 95). Hence, our measurement of t_1 yields t_{on} , which in turn yields $k_{\text{on}} = 1/(\tau_{\text{on}}[\text{E}])$, where $[\text{E}]$ is the concentration of RecQ and τ_{on} is the mean of the t_{on} distribution).

We used *E. coli* RecQ DNA helicase in this study since RecQ is well characterized and can bind to an internal segment of ssDNA prior to unwinding dsDNA (65). Background information on RecQ helicases can be found in section 1.3. To focus on RecQ's helicase activity,

we used a truncated version of RecQ for this assay, RecQ^{ΔH}, which lacks its final domain, the helicase-and-RNaseD–C terminal (HRDC) domain (77). In comparison to wild type RecQ, RecQ^{ΔH} shows no change in processivity nor mechanochemical coupling (93), but removal of the HRDC domain increases ATPase activity by a factor of 2, and weakens binding to ssDNA by a factor of 2–5 (i.e., increased K_D) (72). The buffer conditions used [30 mM Tris-HCl (pH 7.5), 50 mM NaCl, 5 mM MgCl₂, 0.4% Tween-20, 1 mM DTT, and 1 mM ATP] are common for RecQ family helicases, and can be traced back to an early study of human BLM (119).

To determine k_{on} , we measured t_1 at two enzyme concentrations that were much lower than RecQ^{ΔH}'s K_D for ssDNA (90 nM) (72). In this limit, t_1 (and thus t_{on}) should scale inversely with enzyme concentration. Specifically, we measured 70 individual molecules at 200 pM and 67 at 100 pM, all in a single day. Histograms of t_1 were well fit by a single exponential and yielded average values of $\tau_1 = 13.7 \pm 0.7$ s and 26.3 ± 1.8 s (best fit \pm SD) for 200 and 100 pM, respectively (Figure 3.7B). Importantly, our results agreed with the expectation that τ_1 at 100 pM should be twice τ_1 at 200 pM. The dependence of t_1 values on RecQ concentration coupled with the exponential distribution of t_1 at both concentrations shows that the dsDNA hairpin was unwound by a RecQ^{ΔH} monomer rather than a dimer, an ongoing question for RecQ (87, 90) and other helicases (120). Further analysis—assuming $t_1 \approx t_{on}$ —yielded $k_{on} = 3.7 \pm 0.6 \times 10^8$ M⁻¹s⁻¹ (best fit \pm SD), where the reported uncertainty includes both the uncertainty in the fit as well as enzyme concentration. This value for k_{on} is near the ‘diffusion limit,’ the maximum rate at which a molecule undergoing a random walk in 3D can collide with its target (121).

Our single-molecule determination of k_{on} for RecQ^{ΔH} is in close agreement with the one prior measurement from an ensemble stopped-flow assay (95). In that study, 54-nt segments of ssDNA were used as targets, in contrast to the 33-nt segment in the present work. Our value for

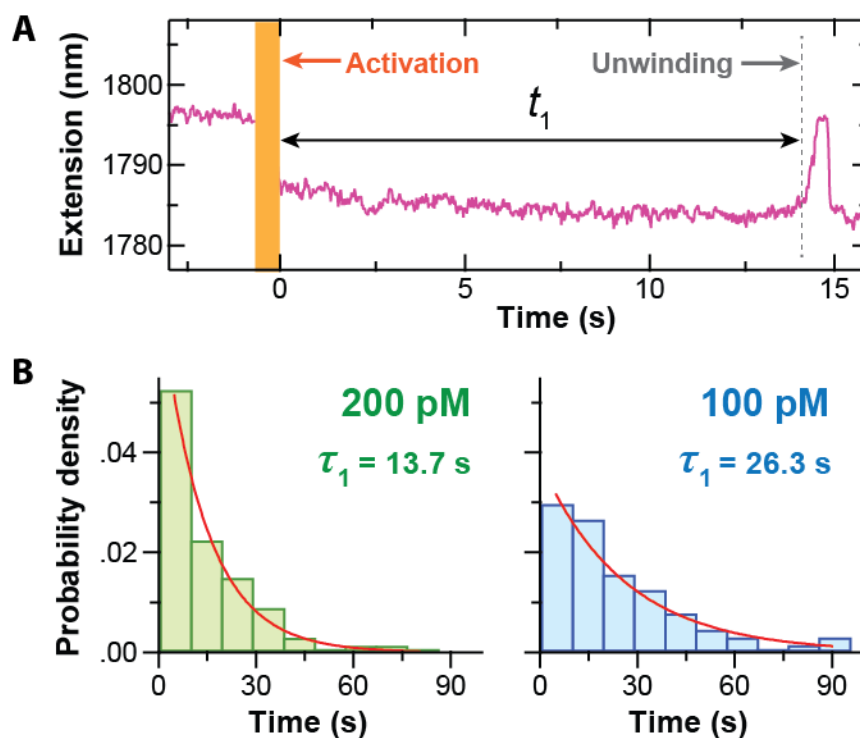


Figure 3.7: Force-activation enables an efficient single-molecule on-rate assay.

A) An extension vs. time trace prior to and immediately after force activation of the hairpin-unwinding substrate in the presence of RecQ^{ΔH} and saturating ATP. After a time t_1 , unwinding of the newly created hairpin led to an increase in extension when measured under constant load ($F = 8$ pN). Note, the decrease in extension after activation matched the expected value (10 nm). Activation occurred in ~ 0.5 s (orange bar). B) The normalized histograms of t_1 at two different enzyme concentrations well below the KD of RecQ^{ΔH} for ssDNA. An exponential fit to the histograms yielded the average time, denoted τ_1 . All the data were acquired in a single day [$N = 70$ at 200 pM and $N = 67$ at 100 pM]. Reproduced from Okoniewski et al., 2017 with permission from Oxford University Press.

k_{on} is ~ 1.5 -fold larger than the previous determination (see supplemental material of Ref. (109) for in-depth calculation). Potential causes for this difference—albeit a relatively small one for a kinetic parameter—include the taut conformation of our ssDNA and the fact that it is flanked by long dsDNA handles, which could facilitate the diffusional search process (121).

One way our force-activated hairpin-unwinding assay can be improved is by decreasing the activation time (currently 0.25 s). The fundamental limit for this time is set by the round trip time of the stretch-relax cycle. This limit varies with stretching velocity and distance traveled by the stage motion. For the present construct held at 8 pN, the round trip distance was 1000 nm. Shorter constructs would decrease this time and are also advantageous since high-resolution assays benefit from stiffer linkers. In addition, future work is needed to fully investigate the velocity dependence of force activation, as we found that a small percentage (30%) of the 50%-GC substrates failed to activate when pulled halfway into the overstretching transition at 20 $\mu\text{m/s}$, whereas all of the substrates activated at 2 $\mu\text{m/s}$.

3.4 Advanced substrates and %GC-dependent unwinding velocity assay

With the concept of force-activated substrates well-demonstrated, we decided to create more advanced versions of the hairpin substrate. The first improvement we focused on was increasing the stem length: 20 bp is sufficient for many assays, but longer stems are often better. However, we did not want to increase the length so much that the PCR reactions would start failing. We decided that doubling the stem length to 40 bp would be a good first step. Following the process laid out in section 3.2.2, we generated this new construct. Happily, increasing to 40 bp stems was easy; no reduction in PCR efficiency or end product formation was observed, and all new substrates force-activated successfully. So, in the same vein, we also generated a reverse version

of this construct for 5' to 3' helicase unwinding. This simply involved switching the location of the ssDNA landing site from downstream of the hairpin (for 3' to 5' motion) to upstream of it. As expected, this construct worked just as well as its sister substrate, and both became our new standard, general-use substrates for helicase studies. With the hairpin stems successfully extended, we next pursued whether the GC content of the stem could be increased while still maintaining successful activation.

To that end, we designed two 20 bp hairpins with increased GC content, one with 66% GC and one with 75% GC. To our mild surprise, both could be made and successfully activated. With these substrates, we intended to perform RecQ unwinding assays to measure %GC-dependent unwinding velocities and compare our results to previously published values (122). Unfortunately, this proved difficult, as RecQ often does strange things when within ~8 bp of the base and top of hairpins (see sections 4.2 and 4.3). For a 20 bp hairpin, this leaves little room for clean unwinding. We thus decided to increase their stem lengths to 40 bp, as above. After testing, it was clear that the 40 bp 66% GC substrate activates successfully while the 40 bp 75% GC does not. The obvious explanation is that this length and %GC is too much for the overstretching transition to easily peel away, which is not entirely surprising, since the GC clamps we use to explicitly prevent peeling in other parts of the substrate are around this length and GC content (~30 bp of 80% GC DNA, c.f. Figure 3.2A).

As development on the above constructs progressed, we designed a more advanced force-activated hairpin for unwinding velocity measurements: a hairpin that has multiple, distinct sections of GC content within a single stem. This substrate would improve unwinding velocity measurements in several ways: (1) it would enable faster data collection since multiple %GC regions are contained in a single substrate, and thus a single data trace; (2) the data from those

different GC regions would be directly comparable in the clearest way possible, since they are plainly from the same molecule in the same buffer conditions; (3) and as before, it would enable controlled data collection since the substrate must be activated. The second benefit is of special note, since many enzymes possess static heterogeneity, meaning that any given batch of the enzyme can have several sub-populations which behave differently from each other, such as having different catalytic speeds or binding properties (this is likely due to the sub-populations having slightly different folded structures) (123, 124). Using a substrate that can internally compare the %GC-dependent unwinding of single members of each of these sub-populations could be a great aid to data clarity.

Using our knowledge from previous constructs, we designed these substrates using 40 bp building blocks. Specifically, the main construct has three 40 bp sections in a row: the initial and final 40 bp of DNA have 50% GC content, while the middle 40 bp has 0% GC (all AT base-pairs). In addition, a control construct was designed with 50% GC all the way through (Figure 3.8A,B, top). Generating these 120 bp force-activated hairpin substrates was more complicated than prior constructs, since they could not be put into a single plasmid; the longer hairpin would be nearly impossible to melt during a normal PCR reaction. To accommodate this, the order of events was slightly changed (c.f. Figure 3.4C). Instead of ligating everything together and inserting it into a single plasmid, the two hairpin halves (and their associated DNA handles) were each placed into plasmids and PCR amplified. The final hairpin ligation step at the loop was then performed after all PCRs were completed. While this process makes the construction slightly harder and less efficient, it did successfully produce the substrates.

Once the 120 bp hairpin constructs were gel purified, we tried to activate them using the same kind of pull-relax-pull overstretching assay as before. Noticeably, not all of the molecules

could be activated. Some tethers just did not activate, no matter how many times and how far into the OS transition they were pulled. In clear contrast, the molecules that did activate usually did so quickly and easily. While the cause of this disparity is not fully understood, the simplest explanation is that the DNA nicking was not completely efficient, leaving some molecules with either one or both of their restriction sites un-nicked (gel assays support this interpretation). Roughly 25% of the molecules tested from both the 50-0-50% and 50-50-50% batches could not be activated. While suboptimal, this only made the process of the data collection a little slower, as non-activated molecules were quickly abandoned for new ones. For the tethers that did activate, their F - x curves look as expected for both types of substrates (Figure 3.8A,B, lower). For the 50-0-50% substrate, the 120 bp hairpin unzips in two distinct steps: the first 80 bp of the stem open at once, then the final 40 bp (confirmed by contour length fits). On the other hand, the full 50% GC hairpin does not have multiple distinct pops, but instead smoothly unzips until reaching a final barrier which is popped open.

With the substrates made, we next sought to demonstrate their previously listed benefits in a helicase unwinding velocity assay. For this, we used the 50-0-50% substrates and the RecQ^{ΔH} helicases used in section 3.3. Prior measurements of how RecQ^{ΔH} unwinding velocity varies with GC content have been made (122), and we sought to reproduce these findings within a single substrate. To do this, we used saturating ATP (1 mM) and recorded RecQ^{ΔH} unwinding the hairpin (Figure 3.8C). The full unwinding of 120 bp roughly equals a total extension change of 90 nm in our 8 pN force clamp; 30 nm per 40 bp section. We chose to break up this total extension change into 10 nm sections for analysis. As stated above, RecQ can do strange things while near the base and top of a hairpin. Therefore, the first and last 10 nm sections of an unwinding trace were excluded from analysis. For a fully unwound hairpin, this left four 10 nm

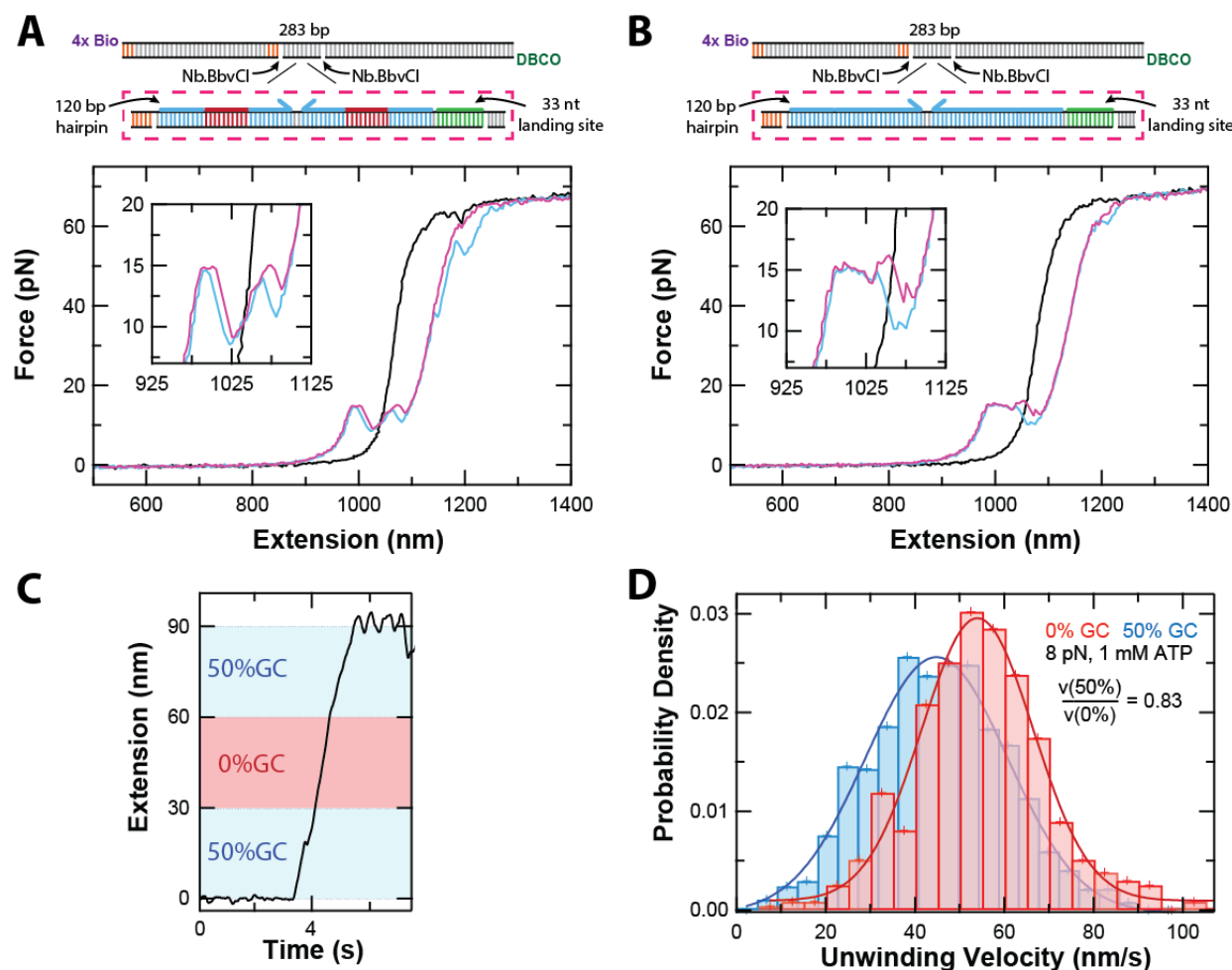


Figure 3.8: Design and application of 120 bp force-activated hairpin substrates.

A) Top: Diagram of the 120 bp hairpin substrate containing 40 bp of 50% GC, 40 bp of 0% GC, and 40 bp of 50% GC. Everything else was kept similar to the 20 bp hairpin design. Bottom: Force vs. extension traces of the hairpin's successful activation. The hairpin was found to zip / unzip in two sharp jumps due to the 40 bp of 0% GC. B) The same information, but for the 120 bp hairpin containing only 50% GC. Here the hairpin was found to zip / unzip in one sharp jump and one continuous annealing / peeling event. C) Example trace of RecQ-dH unwinding the 50-0-50 %GC hairpin at saturating ATP. Each GC region corresponded to 30 nm of extension change while held in an 8 pN force clamp. D) Histograms of average unwinding velocities along 10 nm stretches of the 0% GC (red, N=470) and 50% GC (blue, N=823) regions. Both distributions were fit with Gaussians and their mean velocities recorded. The ratio of the 50% GC mean velocity to the 0% GC mean velocity is 0.83.

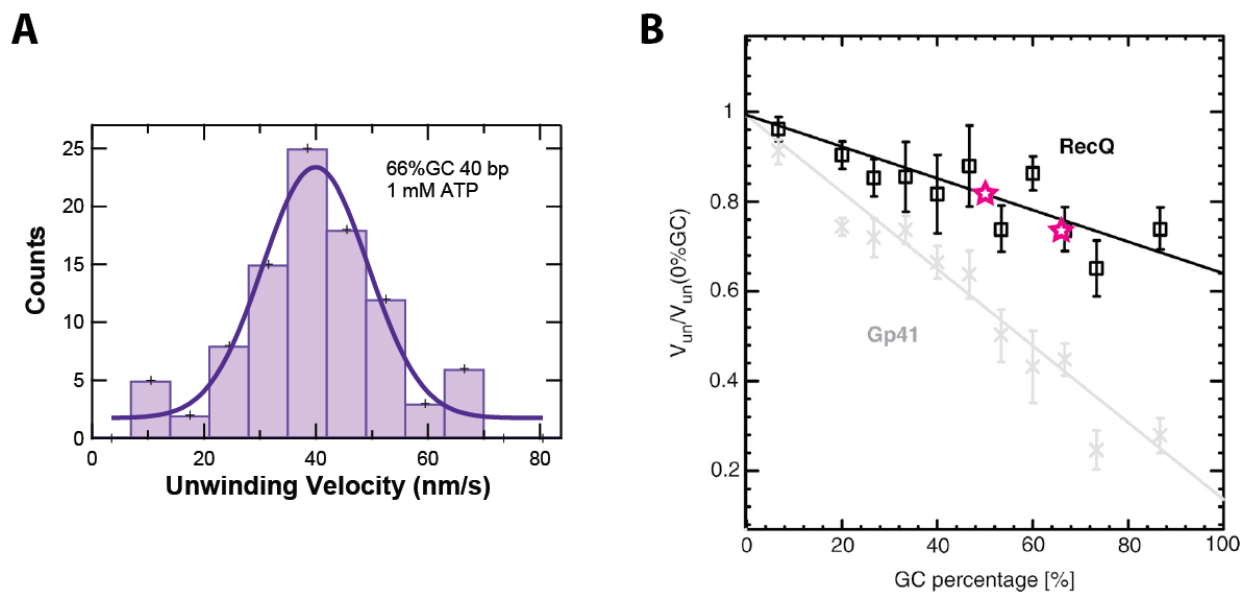


Figure 3.9: 66% GC unwinding velocities and validation.

A) Histogram of mean RecQ unwinding speeds on a 40 bp 66% GC hairpin. Data was analyzed exactly like the histograms in Figure 3.8D. B) Plot of RecQ unwinding velocity ratios vs. %GC content from a prior assay given in black. The 50% / 0% and 66% / 0% ratios collected with force-activated substrates are plotted as magenta stars. Figure reproduced from Manosas et al., 2010 with permission from Oxford University Press.

sections of 50% GC unwinding and three sections of 0% GC unwinding. From each of these sections, a simple linear slope was calculated (total extension change / total time). The resulting velocity values were then binned into histograms based on GC content (Figure 3.8D; 0% GC histogram N = 470, 50% GC histogram N = 823). These histograms were fit with Gaussians to extract their mean values: 54 ± 0.5 nm/s for 0% GC, 45 ± 0.5 nm/s for 50% GC (best fit \pm fit error). The ratio of these two values is 0.83 ± 0.01 , which agrees extremely well with the previously found value of 0.82 (Figure 3.9B) (122). As a final coda for this investigation, we also collected a data set of RecQ^{AH} unwinding velocities using the 40 bp 66% GC hairpins, so that the higher than average GC content substrates could be demonstrated as well. This unwinding data was analyzed from two 10 nm bins (5-15 and 15-25 nm), but otherwise was collected exactly as above. The distribution, while containing fewer points than the 0% and 50% GC data sets (N = 94), still turned out Gaussian, and its fit produced a mean value of 40 ± 1 nm/s (Figure 3.9A). The ratio of this unwinding velocity with the 0% GC velocity is 0.74 ± 0.02 , again in excellent agreement with the previously found value of 0.76 (Figure 3.9B).

Such excellent agreement with prior work shows that these advanced force-activated hairpin substrates do function as intended, and can be used to enhance DNA unwinding assays. As before, data was straightforward to collect, and most of the data sets were collected in single day sittings. It should be noted that, while the unwinding velocity ratios agreed very well with prior work, the absolute values of the velocities differed by around 20%. For example, our measured velocity at 0% GC was 54 nm/s, while in the prior work it was ~ 67.5 nm/s. However, this difference is to be expected, as the assay conditions differ slightly between our work and theirs. The most prominent difference is the temperature difference between the two assays: our unwinding took place at 22 °C, while in the prior work the temperature was 29 °C. Another

difference is the force across the DNA during the unwinding: we used 8 pN while the prior work used 9 pN. Both of these differences would lead to faster unwinding taking place in the prior work, relative to ours (as observed).

Chapter 4

RecQ helicase unwinding

In this chapter, I explain the work done to examine the detailed unwinding behavior of the *E. coli* RecQ helicase, given the establishment of force-activated DNA substrates and monomeric RecQ unwinding in the last chapter. First, I detail this chapter's major drive: the quest to resolve the fundamental physical step size of RecQ (section 4.1). I next present some of the interesting behaviors that were observed while studying the step size: the ATP-less unwinding or “popping” RecQ can perform (section 4.2) and some of the more exotic binding events RecQ can initiate, including rapid strand switching (section 4.3).

4.1 The physical unwinding step size

In this section, I cover the investigation into RecQ's fundamental physical step size. First, I review the information known about RecQ's stepping behavior (section 4.1.1). Then, I explain the many optimizations that must be done to achieve the signal-to-noise (S/N) needed for a successful stepping assay, both to the trapping instrument (section 4.1.2) and the biochemical solution conditions (section 4.1.3). Finally, I present the final stepping results achieved in this instrument: my collected data support RecQ having a 1 bp forward and backward step size, and do not support the more exotic stepping models proposed by other papers (section 4.1.4).

4.1.1 Introduction to RecQ stepping

As stated in section 1.3, the exact mechanics of how RecQ performs its fundamental function, dsDNA unwinding, are still unclear. Given that RecQ is an SF2 helicase with two RecA-like domains, it likely has a physical translocation step size of 1 nt when moving along ssDNA, analogous to other SF1 and SF2 helicases (68). However, this 1 nt physical translocation may not directly translate into 1 bp unwinding. As seen in Figure 1.4C, RecQ most likely keeps the ss-dsDNA junction under tension, and pulls the connected ssDNA such that the duplex slides out of the binding site and splits apart. The question is whether, for a given 1 nt translocation step, the duplex always unwinds 1 bp.

Bulk biochemical studies of RecQ have repeatedly found a chemical unwinding step size of 1 bp (71, 72, 87). In other words, they have found that, on average, 1 bp is unwound for every 1 ATP hydrolyzed by the enzyme. Note that this is only a bulk average; it does not say whether or not 1 bp is unwound for *each* ATP hydrolyzed. Some translocation steps could result in no unwinding, while others could result in multiple base pairs unwinding once the tension across them is too great. Such a mechanism could explain the multiple RecQ unwinding step sizes observed in a recent FRET study (92), although the paper itself offers a different interpretation: they posit RecQ can occlude nucleotides as they are unwound, releasing them later. Supporting this hypothesis, our collaborators at the NIH believe they have observed a 5 bp kinetic step size for RecQ due to occlusion effects (91).

Thus, the mechanics of RecQ's unwinding remain unclear, and a high-resolution optical trapping assay could help illuminate them. Furthermore, given that RecQ is the representative member of the RecQ helicase family, one of the major families within helicase superfamily 2,

uncovering the mechanics of how this helicase performs its basic function is of fundamental interest. We therefore decided to investigate RecQ unwinding in high resolution, focusing on the truncated version RecQ^{AH} for simplicity, since its helicase properties are the same as the full-length, wild-type enzyme, while its binding properties are much simpler (see section 1.3).

4.1.2 Optimizing optical trapping conditions

Obtaining 1-bp resolution in any stepping assay is a very difficult task. Almost every aspect of the measurement has to be optimized, since the expected signal from the enzyme step is so low compared to the overall noise of the system (largely from thermal noise). In this section, I explain the parameters that determine both the signal and noise in a surface-coupled optical-trapping stepping assay, and what must be done to increase the signal and decrease the noise.

For a single DNA held under tension, the signal obtained from helicase unwinding will be some change in both DNA force and extension. For reasons detailed later, extension is by far the better signal to use. Since helicases unwind dsDNA into ssDNA, we should be able to quantify unwinding changes using the eWLC and eFJC, the models which predict the F - x relationship of dsDNA and ssDNA, respectively (Figure 4.1A). Exactly how we implement these models depends on the geometry of the DNA substrate used. For example, say we measured RecQ unwinding with a gapped DNA substrate (such as the 1000 nt force-activated construct in section 3.2.1), where every 1 bp of dsDNA unwound leaves behind 1 nt of ssDNA under tension; let's set the tension to 8 pN. The expected signal for this process is then $0.376 \text{ nm} - 0.322 \text{ nm} = 0.054 \text{ nm}$ (adding 1 nt and subtracting 1 bp): in other words, half an Angstrom. That signal is very small, so unsurprisingly gapped DNA substrates are not used in stepping assays. The best geometry currently available is the hairpin assay: unwinding 1 bp of the hairpin stem releases

two nt of ssDNA into the larger tether, while keeping the hairpin stem width fixed. At 8 pN, this gives an extension signal of 0.75 nm, a 15x amplification over the gapped DNA geometry. This is the DNA substrate type used here, and the first optimization for increased stepping signal.

Substrate tension is the only other parameter that directly impacts the signal. As seen in the F - x models, the higher the force across the substrate, the larger the extension values for both dsDNA and ssDNA. Since larger ssDNA extension produces larger unwinding signals, high substrate tension is clearly desirable. However, there is an upper limit to force in a hairpin assay: the force at which the hairpin unzips. If the tension across the hairpin reaches or even nears that force, the hairpin can immediately unzip and all further unwinding signal is lost. For the 20–40 bp stem hairpins detailed in Chapter 3, this opening force is ~15 pN. For safety, the highest force across these substrates should be ~12 pN. Yet we cannot immediately pick that value as the unwinding force, because force also affects assay noise, not just signal. This choice is dealt with at the end of the section, after the other noise sources have been described.

That said, we can note that without a force clamp the tension in any unwinding assay will constantly lower as new ssDNA is added into the tether, since adding more length produces more slack. Moreover, the amount the force lowers by depends on the full tether length, and thus *changes* after every unwinding step. These length-dependent, non-constant force changes are why force is not used as the signal in unwinding assays. Furthermore, even minor reductions in tether force can reduce the extension unwinding signal dramatically. When a 1 bp step releases 2 nt of ssDNA into the larger tether, it instantaneously reduces the tension across the rest of the dsDNA tether (~3000 bp), attenuating the overall extension increase. To get a quantitative understanding of how, I created a simulation of a DNA hairpin substrate held under tension in a surface-coupled optical trap.

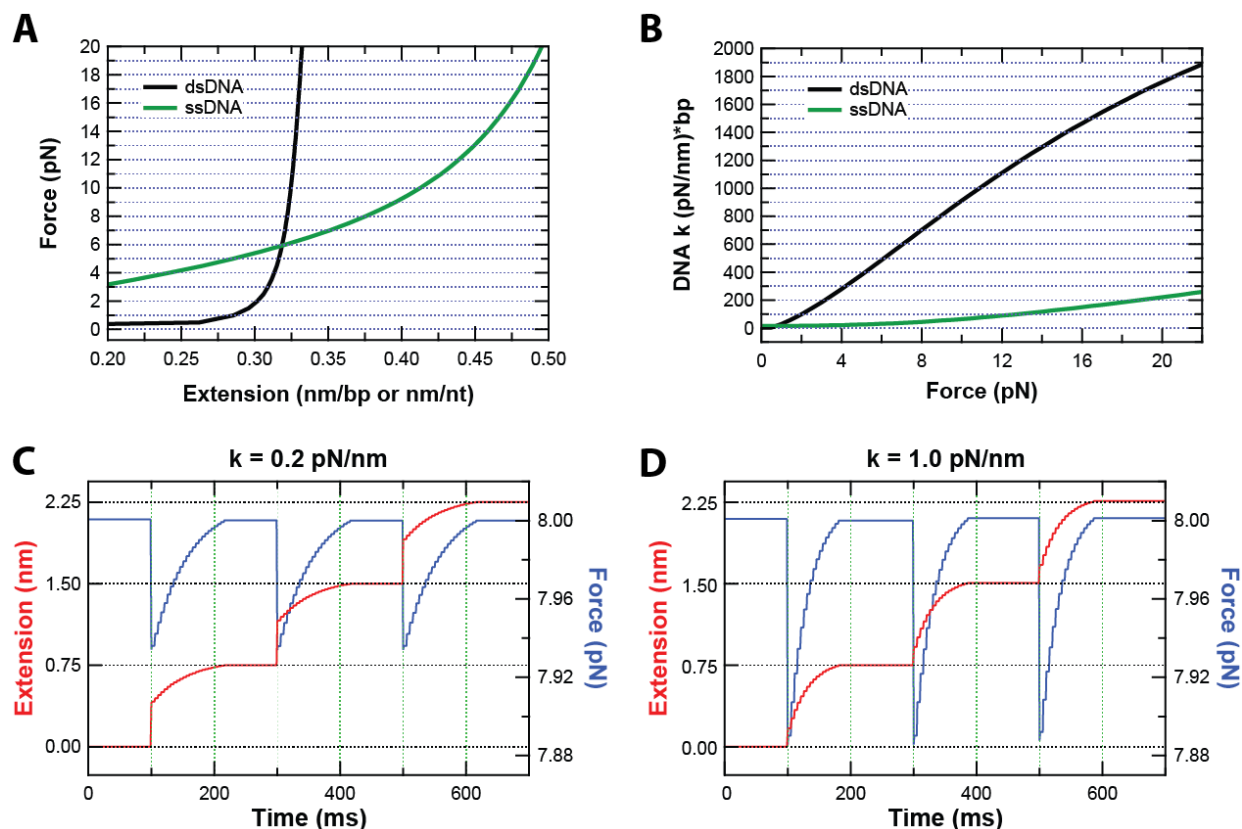


Figure 4.1: DNA mechanistic properties and step simulations.

A) The dsDNA eWLC model and the ssDNA eFJC model, both as functions of extension per monomer unit (bp or nt). B) Nucleic acid polymer stiffness curves as a function of force. Made from the derivatives of the curves in (A). At a given force, the DNA k value must be divided by the number of monomer units in the polymer to get the true stiffness. C) Simulations of RecQ 1-bp stepping on my hairpin substrate held in an 8 pN force clamp with a proportional gain = 1.0. Each step creates an instantaneous, small drop in force that attenuates the extension signal greatly. It also takes the force clamp ~ 100 ms to recover from this drop (with no noise present in the system). This clearly demonstrates the need for a fast force clamp for accurate detection. D) Same as (C), but with 1.0 pN/nm trap stiffness. Higher system stiffness creates larger force drops and attenuation, but faster recovery.

In these simulations, I set a 3000 bp tether with a 39 nt binding site in an 8 pN force clamp with a 250 nm radius bead. The stage position was the control variable, and data was generated by solving the geometric constraint equations (see Figure 2.12) and F - x models. For ease of use, the generated data was assigned a 1000 Hz bandwidth; this is low enough to justify the fact that all thermal equilibration takes place during a single data point, while high enough to sensibly run a simulated active force clamp (at 200 Hz with a proportional gain of 1.0). I then assigned 2 nt of ssDNA to be added to the tether every 200 ms (equivalent to a 1 bp hairpin step). Running this simulation at 0.2 pN/nm and 1.0 pN/nm trap stiffness produces some very interesting results (Figure 4.1C and 4.1D, respectively). In the 0.2 pN/nm case, we see that 1 bp steps reduce the tension from 8.00 pN to 7.94 pN, a 0.75% change. However, that is enough to reduce the initial extension change from the ideal 0.75 nm to 0.40 nm, almost a 50% change! Again, this is due to the ~3000 bp in the handles all shortening just a little, attenuating the overall extension increase from the addition of 2 nt. Moreover, with a gain of 1.0 it takes the force clamp over 100 ms to raise the force back to 8 pN and the signal to 0.75 nm. That is clearly too slow, and would end up smearing together the extension stepping signal in a real assay. Thus the clamp's gain value is clearly an important parameter, which will depend on the force and the noise in the system. Raising the trap stiffness to 1.0 pN/nm keeps the same behavior, except the force drop is higher due to the higher overall system stiffness. This further attenuates the initial signal, but speeds up the force-clamp correction due to the higher ΔF values. Further down, I will discuss the importance of high system stiffness in more detail.

To summarize, the extension signal depends both on the clamped force value and how well the force clamp keeps that value fixed. Force-clamp performance is key, as fluctuations in force distort the extension signal. Thus optimizing the force clamp is another critical task. While

using a full PID (proportional-integral-differential) servo loop may sound tempting, I found that including integral and differential terms just adds noise to the extension signal. The clamp becomes too complex and starts tracking noise or over-compensating for sporadic unwinding. Therefore I only use proportional gain, and have to empirically optimize it for a given assay geometry and set force.

With this, we have exhausted signal optimizations; everything else involves mitigating noise sources, both in extension and force. These noise sources come in two types: thermal bead noise and instrument drift. Thermal bead noise is a fundamental part of trapping experiments, so while it can be mitigated, it can never be completely removed. Instrument drift, on the other hand, is not fundamental and can ideally be eliminated (although real instruments are non-ideal). Instrument drift comes in two main flavors: beam drift (discussed in section 2.1.4) and surface drift (discussed in section 2.1.5). I will first examine thermal bead noise, as its optimization is the underlying reason for multiple design decisions.

The power spectral density of a trapped bead's thermal motion in solution can be mathematically described by a Lorentzian distribution (a type of Cauchy distribution) (37):

$$\sigma_x^2(\Delta f) = \frac{k_B T}{\pi^2 \beta} \int_0^{\Delta f} \frac{df}{f^2 + f_0^2}, \quad (4.1)$$

where $\sigma_x^2(\Delta f)$ is the position variance of the bead as a function of measurement bandwidth Δf , $k_B T$ is the thermal energy of solution, β is the bead's drag coefficient, and f_0 is the corner (or roll-off) frequency of the optical trap. Importantly, integrating from 0 to infinity produces the equipartition relationship $\sigma_x^2 = k_B T / k_{\text{trap}}$, where $k_{\text{trap}} = 2\pi\beta f_0$ is the trap stiffness (see section 2.4.2; the log-log plot of the integrand in Eq. (4.1) can be seen in Figure 2.12C). For a trapped bead tethered by a DNA molecule, the expression gets slightly altered: the stiffness of the DNA is added to the trap stiffness (as they are springs in parallel). DNA stiffness can be computed by

taking the derivative of the F - x curves in Figure 4.1A. The resulting functions (Figure 4.1B) can be used to compute tether stiffness by taking the stiffness at a specific force and dividing it by the number of bp or nt in the substrate. In other words, longer nucleic acid polymers are more flexible, while shorter ones are stiffer.

With the DNA stiffness accounted for, we can compute the noise value we care about: the standard error in the mean bead position. This quantity is the square root of σ_x^2 divided by the number of independent data points averaged together from the bead position data. Roughly, the roll-off frequency of the system (trap + DNA) specifies how quickly these independent data points are collected. The expression for this can be written as (125):

$$\sigma_x^{\text{SEM}} = \frac{\sigma_x}{\sqrt{N}} = \sqrt{\frac{k_B T}{k_T}} \sqrt{\frac{\Delta f}{f_0}} = \sqrt{\frac{k_B T}{k_T} \frac{12\pi^2 \eta r \Delta f}{k_T}} = \pi \sqrt{12k_B T \eta} \frac{\sqrt{r \Delta f}}{k_T}, \quad (4.2)$$

where σ_x^{SEM} is the standard error, $N = f_0/\Delta f$ is the number of independent data points averaged together (Δf is the final bandwidth, which must be lower than f_0), η is the dynamic viscosity of the solution, r is the bead radius, and $k_T = k_{\text{trap}} + k_{\text{DNA}}$ is the total stiffness of the system. Note $\beta = 6\pi\eta r$ for a spherical object in liquid. Also note that k_{DNA} is ~ 0.2 pN/nm for my tether lengths and set force, while k_{trap} gets set to $0.2 - 1.0$ pN/nm. The last expression in Eq. (4.2) has been split into two terms for clarity. The first has constants and temperature-dependent inputs that are not very variable; obviously the constants are fixed, and T and η do not change much over a few Kelvin, the temperature range of my trapping assay. Therefore, this term is roughly constant, and noise reduction efforts must be directed towards the second term.

At first glance, the bead noise seems to: (1) increase with bead size by \sqrt{r} , (2) increase with the measurement bandwidth by $\sqrt{\Delta f}$, and (3) decrease proportional to k_T . Yet that analysis ignores how the parameters interrelate. Recall from section 1.1 that the trap stiffness has a r^3

dependence (for beads with r much smaller than ~ 400 nm, the beam radius) (46). Thus, for a given fixed k_T , larger beads will have higher noise. *But* for a given fixed laser power larger beads produce a much higher k_T , and thus reduce the overall bead noise.

$$\sigma_x^{\text{SEM}} \propto \frac{\sqrt{r}}{k_T} = \frac{\sqrt{r}}{k_{\text{trap}} + k_{\text{DNA}}} \propto \frac{\sqrt{r}}{r^3 + k_{\text{DNA}}}. \quad (4.3)$$

One way to understand this relationship is to note how bead size and trap stiffness affect the correlation time $\tau = \beta/k_T$, the average time interval between independent (i.e., uncorrelated) data points. Increasing the bead's size increases the drag on the bead, which increases the time interval during which its movements are correlated. Increasing the system stiffness decreases that time interval, since a stiffer system corrects the bead's thermal vibrations faster. The best size choice will depend on the exact optical setup, since the r^3 scaling falls off as beads get as large as the beam width. Increasing bead size further increases drag linearly while initially keeping trap stiffness constant, and then eventually *decreases* trap stiffness, as the beads become too large for the trapping laser to properly surround (46).

Given this information, it is clear that beads can be too small or too large for stepping assays. There are other complications: the first is that bead size also affects force noise. To get an expression for that, we can multiply the bead's position noise given in Eq. (4.2) by k_T :

$$\sigma_F^{\text{SEM}} = k_T \sigma_x^{\text{SEM}} = \sqrt{2\pi k_B T \beta \Delta f}. \quad (4.4)$$

From this, it is clear that while the bead's position noise can be reduced by increasing k_T , the force noise cannot. Thus increased bead size only increases the force noise, which makes the force clamp harder to run, which degrades overall signal quality.

The second complication is that optimizing bead size and system stiffness takes place in a 2D geometry. From section 2.4.2, we know that trap stiffness has lateral and axial components,

and that the axial one is typically 2x to 3x weaker than the lateral one. To increase overall stiffness, one must therefore pull the DNA tether at a very shallow angle, so that the contribution of the lateral trap stiffness is maximized (Figure 4.2A). However, this cannot be done with large beads and short DNA tethers, as both will geometrically force the pulling angle to increase. Trying to reduce the pulling angle by decreasing the height h between the bead and surface also comes with a cost: the viscous drag on the bead increases due to the proximity of a fixed surface. This increased drag is quantified by Faxen's law correction factors to the dynamic viscosity η in both directions (Figure 4.2B) (106). Increasing drag at fixed stiffness increases the correlation time $\tau = \beta/k_T$ of the bead's motion (i.e., lowers roll-off frequency via $k_{\text{trap}} = 2\pi\beta f_0$), reducing my ability to average down noise. Thus there is a careful balancing act between choosing the right bead size, height, and tether length to achieve the ideal assay geometry for low noise work.

After iterative testing of bead sizes, heights, and tether lengths, I settled on a bead radius of $r = 250$ nm, a height between surface and bead edge of $h = 200$ nm, and a tether contour length of 1000 nm (3000 bp of dsDNA). I found this combination, which produces an initial pulling angle of $\sim 22^\circ$, to give the best mixture of noise characteristics and usability. In this trapping instrument, beads with 250 nm radii can produce a trap stiffness of 1 pN/nm in the lateral direction when using slightly less than max laser power, sustainable for several seconds before thermal drift starts to dominate. As seen in Figure 4.2B, a 250 nm radius bead at a height of 200 nm above the surface induces a Faxen's law drag correction of $\sim 1.5x$ and $2.5x$ in the lateral and axial directions, respectively.

With tethering geometry optimized, we should further delve into the costs and benefits of increasing trap stiffness via the trapping laser power. This method of increasing k_T is the most controllable, since bead size and material are both fixed properties once the experiment begins;

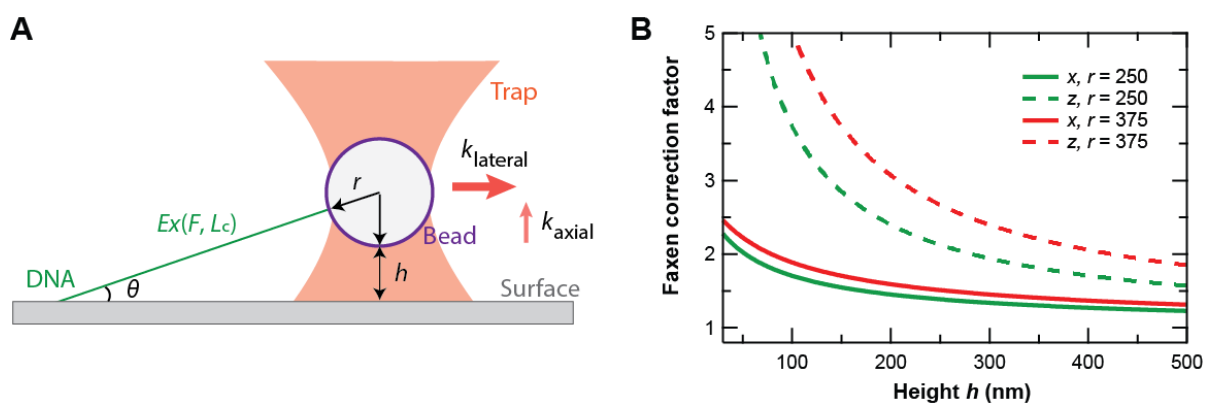


Figure 4.2: Surface-coupled geometry optimization.

A) Cartoon depicting the geometry considerations that must go into designing a surface-coupled assay. The bead radius, height above the surface, and DNA length all affect the pulling angle θ between the DNA and surface. The smaller the angle, the more the stronger lateral trap stiffness contributes to the assay. B) Faxen's law correction factors for the drag coefficient as a function of height above the surface. The corrections factors for motion parallel to the surface (solid lines) are lower than those for motion perpendicular to the surface (dashed lines). In addition, the larger the bead, the larger the correction factors at a fixed height.

laser power, on the other hand, can be rapidly changed thanks to the AOM servo loop (section 2.1.4). Increasing trap stiffness in this manner reduces the bead thermal noise dramatically, as expected (Figure 4.3A), but comes with two costs: intense thermal drift in the instrument and potential biological damage. Recall that the lasers pass through a large objective before entering the sample plane (section 2.1.1). This objective, made up of multiple lenses glued into a single metallic shell, is temperature sensitive. As laser light passes through it, the internal elements absorb heat from the light and the entire piece expands. This thermal expansion distorts the beams' propagation, leading to laser drift in the sample plane. In tethered bead assays, this produces large drift effects in the extension trace (Figure 4.3B). Second, in addition to signal degradation, more intense laser light can also harm biological molecules. 1064 nm light can interact with polystyrene and molecular oxygen to produce reactive oxygen species, which induce damage in both DNA and its linker chemistries (107). Oxygen scavenging systems can mitigate this damage (e.g., PCA-PCD, glucose oxidase, DTT), but higher laser light will inevitably lead to higher rates of damage. Finally, higher laser light also heats the water near the optical trap up a few Kelvin. However, as specified above, this temperature change is typically not enough to impact the S/N in a meaningful way.

By increasing the trap stiffness so dramatically, we soon run into a new noise floor. In other words, we are able to reduce the bead thermal noise to such an extent that it is no longer dominant. The subsequent dominant noise is, unsurprisingly, relative drift between the surface and lasers. Even with active stabilization on both, small jerks around their mean positions can still get through into the signal (Figure 4.3C). Given optimized servo loops, this noise cannot be further reduced and sets the instrument's noise floor. And unfortunately, this noise can be on the scale of the expected stepping signals. This means that not only is the time at high stiffness

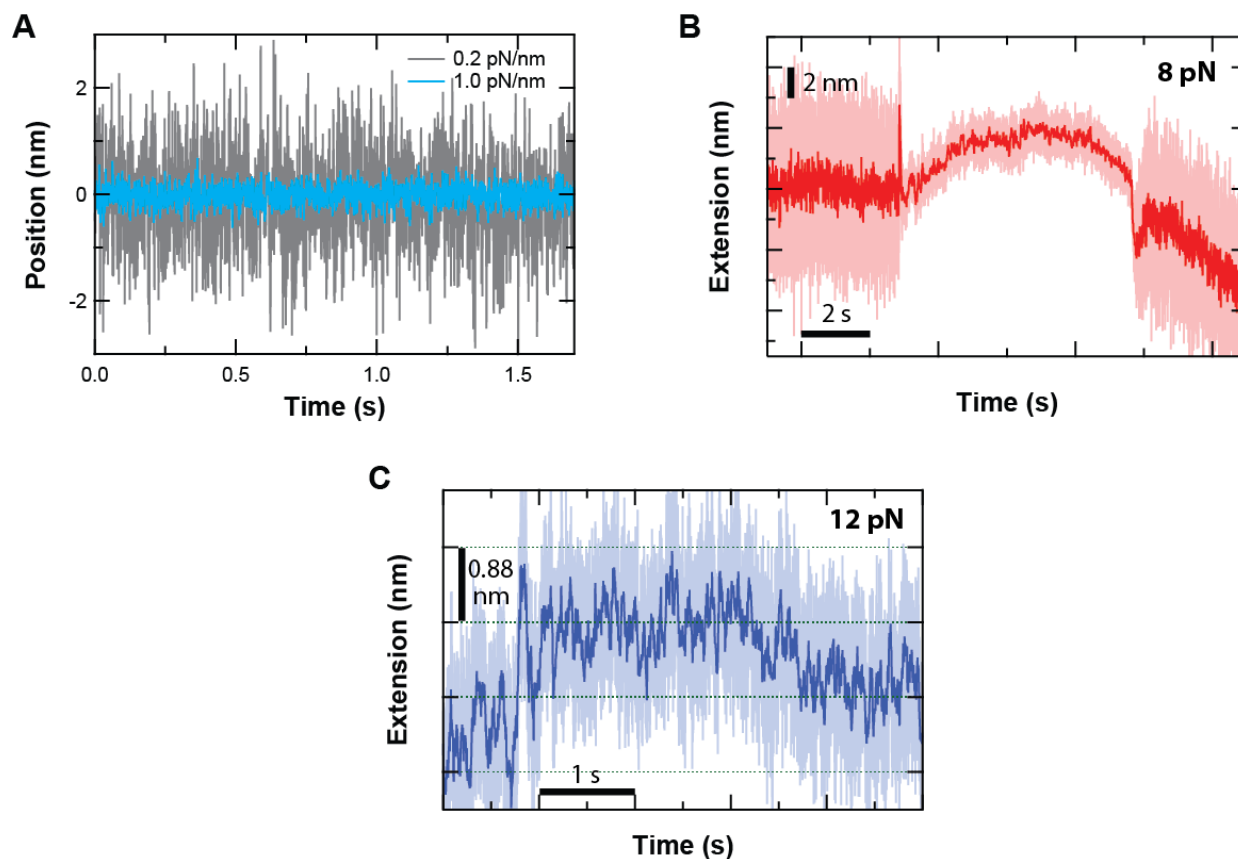


Figure 4.3: Optimizing the trap stiffness.

A) The thermal noise in bead position can be significantly reduced by increasing the stiffness of the optical trap. Shown is 1200 Hz position data for a trapped $r = 250$ nm bead with either 0.2 pN/nm (grey) or 1.0 pN/nm (cyan) trap stiffness. The standard errors in the mean of these data sets are 0.9 nm and 0.2 nm, respectively, giving an overall noise reduction of 4.5x, close to the expected value of 5 for a 5-fold stiffness change (see Eq. 4.3). B) Going from low to high trap stiffness by changing the laser power in the sample plane induces thermal drift. Shown is the extension data for an activated hairpin tether at 3 kHz (light) and 300 Hz (dark) at 8 pN. The characteristic thermal drift for this process is a slight increase in extension, followed by a flat period of little-to-no drift, followed by a rapid decrease in extension. This decrease will continue as long as the high trap stiffness is maintained, and will even continue briefly after the laser power is decreased. These different types of drift are assumedly due to different parts of the microscope objective thermally expanding at different rates. Data is ideally collected in the flat region with no drift for maximum precision. C) Reducing the thermal noise via high trap stiffness reveals the instrument noise floor. An activated hairpin tether held at 12 pN and 1.0 pN/nm will display instrument drift on the order of the desired stepping signals. This is the major limitation of the assay (light: 3 kHz; dark: 300 Hz).

limited by thermal drift, we will also need multiple unwinding steps in a row in order to clearly delineate between real steps and the noise floor. These demands on the experiment, combined with others detailed further below, will clearly reduce the throughput of useful data.

With the trap stiffness sorted, let us return to the clamped force value. As discussed above, the benefits of high tension are an increased signal (to due higher ssDNA extensions) and slightly reduced noise (due to slightly stiffer dsDNA handles). Yet there is a cost to higher force: faster helicase unwinding speeds, since putting more tension across the dsDNA hairpin reduces the energy needed to unwind it. Recall that resolving 1-bp steps through thermal noise involves averaging down high bandwidth data to achieve better spatial precision at the cost of time resolution. Ideally this averaging should only be done *in between* instances of helicase stepping. If multiple steps get averaged into a single data point, obviously that stepping information is lost and all we get is a smear of increasing extension. Thus, the speed at which the helicase unwinds sets a limit on the amount of data averaging, and thus the amount of noise reduction, actually achievable. That said, the effect force has on unwinding speed is enzyme-specific, and RecQ's speed has been shown to be nearly independent of force (making it a very "active" helicase) (122). This is at once a blessing and a curse: we can use high force to amplify the signal without affecting the speed, but we cannot use low force to significantly slow down the helicase and thereby increase our noise averaging capacity. After many tests, I found that 8-12 pN worked well, and that there is few observable difference between values in this range. Since earlier magnetic tweezer assays on RecQ used 8 pN, that was my most commonly set force. However, my later stepping work used 10 and 12 pN more frequently for slight increases to S/N.

As a final note, another way to potentially reduce RecQ unwinding speed is to lower the solution temperature. Many enzymes have temperature-dependent activity, if thermal forces are

critical for certain binding events, conformational changes, or oligomeric formations (recall the importance of temperature in the oligomeric debate for RecQ in section 1.3). Unfortunately, the few studies performed on the temperature dependence of RecQ's unwinding activity have found little change within my viable temperature range (85, 101). Given this, I did not pursue temperature variation as a way to slow down RecQ.

4.1.3 Optimizing biochemical conditions

While we have exhausted optical trapping optimizations, there is still one major way to improve the signal-to-noise ratio (S/N): slowing down unwinding speed. As stated above, the helicase unwinding speed sets an upper bound on how much spatial averaging can be done before signals get averaged together into a smear. Therefore, slow enzyme stepping is *highly* desirable, and since RecQ requires ATP for its activity, the obvious way to reduce its speed is to reduce the concentration of ATP in solution. By limiting [ATP], we make ATP binding rate-limiting in the catalytic cycle, and then adjust that rate by adjusting [ATP]. This is a very common tactic in stepping assays (26, 32), but in RecQ's case there is a steep cost: RecQ's off-rate from DNA, the rate at which it unbinds and dissociates from the substrate, is also ATP-dependent (126). Higher [ATP] means RecQ is able to unwind more processively, staying on a single substrate for longer, while lower [ATP] means it dissociates sooner, sometimes right after it binds. This introduces a difficult balancing act into signal resolution: on the one hand, we need the slow, well-resolved steps that come from low [ATP]; on the other hand, we need enough consecutive steps to properly active high trap stiffness for increased S/N and to discern the true step size of RecQ.

Since RecQ rapidly unwinds at saturating [ATP] (1 mM), finding an [ATP] value where RecQ stepping can be resolved is a critical first step (Figure 4.4). As reported in section 3.4,

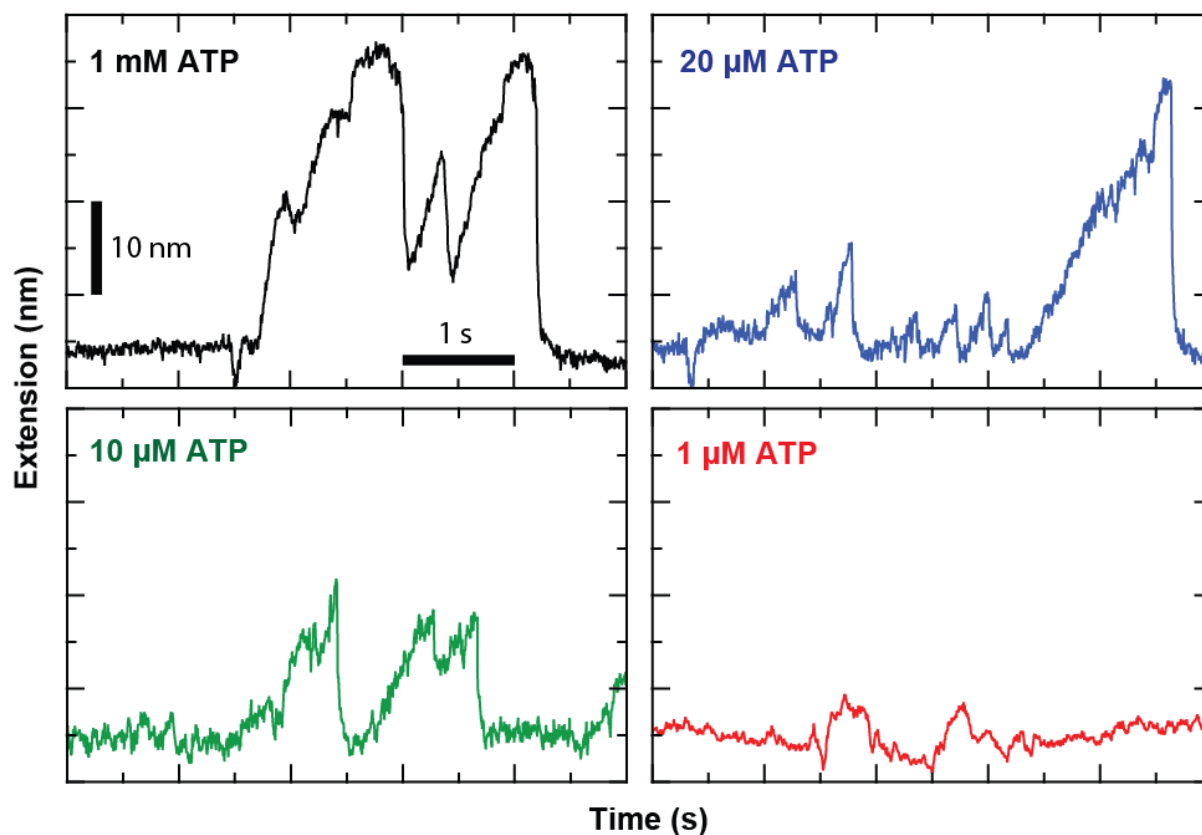


Figure 4.4: RecQ processivity varies with [ATP].

Four traces of RecQ unwinding at 200 Hz bandwidth and 8 pN tension. The processivity of the helicase lowers as [ATP] is lowered. The 1 μM ATP trace was collected at 1.0 pN/nm trap stiffness for maximum precision, as opposed to the 0.2 pN/nm trap stiffness used in the other three traces.

RecQ unwinds 50% GC DNA at an average speed of ~60 bp/s (45 nm/s) for 1 mM ATP and 8 pN of force. That gives a mean stepping frequency of one step per 16 ms, with most of the steps occurring much faster (for an exponential distribution of stepping times). Since my active force clamp runs once every 5-10 ms (depending on the exact assay), the clamp will not keep up and so will lose the steps in smear and noise. To slow down stepping, [ATP] must be reduced to near or below its Michaelis-Menton constant for RecQ (the concentration at which RecQ's ATP hydrolysis rate is half the saturating rate). Previous work found this value to be $K_M = 16 \mu\text{M}$ (101). Using 20 μM , 10 μM , and 1 μM [ATP] definitely slows mean RecQ unwinding, but also shows the steep cost: processivity is lost and the steps are slowed down non-uniformly (Figure 4.4). Even at low [ATP], there are often unwinding runs that have largely the same speed as saturating ATP. Much of the slowdown arises from the decreased processivity, which introduces not only the expected pausing but also apparent slippage into the traces. So while lowering [ATP] is helpful overall, the clear downsides provide motivation to try alternative methods for slowing down RecQ.

Lower [ATP] slows RecQ unwinding because it extends the ATP binding step of the hydrolysis cycle (Figure 4.5A). However, that is not the only way to extend the binding step. Another tactic for slowing down ATPases is to replace some portion of the ATP with non-hydrolysable analogs, which extend the ATP binding step by temporarily clogging the hydrolysis pocket, forcing usable ATP molecules to wait until it becomes unclogged. This trick has the benefit of keeping the ATPase in a conformation close to its ATP-bound state, extending the time spent in that conformation instead of the ATP-unbound one. This is desirable for RecQ, since it has higher affinity for DNA in its ATP-bound states (126). If I could slow down the hydrolysis cycle by using an analog while keeping the unwinding processivity high, I could

better resolve RecQ's overall stepping. Thus I spent time trying out different non-hydrolysable ATP analogs to see if one of them could dramatically improve the assay.

However, adding in direct competitors to ATP is not automatically an improvement: if certain criteria are not met, these analogs will just make the assay worse. For instance, to resolve single steps, the analogs must on average interrupt the ATP hydrolysis cycle at least once per cycle. It does no good if only one out of every dozen steps is delayed, as sequential 1 bp steps will likely never be seen. The ideal analog should have a RecQ on-rate comparable to or higher than ATP and a RecQ off-rate slower than the hydrolysis and product dissociation rate of ATP. This would enable the analog to out-compete ATP to RecQ and stall the enzyme, creating the desired slowdown. Sadly, the binding affinity for any analog is likely to be lower than ATP's affinity (since ATP is the binding pocket's sole target substrate), but increasing the relative concentration of analog to ATP can compensate for this. The bigger sticking point is the off-rate: we want an off-rate that is slow but not *too* slow. For example, if the off-rate is so slow that a single step takes a minute, instrument drift can potentially obscure the steps, even with active surface stabilization. Ideally, we would like an analog to slow the hydrolysis cycle down 2-fold to 10-fold. With these criteria in mind, I tested a variety of non-hydrolysable ATP analogs.

The analog I used first, and the most common non-hydrolysable ATP analog, is called ATP γ S. This molecule has the same structure as ATP except for one atom: the γ -phosphate's double-bonded oxygen is replaced with sulfur. This single swap renders it practically non-hydrolysable by many ATPases, including RecQ (74, 91). After running multiple unwinding assays with [ATP] and [ATP γ S] values ranging from 0 to 1 mM, I was able to confirm several points about the interaction dynamics of RecQ, ATP, and ATP γ S in solution. First, ATP γ S has a slower on-rate and off-rate than ATP, as expected. For the on-rate, using an ATP:ATP γ S ratio of

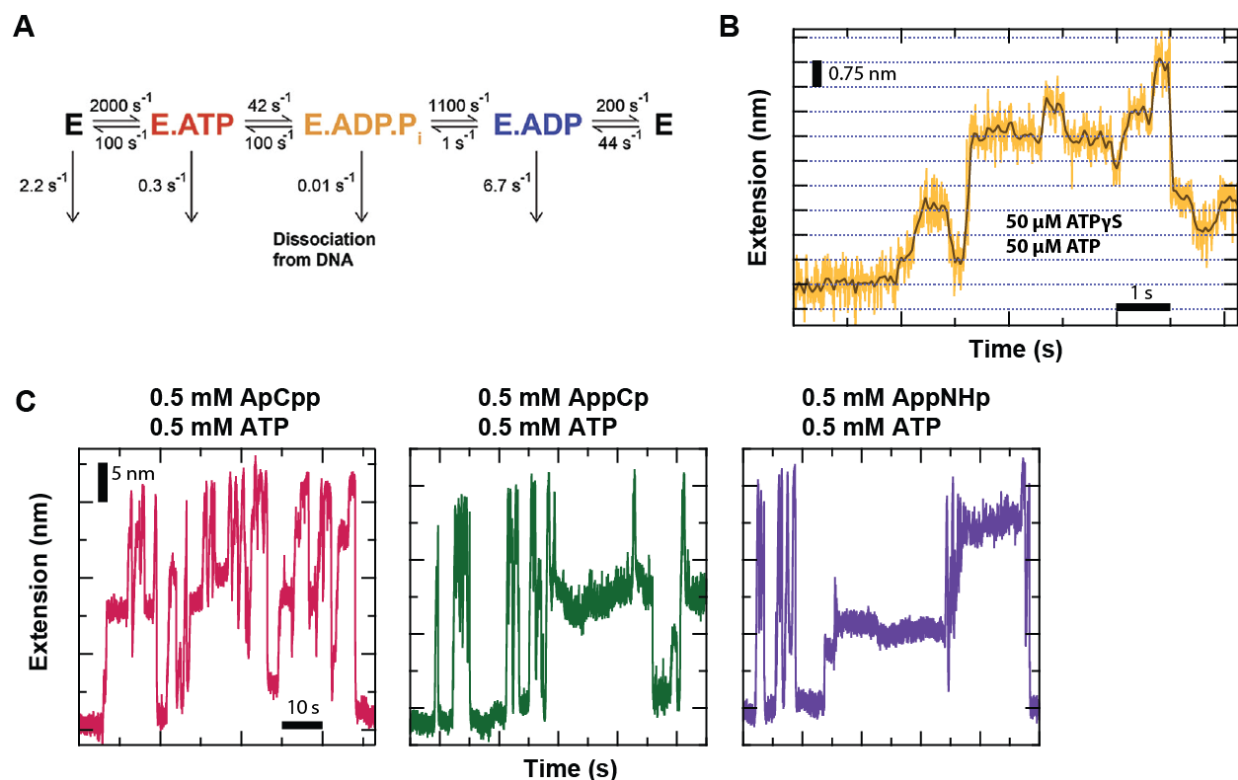


Figure 4.5: RecQ interacts with non-hydrolyzable ATP analogs.

A) A diagram for the typical kinetic pathway of RecQ's hydrolysis of ATP with approximate rate constants. The rate constants are specified as either best-fits or limiting values (lower bounds for k_1 , k_2 , k_3 , and k_4 ; upper bound for k_3 . Associative rates given for pseudo-first-order conditions). Figure reproduced from Sarlos et al., 2015 under the Creative Commons license. B) RecQ unwinding trace with 50 μM ATP and 50 μM ATP γS . Data taken at 0.2 pN/nm trap stiffness in 50 mM NaCl and 1 mM MgCl₂. Light: 100 Hz, dark: 10 Hz. The pauses in this trace were noticeably more uniformly distributed than other traces taken in these conditions. From this, 1-bp forward and backward steps can be clearly seen, in addition to larger extension increases. It is impossible to tell whether these larger increases are due to single multi-bp steps or the smearing together of multiple 1-bp steps. C) Example traces of RecQ unwinding in the presence of 0.5 mM ATP and 0.5 mM ApCp (left), 0.5 mM AppCp (middle), or 0.5 mM AppNHp (right). Very infrequent, very long pauses can be observed in all three traces. Compared to ATP γS , these non-hydrolyzable ATP analogs are therefore not as suited for aiding 1-bp stepping assays.

1:1 does not provide enough reliable slowdown, while using a ratio of 1:5 completely stops all unwinding activity. All available data indicate that ATP γ S keeps RecQ bound to DNA while it is associated with RecQ. For the off-rate, ATP γ S seems to have a wide range of dissociation times whose average is on the order of ~ 1 s. The best results from these mixed assays occur when ATP is kept low, in the 10-50 μ M range, to keep the overall RecQ speed low. I collected some bp-scale stepping results with these conditions (Figure 4.5B), but overall the ATP γ S-induced slowdown still had many multi-bp steps and smeared unwinding runs. To see if I could obtain better-resolved unwinding, I tested several other non-hydrolysable ATP analogs to check whether their kinetic rates were more in line with ATP.

The next analogs I used had additional atoms in their structures, in between the phosphate groups. If we denote ATP by Appp, where A is the nucleoside and the p's are the phosphate groups, then these analogs were ApCpp, AppCp, and AppNHp, where the C's are carbon insertions and the NH is a nitrogen insertion. To test whether their kinetic rates were closer to ATP's than ATP γ S, I ran RecQ unwinding assays with equal parts ATP and analog, using 0.5 M for both to ensure that no pausing would arise from low [ATP]. The results of these tests showed that all three analogs had *much* lower on- and off-rates compared to ATP γ S (Figure 4.5C). Thus, they were not viable replacements. At this point, it seemed that while doping the solution with non-hydrolysable analogs was helpful, it would never provide the kind of uniform slowdown I needed to ensure that all extension changes could be unambiguously designated as single signals. With that determined, I then worked to see whether other steps of the hydrolysis cycle could be extended, such as the actual hydrolysis step or product dissociation step.

To slow down the hydrolysis step, one would need to either mutate the RecQ or change a component in the hydrolysis reaction. These components include the triphosphate fuel source

(usually ATP), the divalent cation that bridges the phosphate-protein interactions (usually Mg^{2+}), or the salt and pH of the external environment (usually ~ 100 mM NaCl at pH 7.5). The overall goal is to slightly distort the geometry of the RecQ hydrolysis reaction to make it less efficient, and thus slow it down. I initially tested environment changes, as they are easiest to implement; they did nothing. Varying monovalent salt from 25 mM to 150 mM did not affect unwinding speed in any measureable way. For the pH, prior bulk studies showed RecQ's binding affinity for ssDNA drops 2-fold at pH 5.5 and 8.5 (from a maximum at pH 6.0-7.5) (86). However, I have never found a bulk measurement for how RecQ's speed changes with pH. In my single-molecule experiments, I did not observe any speed difference at pH 8.5, and was unable to measure RecQ unwinding at pH 5.5 due to my beads adhering to the surface. From this, I determined that varying environmental conditions was not a fruitful path for slowing RecQ unwinding.

Another way to slow down the hydrolysis step is to replace ATP with a hydrolysable analog. This allows the reaction to take place, but at a reduced rate since the analog does not fit perfectly into the binding pocket. While investigating chemicals listed as non-hydrolysable ATP analogs, I found that RecQ could actually hydrolyze one: ATP α S, the α -phosphate equivalent of ATP γ S. My initial experiments showed that RecQ unwinds ~ 2 -fold slower with ATP α S vs. ATP (at 50 μ M), but that most of the slowing is due to processivity loss and slippage, similar to the speed decreases from lower [ATP]. ATP α S possesses two optical isomers, S_p-ATP α S and R_p-ATP α S, and previous research found that multiple enzymes hydrolyze the S_p isomer while the R_p isomer is rarely hydrolysable (this trend held for dATP α S versions, as well) (127-129). The first batch of ATP α S I tested was a 1:1 mixture of the two isomers, so it was unclear how RecQ precisely interacted with each. To clear this up, we tested a pure stock of R_p-ATP α S, since prior work implicated it as the less hydrolysable of the two (127-129).

Running a RecQ assay with 20 μM ATP and either 0 or 100 μM $\text{R}_p\text{-ATP}\alpha\text{S}$ showed a clear processivity loss for all of the 100 μM traces; most could not even clear half of the hairpin before dissociating (Figure 4.6A). This shows that the analog and helicase frequently interacted, which is already better than some prior analogs (Figure 4.5C). Compared to the unwinding seen with the 1:1 $\text{ATP}\alpha\text{S}$ mixture, this mixture has slower and less processive activity even with a much higher overall concentration. Thus we can deduce that the S_p isomer in the 1:1 mixture is the major component used in unwinding, and that RecQ interacts with $\text{S}_p\text{-ATP}\alpha\text{S}$ similar to ATP, akin to enzymes in past literature (127-129). We can therefore ignore the mixture and just use ATP and $\text{R}_p\text{-ATP}\alpha\text{S}$, or $\text{R}_p\text{-ATP}\alpha\text{S}$ alone (control experiments showed that RecQ can hydrolyze $\text{R}_p\text{-ATP}\alpha\text{S}$, although very poorly).

As a note, I found that environmental conditions affect $\text{ATP}\alpha\text{S}$ hydrolysis differently than ATP hydrolysis. For ATP, RecQ unwinding was unchanged by monovalent salt variations; this was not true for the 1:1 mixture of $\text{ATP}\alpha\text{S}$. Specifically, very little processive RecQ unwinding was observed when using 150 mM NaCl (as opposed to the standard 50 mM), even with 1 mM 1:1 $\text{ATP}\alpha\text{S}$. However, I found that the unwinding runs present at these conditions had the same local speed as those at lower [NaCl], implying that the off-rate of the RecQ· $\text{ATP}\alpha\text{S}$ complex from its DNA substrate is salt dependent, but that the binding and hydrolysis rates remain unaffected. Sadly, that means this salt dependence cannot be used to slow RecQ.

For completeness, I also decided to check whether the ATP in RecQ assays could be replaced by other NTPs, specifically GTP and UTP. One of the first papers on RecQ tested the hydrolysis activity of RecQ with GTP, and did not find any within the noise threshold (70). However, because our lab had some GTP lying around, I double-checked it on the off-chance of there being some very slow activity that could benefit my S/N. But as expected, there was no

unwinding activity at 1 mM GTP. The UTP was much the same story, except the idea for it came from finding out that RecA can hydrolyze UTP poorly (130). Since RecQ's hydrolysis pocket is made up of two RecA-like domains, I chose to try it, as well. No activity was detected.

With the exception of mutation, there is only one more way to disrupt the hydrolysis reaction: swap the Mg^{2+} that coordinate the ATP with different divalent cations. Investigating how divalent-coordinated enzyme reactions change with divalent type is a standard procedure, and was one of the first biochemical analyses performed on RecQ (70). In that work, the authors found RecQ's hydrolysis of ATP was most efficient with Mg^{2+} , as expected. Swapping the Mg^{2+} for Mn^{2+} , Ca^{2+} , and Zn^{2+} reduced the hydrolysis efficiency to 96%, 89%, and 24% of the Mg^{2+} value, respectively. These findings tell us that in the RecQ binding pocket Mg^{2+} and Mn^{2+} act interchangeably, with Ca^{2+} acting very similar. Zn^{2+} was the only ion exchange that significantly reduced ATP hydrolysis efficiency, though the bulk assay could not say exactly how. Divalent swapping is especially popular for polymerase studies, since the kinetic changes induced by the swaps can be mapped to questions of direct biological interest, such as how metal contaminants cause mutations during replication (131). The cited review shows that these studies use a large collection of divalent cations with multiple polymerases, and that they found some clear trends in how the enzymes behaved with certain cations. I used this data and the work done previously on RecQ to inform my choices for further divalent swapping.

In RecQ and the studied polymerases, swapping Mg^{2+} for Mn^{2+} did not change any kinetic parameters, so I did not bother testing it. Since Ca^{2+} was in my lab already, I tried it as my first swap to see what a 10% drop in bulk hydrolysis efficiency looks like in a single-molecule assay. As expected, unwinding looked mostly the same, with the addition a few more pauses (Figure 4.6B). I next tried to repeat the same experiment with $ZnCl_2$, but ran into the

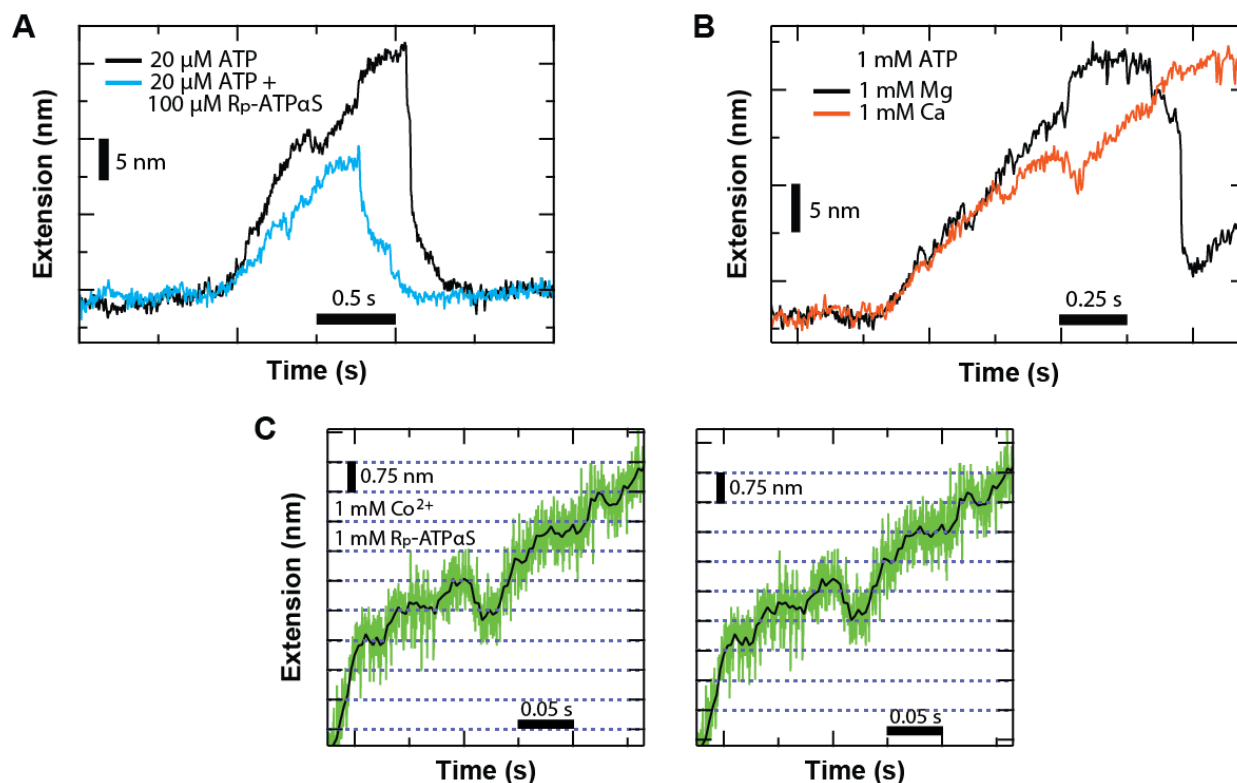


Figure 4.6: Slowing RecQ unwinding with ATP α S and divalent swaps.

A) RecQ unwinding traces with 20 μM ATP (black) and 20 μM ATP + 100 μM $R_P\text{-ATP}\alpha\text{S}$ (blue). 300 Hz traces taken at 0.2 pN/nm trap stiffness with 75 mM NaCl and 1 mM MgCl_2 . The most striking effect of adding $R_P\text{-ATP}\alpha\text{S}$ is the processivity loss in all RecQ unwinding events. The consistency of this loss implies that RecQ and $R_P\text{-ATP}\alpha\text{S}$ repeatedly interact during the unwinding traces. B) Comparison of RecQ unwinding at 1 mM ATP with either 1 mM Mg (black) or 1 mM Ca (orange) as the divalent cation. Other conditions similar to those in (A). As expected from prior bulk ATP hydrolysis assays, RecQ can processively unwind DNA when only Ca divalent cations are available. The only noticeable change in these single-molecule traces was a slight increase in the number of pauses during unwinding. C) 1-bp steps resolved in the presence of 1 mM Co divalent cations and 1 mM $R_P\text{-ATP}\alpha\text{S}$. Light traces: 3000 Hz, dark traces: 300 Hz. Data was taken at 1 pN/nm trap stiffness without DTT in solution, as side-reactions occur when it and Co are placed in Tris-HCl, NaCl solution. Left: At least 3 bp worth of unwinding occurs in a smear, followed by two well-resolved 1-bp steps forward and one 1-bp step backwards. Right: Drift occurs that puts the unwinding trace slightly out of register with prior steps. However, four 1-bp steps forward can clearly be seen to occur after the backwards step. Unfortunately, after this unwinding becomes a smear again.

problem of zinc oxychlorides precipitating out of solution and causing my bead-DNA tether complexes to adsorb to the surface (132). Replacing the zinc chloride with zinc acetate fixed this problem, only to show that while RecQ's unwinding speed certainly drops when using Zn^{2+} , its on-rate absolutely plummets. Acquiring just a few unwinding traces was a very time-consuming task, and RecQ repeatedly slipped off of the DNA substrate, indicating that it was not well-bound. Since this may indicate Zn^{2+} is distorting the unwinding process too much (and thus not providing biologically relevant information), I decided to try a few other divalents. First I tried Sr^{2+} , the next after Ca^{2+} in the alkaline earth metal column of the periodic table, but like in all previous polymerase assays (131), it appears that RecQ too cannot use Sr^{2+} at all. This is due to steric hindrance in some respect: either the ion cannot fit inside the binding pocket, or it is simply too large to correctly coordinate ATP for the hydrolysis reaction (133).

The next transition metal divalent I tried, Co^{2+} , did work well. RecQ's on-rate to DNA with Co^{2+} was similar to its on-rate with Mg^{2+} , and it processively unwound DNA while simultaneously experiencing a ~2-fold unwinding slowdown. Because of its ease-of-use and effective properties, Co^{2+} became my divalent of choice when not using Mg^{2+} . As a note, I found that mixing DTT, $CoCl_2$, and buffered solution with Tween-20 did not work well; a sickly brown solution would form (DTT and $CoCl_2$ mixed by themselves is fine). Since using a buffered solution with Tween-20 is necessary when using polystyrene beads (or else they get stuck to the glass surface), I leave out DTT in all Co^{2+} -based assays. To make sure this did not affect RecQ's activity in any significant way, I tested a side-by-side comparison of Mg^{2+} -based RecQ unwinding with and without DTT. There was no difference between the assays, meaning that DTT acts solely as an oxygen scavenger in RecQ unwinding experiments (meaning its removal will lead to more rapid DNA damage, but switching to new substrates can compensate for this).

When combining Co^{2+} with ATP unwinding did not produce as much slowdown as I was hoping, I decided to try it with 1 mM $\text{R}_p\text{-ATP}\alpha\text{S}$, to see whether or not RecQ could hydrolyze the molecule. Unwinding did occur, though with much lower processivity than with ATP (as expected from the results of the prior ATP + $\text{R}_p\text{-ATP}\alpha\text{S}$ assay). With these conditions, I was able to collect some bp-scale stepping runs, but again, with less processivity than I would like and with most of the potential “steps” smeared together by fast unwinding (Figure 4.6C). With this, I concluded the biochemical optimization process without a clear answer to a single, optimum condition set. No conditions tested gave an unequivocally superior unwinding assay compared to all others; it was largely a give-and-take between speed, processivity, activity frequency, ease-of-use, and binding strength. I therefore decided to summarize what RecQ stepping conclusions I could obtain from these various condition sets.

4.1.4 Final RecQ stepping results

With all of this work done, what results did I obtain with my stepping assays? Unfortunately, I never achieved sufficient resolution to unambiguously determine whether the few multi-bp steps I observed were real or simply due to a few fast 1-bp steps being smeared together. This means that I cannot *definitively* comment on whether RecQ only takes 1 bp unwinding steps or whether it can take multi-bp steps. With that said, the RecQ stepping data I did collect can be compared to and contrasted with prior results, starting with the results of the 20 Hz FRET-under-tension assay (92) that observed a wide distribution of RecQ step sizes.

In my clear stepping data, I primarily observed only 1-bp steps (Figure 4.7A). This data mostly came from low [ATP], Mg^{2+} -based traces, but also included a few traces from other conditions (Co^{2+} , $\text{R}_p\text{-ATP}\alpha\text{S}$, ATP+ATP γ S). I typically resolved runs lasting two to four steps;

not enough for useful stepping statistics, but still plainly different from prior work (91, 92). On that point, a number of 1-bp back steps were also resolvable (Figure 4.7B), which have never been clearly shown for RecQ before and will be discussed further below. I was able to collect these traces at forces from 8 – 12 pN and at [ATP] values from 1 μ M to 1 mM, with clear steps more common at lower [ATP] but still present at higher [ATP], especially when using RecQ^{WT} instead of RecQ ^{Δ H} (the final HRDC domain is expected to alter stepping kinetics, but not the physical step size). In fact, a large disparity in the speed of short stepping bursts exists (Figure 4.7C). To quantitatively analyze my stepping data, I took 50 clear stepping runs and used a step-finding algorithm to determine step sizes. This algorithm was previously validated and published by my collaborators Keir Neuman and Yeonee Seol, and uses a t-test to determine significant differences in extension data noise (101). My criteria for selecting “clear” stepping traces is based on the visible presence of at least three extension dwells at regular intervals (for at least two steps in a row), with no regard to the actual interval lengths. Thus no selection bias for a specific step size was placed upon the data. With that, the step-finding algorithm found a total of 245 steps in the 50 traces. I then converted the calculated extension values into base pairs (based on the applied force) and plotted the distribution (Figure 4.8A).

This distribution has a clear peak at 1 bp for forward steps, and a second peak at -1 bp for back steps. Other forward step sizes are present (notably at 0.5 bp), but the 1 bp size dominates the distribution. This is in stark contrast to the previously published RecQ step size distribution from the FRET-under-tension assay (Figure 4.8B). Here the authors, like me, only collected clear traces with a few steps per trace, but instead of using a trap they used a FRET assay paired with a ~6 pN intrinsically taut DNA substrate. The authors observed RecQ taking steps at 20 Hz with sizes ranging from 0.5 bp to 3.5 bp. Importantly, only ~15% of their recorded steps were 1 bp

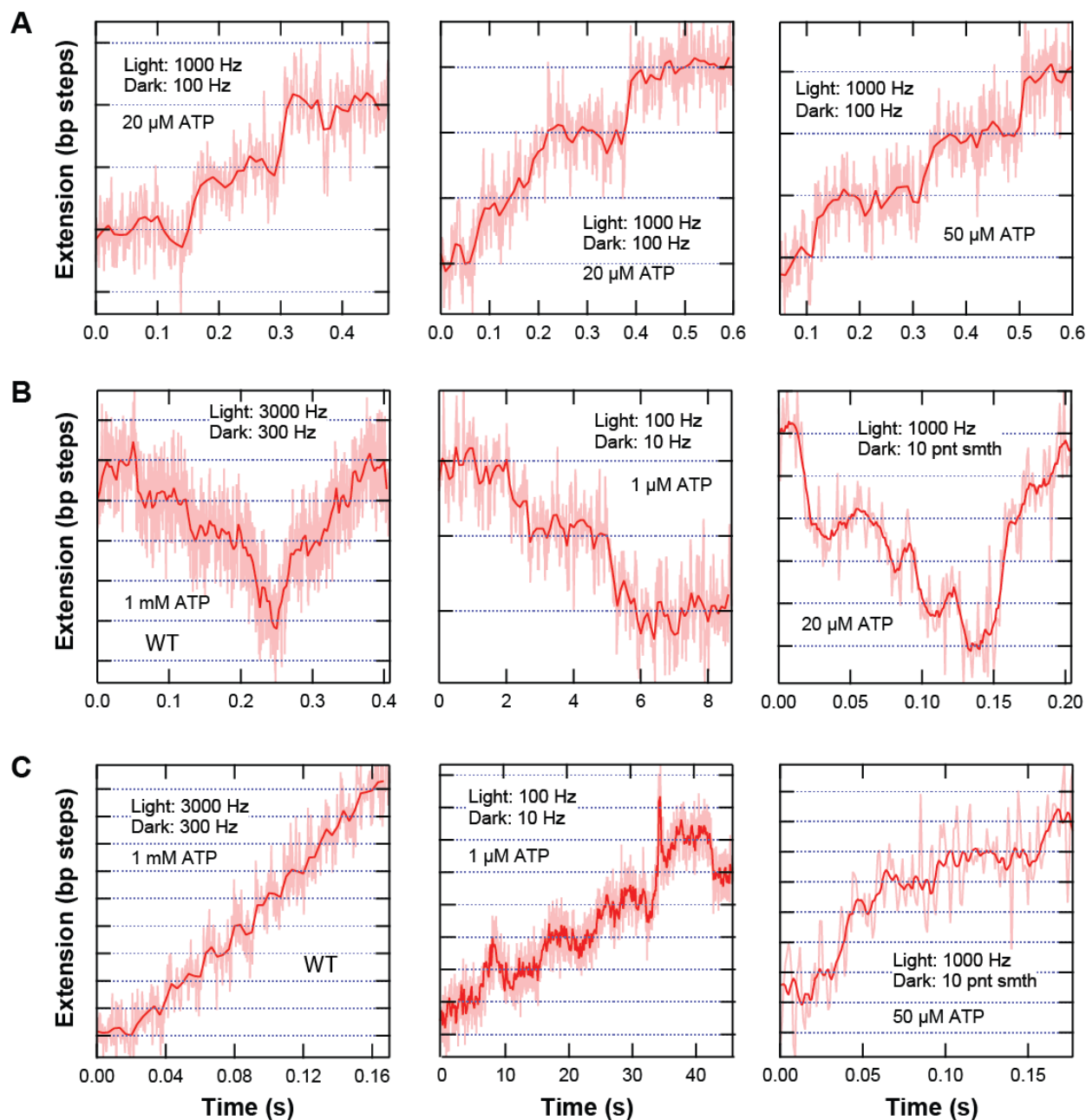


Figure 4.7: The *E. coli* RecQ helicase takes 1-bp physical unwinding steps.

All data collected using Mg^{2+} , ATP, and 8 pN (for 0.75 nm Δx per 1 bp step). A) RecQ data was analyzed by eye for sequential, identifiable dwells (steps), with no criteria placed on spacing. Almost all detected steps had 1-bp spacing. Most runs were limited to 2-3 steps due to noise or smearing from rapid steps. B) 1-bp backsteps were regularly seen. Their speed was comparable to forward steps in each assay, and occurred in RecQ^{WT} (left) and RecQ ^{ΔH} (middle & right). C) Longer 1-bp runs at different time scales. Left: RecQ^{WT} sometimes produced good runs, but was overall harder to work with. Middle: An exceptionally slow stepping trace. This plot and the one above, taken on the same day, were the only time such slow steps could be collected. Right: A fast, resolved stepping trace. The apparent 2-bp step is likely two very fast 1-bp steps.

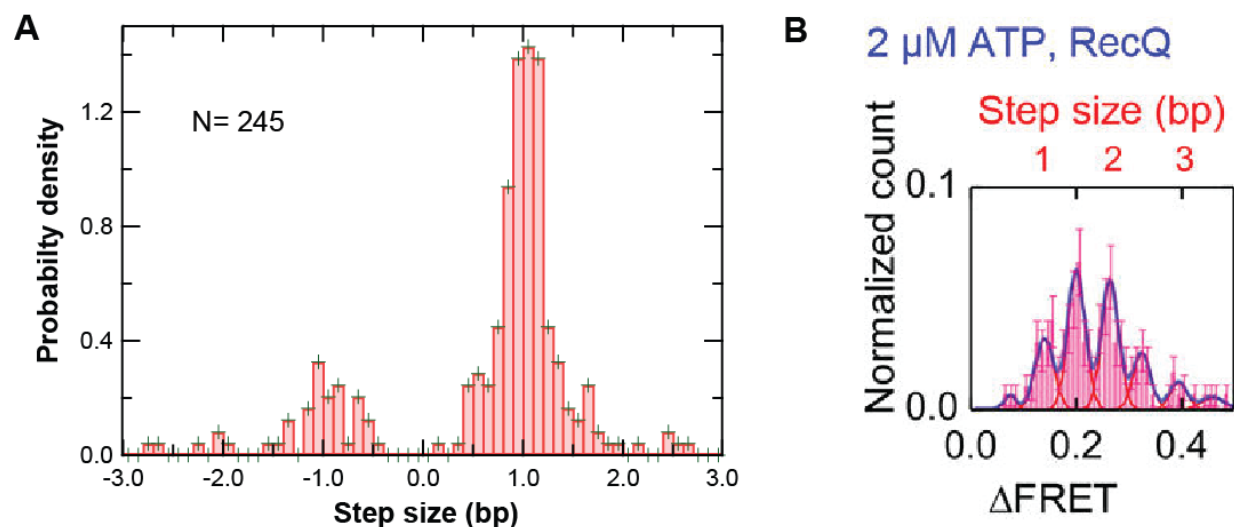


Figure 4.8: The high-resolution step size distribution strongly peaks at 1 bp.

A) A RecQ step size histogram collected using a t-test-based step-finding algorithm on my high-resolution unwinding traces in my optical trap. A total of 245 steps were detected from 50 distinct unwinding runs. Data traces used in this distribution were collected at forces between 8-12 pN and [ATP] between 1 μ M to 1 mM, then converted from extension into base pairs. The underlying distributions for these conditions were all similar to the total distribution, showing that the fundamental physical step size does not depend on force or [ATP]. B) The equivalent RecQ stepping distribution from the FRET-under-tension assay. Data was collected on a \sim 6 pN tensioned DNA substrate at 2 μ M [ATP] and 20 Hz bandwidth. Figure reproduced from Ma et al., 2018 with permission from the American Chemical Society.

(relative to the normalized counts of the rest of the distribution). In contrast, over 50% of their steps were either 1.5 bp or 2 bp (from a data set of 249 unwinding runs), with both individual peaks being larger than the 1-bp peak. If this step size distribution was correct, I should have seen it reproduced in my assay. But I did not. Instead, I found that ~80% of my forward steps were clearly 1 bp, with the majority of the rest being either 1 bp steps broadened by noise or apparent combinations of 0.5 bp and 1.5 bp steps. This leaves two options: either (i) the multi-bp step size distribution is wrong, and likely suffers from multiple fast steps blending together in the 20 Hz data, or (ii) my results are incorrect. Unsurprisingly, I think option (ii) is unlikely. With my high spatial and temporal precision, I was able to better resolve many fast unwinding runs as being composed of successive 1-bp steps (c.f., Figure 4.7C right). At lower resolution, these runs would have instead looked like larger, multi-bp steps. And if larger physical step sizes were indeed more common than 1-bp steps, I should have seen them, as they would have been easier to resolve. But I did not. Therefore, I think it is likely that the multi-bp step distribution is incorrect: *E. coli* RecQ takes a majority of 1-bp unwinding steps, as expected from its known translocation step size. That said, I cannot definitively state whether or not RecQ *only* takes 1-bp steps; it is certainly possible that it rarely takes larger steps, and I certainly observed 0.5 bp steps in my experiments, though my S/N is not high enough to further pursue that analysis.

Let us return to the subject of RecQ back steps during unwinding (Figure 4.7B). These back steps occurred both as single events and as multiple, distinct steps, typically once RecQ made its way a few bp into the hairpin. Back steps were always soon followed by the resumption of normal forward unwinding, evidence that the RecQ conformation during both step types is not drastically different. In addition, the prevalence of back steps increased as [ATP] decreased. Linking these observations with the hypothesized structure for RecQ binding to DNA (Figure

1.4C) presents a possible mechanism: slippage of the RecA-like domains from their ssDNA track. If the binding between the ssDNA nucleotides and the RecA-like domains briefly broke, the RecQ zinc-binding and winged-helix domains that loosely associate to the dsDNA portion of the junction could keep the protein loosely bound. In that instant, the ssDNA would be free from tension and could start zipping itself. After one nucleotide zipped into the dsDNA, the remaining ssDNA nucleotides would once again be in register with the RecA-like domains, allowing them to rebind. Given low [ATP] conditions, the process could repeat until the RecQ rebound to the substrate firmly. However, this mechanism does not adequately explain how multiple, relatively slow 1-bp back steps can occur in succession. It is unlikely for slippage to repeat with such slow regularity, often with a speed comparable to forward steps (c.f. Figure 4.7B).

Another possibility is that these back steps are really forward steps along the opposite strand. In other words, RecQ briefly switches translocation strands and lets the unwound hairpin close behind it as it moves away from the ss-dsDNA junction. It is clear from my data that RecQ can switch strands in some capacity, as I often observe a single helicase unwind the same hairpin multiple times. This behavior can be seen in prior figures (Figure 4.4, black and Figure 4.6A) as well as in figures from upcoming sections (Figures 4.10A, 4.13A, and 4.14A). Such repeated unwinding can only occur if, after unwinding the full hairpin stem, the helicase then continues translocating down the complementary strand and eventually switches back to unwind the re-zipped hairpin. If it is possible for RecQ to strand switch after unwinding the full hairpin, it may be possible for it to strand switch during normal unwinding. This mechanism could explain both the existence and dynamics of the observed back steps, but it is not without issues. The most glaring issue is the large conformational change that needs to occur: can such a position switch

happen quickly, without inducing large-scale hairpin zipping when the helicase lets go of the substrate (c.f. Figure 4.7B)?

To my knowledge, the *E. coli* RecQ has never been shown to take back steps before, although strand-switch-based back steps have been observed in the *A. thaliana* RECQ2 homolog (134). It is not surprising that they went unobserved in previous *E. coli* RecQ studies, as bulk assays could not detect them and single-molecule assays used either very high ATP (1 mM) or very low ATP (~2-5 μ M). Neither condition is ideal for producing back steps, since high [ATP] keeps RecQ driving forward with little chance of slippage or strand switching, while low [ATP] prevents RecQ from unwinding more than a couple steps. Without opened nucleotides to close, and potentially enough room to strand switch, backsteps cannot occur or be detected.

In the course of this project, I have not seen any evidence of a 5-bp kinetic step, even in longer stepping traces (Figure 4.7C). To review, my collaborators believe they see systematic pausing in RecQ unwinding once every ~5 bp, which they think arises from RecQ occluding and then releasing unwound nucleotides (91). On the other hand, I have never observed this kind of pausing, either in RecQ ^{Δ H} or RecQ^{WT} unwinding traces. To better understand this disagreement, I created some simulated data meant to reproduce their magnetic tweezers data and analyzed it with their t-test-based step-finding algorithm (101). Their data for RecQ unwinding was taken at 200 Hz with 1 mM ATP, and the standard deviation of their thermal noise appeared to be ~5 bp (putting their expected S/N close to 1). I then generated simulated RecQ stepping data with these values using only exponentially distributed 1-bp steps (Figure 4.9A). I used a value of 0.0135 s for the exponential time constant, which empirically produced a mean unwinding rate of ~60 bp/s, comparable to my previously measured 1 mM ATP RecQ speeds (section 3.4).

Fitting this data with the step-finding algorithm produced a fit that had a roughly Gaussian distribution of step sizes centered on 5.5 bp (Figure 4.9B). Since the real distribution is made up of only 1-bp steps (although multiple 1-bp steps can come right after another, due to the combination of fast stepping speed and low bandwidth), something is clearly going wrong. The most likely explanation is that the 5-bp noise completely dominates the real 1-bp signal, and since the algorithm is designed to fit only statistically significant differences in extension, it is effectively fitting the noise. This conclusion, combined with the previous absence of 5-bp kinetic step size data on my end, indicates that this kinetic step size is likely not real, but merely a product of fitting low S/N data. Given that this kinetic step size and the prior multi-bp step size distribution were both postulated to occur due to RecQ occluding multiple unwound nucleotides, and that now I have given evidence that both conclusions were drawn from over-interpreting low resolution data, I think we can conclude that there is currently no evidence for RecQ to possess any nucleotide-occluding capacity. It simply takes very fast 1-bp steps.

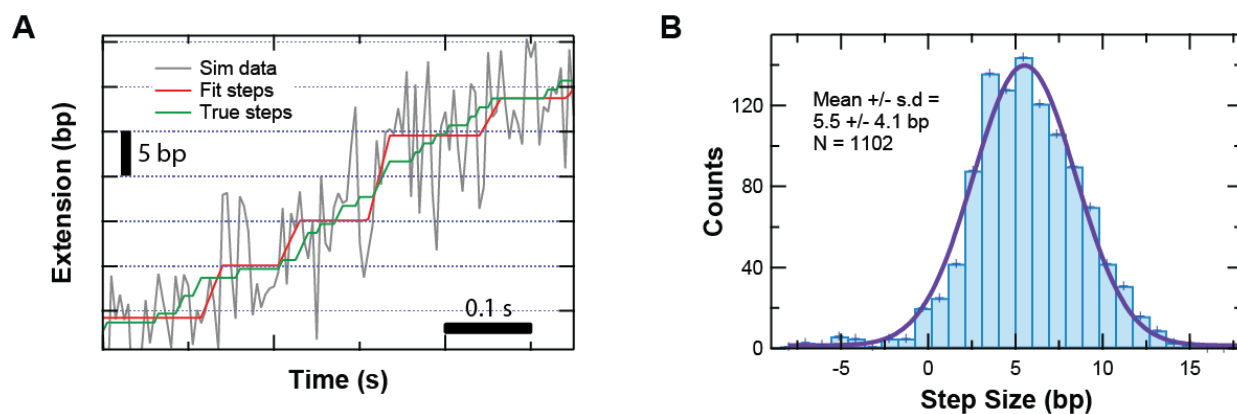


Figure 4.9: Fitting simulated magnetic tweezer steps.

A) Example trace for simulated 200 Hz 1-bp steps with 5-bp noise (grey) from a magnetic tweezers assay. The true steps (green) followed a single exponential time distribution with a time constant of 0.0135 s (equivalent to a ~60 bp/s unwinding speed to simulate 1 mM ATP conditions). The fit steps (red) arise from a t-test-based step-finding algorithm that looks for significant differences in extension noise. B) Histogram for the fit step sizes ($N = 1102$) for a simulated 100 s trace. From the Gaussian fit giving a mean step size of 5.5 bp, it would seem the fitting algorithm primarily fit the 5 bp noise in the trace.

4.2 Unwinding “popping” behavior

In previous sections, I worked to optimize the ATP concentration so that RecQ^{ΔH} would unwind slowly but with adequate processivity for a stepping assay. During that search, I checked to see how 300 pM RecQ^{ΔH} interacted with activated 50% GC DNA hairpins when no ATP was in solution. I expected to see flat traces with no activity, since RecQ’s translocase and helicase activities are known to be ATP dependent. However, that is not what I saw. While no ATP-less translocase activity was observed (my assay cannot detect translocation), I did observe ATP-less helicase activity at the activated hairpin. Unlike the smoothly sloped and processive extension increases from ATP-dependent unwinding, this ATP-less unwinding produces “popping” events where the extension sharply increases and decreases repeatedly (Figure 4.10A).

These transitions appear near-instantaneous in the 1 kHz extension data bandwidth, a marked difference from the usual RecQ unwinding signal. However, extension data is inherently force dependent, so judging the exact sharpness of large transitions can be hard since dramatic shifts in force skew the signal before the force clamp can react. Polymer folding studies remedy this by converting extension into contour length, a force-independent quantity. To create a contour length trace, the measured force and extension traces are combined in an eWLC (see section 1.2). The benefit of this approach is that the contour length shows the real sharpness of transitions; the cost is an increase in apparent noise.

Noise increases because the recorded force data used in the contour length conversion is *not* the exact force on the DNA. We record force by measuring the trap’s force on the bead; the mean value of this force is the same as the force on the DNA, but the thermal force fluctuations are *anti*-correlated. For example, thermal bead kicks towards the DNA reduce the DNA’s tension since the bead is not pulling as hard. In contrast, the trap’s force on the bead increases because

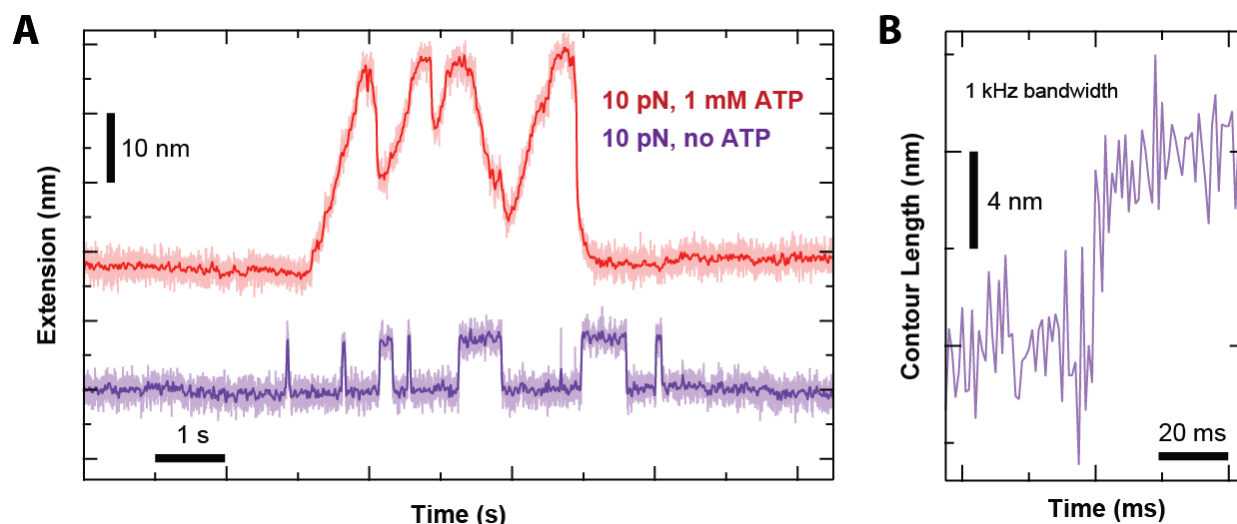


Figure 4.10: ATP-less RecQ popping of DNA hairpins.

A) Comparison of two 10 pN RecQ unwinding traces, one with saturating ATP (red) and one with no ATP (purple). Light: 1000 Hz, Dark: 100 Hz. Unexpectedly, RecQ displays a strange unwinding behavior when no ATP is in solution. B) A 1000 Hz contour length trace shows the “popping” event happens instantaneously, indicating that an unwinding mechanism distinct from normal, ATP-utilizing unwinding must be involved.

the bead is now further away from trap center. Combining the bead's force and tether's extension to produce contour length amplifies the apparent thermal noise by effectively counting it twice, once for each trace. However, so long as the transitions of interest are larger than the noise, this is only a minor problem. A slightly deeper problem is that extension traces can only be converted into a single polymer's contour length; you have to pick one polymer model for the calculation. Since my construct is dominated by the extension of dsDNA handles, I convert to dsDNA contour length. However, my signal arises from ssDNA unwound from the hairpin stem, so modeling it as dsDNA introduces some error. That said, I only care about obtaining a clear transition time and a relatively accurate length change, so the expected ~15% contour length magnification from treating ssDNA like dsDNA at 8 pN is acceptable.

The contour length trace reveals that the “popping” transitions are indeed very fast, unwinding 7 nm almost instantaneously for a 1000 Hz bandwidth. This gives a lower estimate of ~7000 nm/s for the unwinding speed (Figure 4.10B), two orders of magnitude faster than the mean unwinding speed at *saturating* [ATP] found in the last chapter, where RecQ^{ΔH} unwound 50% GC DNA at ~45 nm/s (extension unwinding; section 3.4). From this dramatic difference, popping and normal, ATP-dependent unwinding likely occur via different mechanisms. What then is the mechanism, and is it biologically relevant to RecQ? ATP-less unwinding activity is known to be relevant to many other helicases; specifically, it is well-established for the largest SF2 helicase family: the DEAD-box RNA helicases (69, 135, 136). The unwinding mechanism for these proteins appears to be duplex destabilization via energetically-favorable binding, which unwinds 8-20 bp segments of dsRNA and DNA-RNA hybrids (but not dsDNA). This destabilization occurs without ATP, but binding ATP increases substrate affinity and hydrolyzing ATP appears necessary for unbinding and restarting the unwinding cycle.

In contrast to this, I observe completely ATP-less binding, unwinding, and (apparent) unbinding by RecQ^{ΔH} on DNA hairpin substrates under tension. I say apparent unbinding because my instrument cannot definitively detect binding and unbinding, unlike more complex optical traps integrated with single-molecule fluorescence (137, 138). I can only infer binding and unbinding events by pauses of inactivity before and after unwinding events, respectively. For example, performing this ATP-less assay at 8 pN produces traces that are largely blank (aside from instrument drift) with an occasional popping event (Figure 4.11A, blue). Due to the large time intervals between the events, we assume they are from separate helicases, and that binding and unbinding events flank them. However, we cannot specify the exact times. One might expect that they occur directly before and after the unwinding event, but increasing the tension to 10 pN disproves that notion (Figure 4.11B, green). At this force, multiple popping events take place in succession, spanning time intervals from 3 s to 8 s. Thus at lower force it is likely that the RecQ stays bound to the substrate for much longer than the popping event implies.

Interestingly, though, the extended series of popping events are still flanked by long time intervals of inactivity. If we assume that each condensed series of pops corresponds to one RecQ^{ΔH} binding event, then the overall rate of RecQ^{ΔH} binding appears similar at 8 pN and 10 pN. This is expected, since the [RecQ^{ΔH}] is the same and RecQ^{ΔH}'s on-rate has no clear force dependence. In contrast, the popping frequency *within* one of these bound intervals increases dramatically with higher force. Thus the traces gives us a preliminary notion for how RecQ^{ΔH} interacts with the substrate: it binds near the hairpin junction at a rate independent of force, and once there periodically “pops” open the hairpin with a force-dependent rate (higher force for more events). Note that I specify the ss-dsDNA junction here, since only junction unwinding can be detected in this assay (internal melting further up the hairpin stem would not add extension

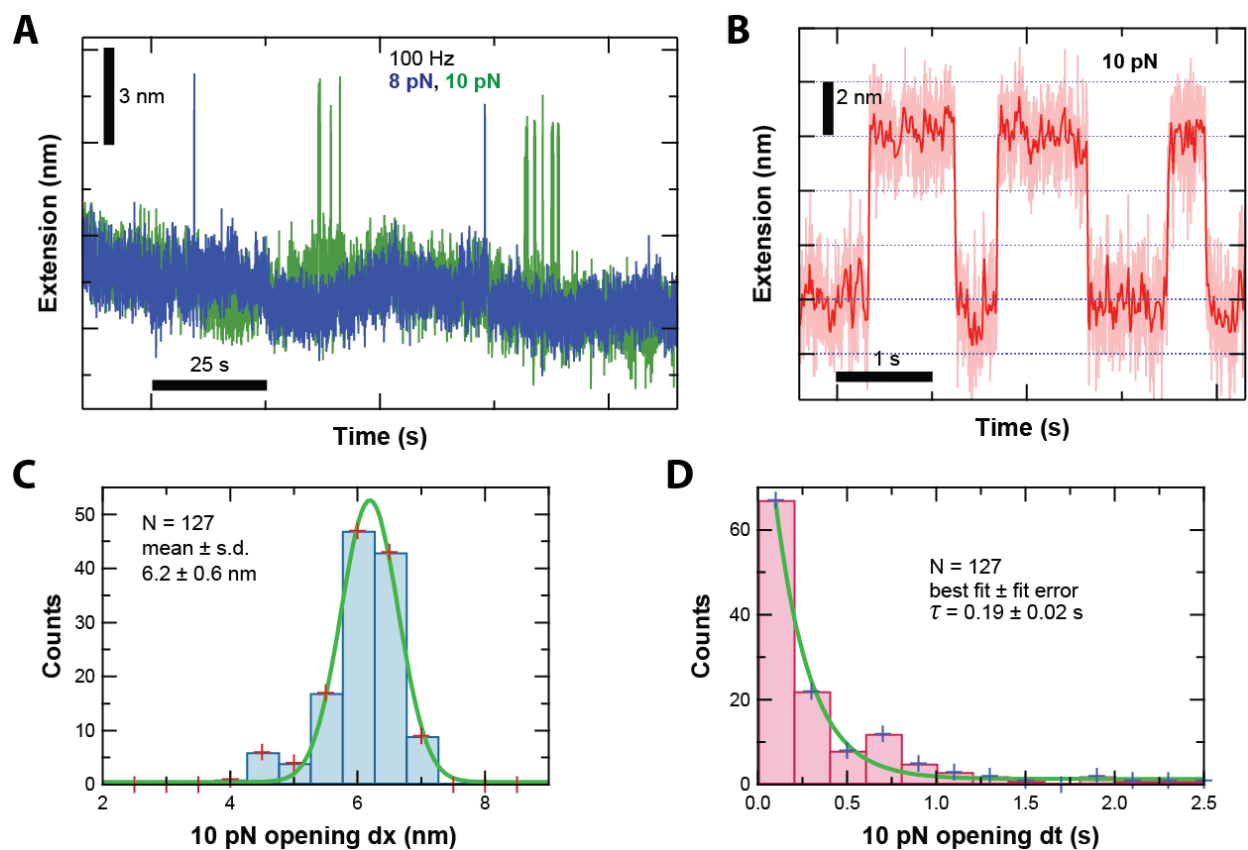


Figure 4.11: Quantifying the popping phenomenon.

A) Varying the tension affects the likelihood of popping in some capacity. At 10 pN (green), the RecQ^{AH} repeatedly pops open the hairpin stem in bursts, compared to the less active 8 pN trace (blue). However, the overall likelihood of there being *some* number of popping events per unit time does not seem to shift in these traces, indicating that force may increase the number of popping events, but RecQ binding determines if any take place. B) A close-up example of one of the repeated popping events. The opening size appears consistent. C) A distribution of 10 pN opening sizes (N = 127) fit with a Gaussian. D) A distribution of the opening times, i.e. the length of time any popping event lasts (N = 127) fit with a single exponential.

into the tether). Force dependence implies the popping is resisted by duplex stability, since using force to lower that stability increases the popping rate. The opening distances are also fairly consistent, and therefore may hold information about the underlying mechanism (Figure 4.11B).

Using 10 pN data to collect enough popping events, I measured the extension change for each clear opening. Plotting these values in a histogram ($N = 127$), we find that they can be fit by a Gaussian with a mean and standard deviation of 6.2 ± 0.6 nm (Figure 4.11C). If we assume the extension change is solely due to ssDNA being released into the tether (and not from distortions to the ssDNA landing site), then we can convert into unwound nucleotides. At 10 pN, unwinding 1 bp generates 0.826 nm of extension change, which means a 6.2 nm change must arise from ~ 7.5 bp, or 15 nt of ssDNA. The length of time each pop lasts can also be quantified; fitting this distribution with a single exponential produces a time constant of 0.19 ± 0.02 s (Figure 4.11D). This time distribution indicates that the popping interaction is somewhat stable, as the times last from milliseconds to seconds (as opposed to micro- or nanoseconds). Multiple openings also tell us that the interaction can repeatedly occur and be recovered from in a single RecQ binding event. This likely means that some part of the RecQ is continuously, stably bound during the entire popping process.

However, it is unclear whether monomers or multimers of RecQ^{ΔH} are the active agents. The work discussed in section 3.3 indicates that monomers should be the only species present, and current data implies that, as well. While collecting very low ATP unwinding traces for my 1-bp RecQ step search, such as 5 μM ATP in a 12 pN force clamp, I would sometimes observe both types of unwinding, sharp pops and processive unwinding, in a single trace (Figure 4.12A). The rapid transitions from popping to processive unwinding imply that a single type of RecQ^{ΔH} generates both, assumedly a monomer given my past findings. It also implies that the binding

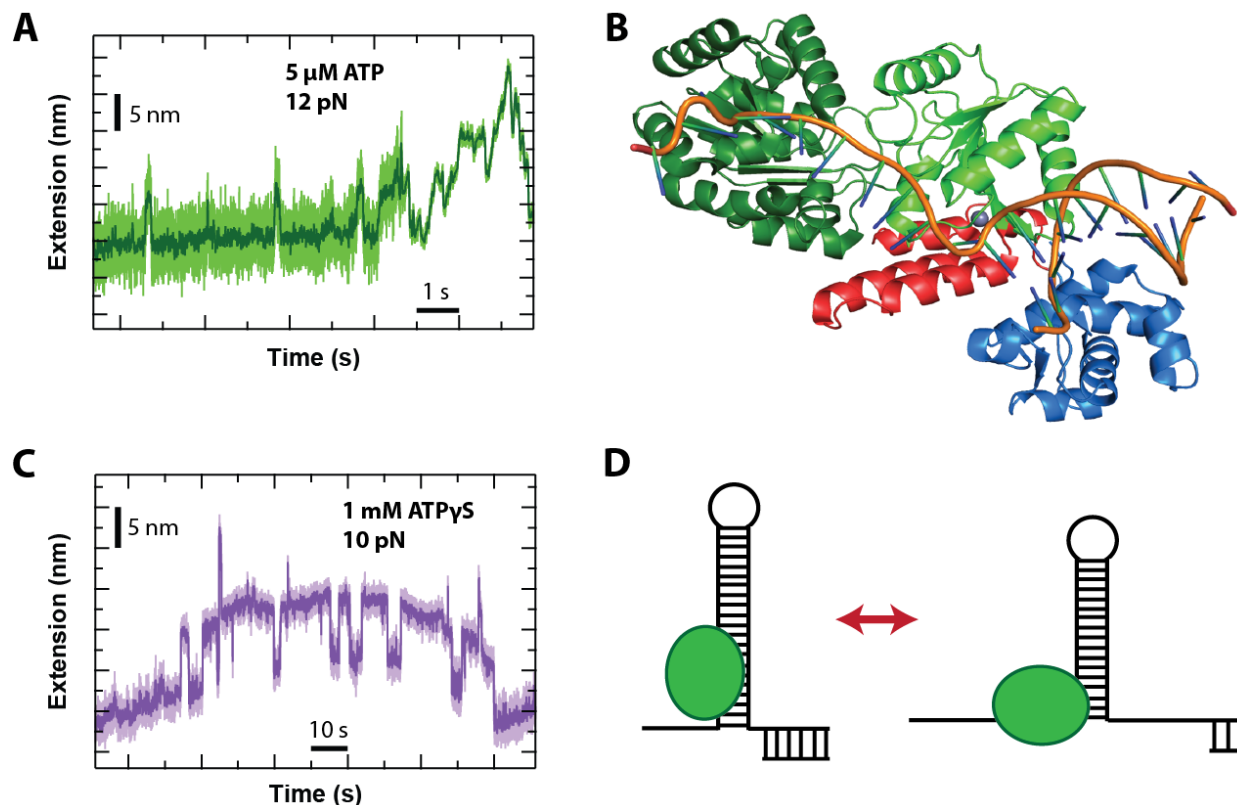


Figure 4.12: Structural implications of the popping behavior.

A) At low [ATP], normal unwinding and popping can both occur. High trap stiffness was activated once processive unwinding began. B) The crystal structure of the RecQ homolog from *C. Sakazakii* bound to forked DNA (PDB 4TMU), which we assume is close to how *E. coli* RecQ binds its substrate. C) Popping can also take place in 1 mM ATP γ S, with noticeably longer opening times and occasional secondary pops. D) A cartoon of one possible mechanism for popping. The RecQ may bind the hairpin stem in such a way that some number of base pairs becomes destabilized. If that happens, the tension across the remaining base pairs may be enough to unzip them. Openings would last until RecQ changes its position and allows the hairpin to reclose.

mode for popping cannot differ too much from normal binding, which we assume is akin to the *C. sakazakii* homolog structure (Figure 4.12B). To gain a better understanding of what exactly causes the pops, we can next ask whether slight structural differences change the behavior, such as those between free RecQ^{ΔH} and RecQ^{ΔH} bound to ATPγS. Does popping occur when a nucleotide is bound between the RecA-like domains? Putting 1 mM ATPγS in solution with RecQ^{ΔH} does produce popping behavior, but with some clear differences from the 0 ATP case (Figure 4.12C). Qualitatively, it seems the ATPγS increases the stability of the popped structure, as those states last for much longer here (10s of seconds). Interestingly, there are sometimes further, brief extension increases on top of the initial, longer-lasting pops. A few instances of this behavior were observed in 0 ATP traces, but it occurs more frequently in the ATPγS data.

From all of this disparate information, can we synthesize a plausible mechanism? The extension data indicate that ~7.5 bp of hairpin stem, or 15 nt of ssDNA, is being unwound and released into the tether. The time distribution indicates that the popped state is somewhat stable, and the low ATP traces implicate a monomer as the phenomenon's source. Importantly, popping is a force-dependent process. One possible mechanism is that RecQ^{ΔH} binds near the ss-dsDNA junction, but *not* in its assumed normal position, and slightly destabilizes part of the hairpin stem (Figure 4.12D). Why does this work? Hairpins can be unzipped by force, with prior work showing that 8 pN can unzip 8 bp stems (20). The pops are consistent with an ~8 bp hairpin opening, which can be done purely through force in these 8-12 pN force-clamp assays. Given our 40 bp hairpin substrate, this could only occur if RecQ destabilized part of the stem such that the only resistance to unzipping at the junction was from less than 8 bp of dsDNA. Internally destabilizing the dsDNA, like the DEAD-box RNA helicases mentioned above, would then release the nucleotides between the junction and destabilization point into the tether. If the

destabilizing binding between the RecQ^{ΔH} and DNA is strong, the RecQ^{ΔH} can also trap the DNA, preventing it from re-zipping until the RecQ^{ΔH} moves away. This would lead to the somewhat long-lasting observed popping events. Importantly, the data indicates that RecQ^{ΔH} cannot be in its assumedly normal, junction-binding position while popping occurs. If it was, it would act like a clamp between the ssDNA landing site and part of the hairpin stem, since it is attached to both (Figure 4.12B). In the case of a pop, this would prevent half of the released nucleotides from entering the tether and increasing the extension. Thus to get ~15 nt released into the tether, 30 bp would have to be unwound, something sterically impossible here.

While this is one possible mechanism, it is obviously not the only possible one; to further support or refute any model, we need more data. One avenue is the biochemical variations discussed previously (section 4.1.3), applied to this behavior. Another is to use RecQ^{WT} and RecQ mutants to try and identify which domains are important for the popping interaction. A promising candidate would be RecQ^{ΔWH}, a RecQ variant with both its HRDC and winged-helix domains deleted; given the assumed flexibility of the WH domain, it is likely to be involved in mediating the popping. Yet even if a mechanism is determined, it remains to be seen whether this behavior is biologically relevant. Though popping only takes place regularly under strain, there are several possible strained structures, such as improperly annealed strands or recombination intermediates, where this behavior may aid RecQ in its fundamental repair and recombination unwinding activity.

As a final note, one may ask why this behavior was never reported in prior studies. The reason is the same as for RecQ back steps: the two kinds of prior studies were bulk biochemical and single-molecule magnetic tweezers studies. As we have seen, the opening distance is ~8 bp, and its frequency is force-dependent. Without external force or exotic substrates, it is likely that

the opening rate is practically zero, and therefore bulk studies would never detect it. For magnetic tweezers, experiments reported thus far have typically used only high [ATP], and so would not observe the low-to-zero ATP popping behavior.

4.3 Additional non-standard interactions of RecQ and DNA

In the last section, we saw that RecQ^{ΔH} could generate large unwinding “pops” when there was no ATP in solution. Those were not the only rapid extension shifts I observed. In the presence of ATP, right before normal unwinding on activated hairpin constructs, I would sometimes observe sharp, brief extension decreases (Figure 4.13A). Even more rarely, I would occasionally see these spikes in isolation, with no unwinding following them. To my knowledge, this behavior has never been reported in a helicase before. So like in the last section, I want to determine the mechanism behind these strange signals, and whether it is biologically relevant.

To get a general idea of the mechanism, we need to note two things. First, these spikes occur as extension drops below the baseline, which in my activated hairpin substrates are only possible if part of the tether gets scrunched together. We can quantify these spikes by taking an 8 pN sample (N = 23) and finding its mean and standard deviation (Figure 4.13B). From this, it is clear the spikes cluster around a mean value of 3.5 ± 0.7 nm (not in a Gaussian distribution, at least at this sample size). The second thing to note is the timing: the extension drops either occur in isolation or before unwinding begins, never during or after. Therefore, they likely are associated with a kinetic step that precedes unwinding, namely RecQ^{ΔH} binding and/or unwinding initiation. The fact that unwinding can almost *immediately* follow these events indicates that they likely take place close to the hairpin junction. From these points, we can infer that during binding and/or initiation, RecQ^{ΔH} has a chance of coming in contact with spatially

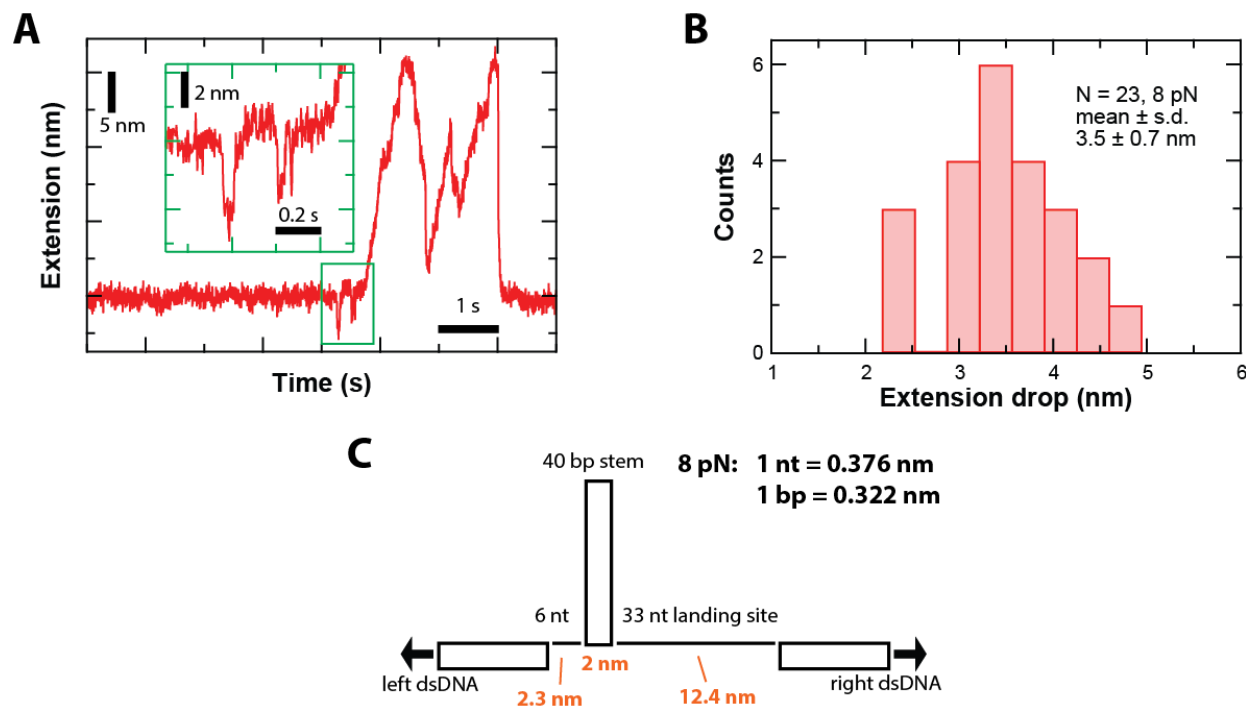


Figure 4.13: RecQ can induce sharp extension drops prior to unwinding.

A) A normal RecQ unwinding trace at 1 mM ATP. Before the start of processive unwinding, several sudden extension drops can be seen. These drops are bizarre, as there is no expected way to generate extension drops in a fully wound hairpin substrate. They can be occasionally seen before unwinding or in isolation, but never after unwinding. B) A small distribution of sizes for the extension drops ($N = 23$) at 8 pN. They seem to cluster around a mean value of ~ 3.5 nm. C) Diagram of the 40 bp hairpin construct with expected extensions at 8 pN tension. To generate the extension drops, some part(s) of the orange labeled lengths must decrease.

separate parts of the tether and briefly bending them closer together. Given that the drops are rare and have moderate dwell times ($0.07 \text{ s} \pm 0.04 \text{ s}$, $N = 23$), we can assume that they are due to non-standard interactions between the helicase and DNA. If this is true, looking at the substrate structure may help identify exactly where and how these events take place.

Given that the activated substrate is made up of ssDNA and dsDNA sections, one may ask whether one type is more easily bent than the other. To answer that, recall that ssDNA has a much lower persistence length than dsDNA (0.75 nm vs. 50 nm; see section 1.2), meaning it is much easier to bend. Looking at a diagram of the substrate, there are two ssDNA locations where the extension might be compressed, the 6 nt left side and the 33 nt right side (Figure 4.13C). At 8 pN tension, these sections will be 2.3 nm and 12.4 nm long, respectively. In contrast, it is hard to imagine the RecQ changing the extension of the dsDNA handles or the 2 nm width of the hairpin stem. So what interactions could generate these spikes? The maximum extension drop one could get from the left ssDNA section is ~ 2 nm, assuming the hairpin stem touches the left dsDNA handle and creates a tensionless 6 nt loop. This is not enough to account for the recorded spike sizes. Therefore, the majority of spikes must involve at least the 33 nt side (possibly both sides).

Considering that RecQ's RecA-like domains bind to ssDNA and its zinc-binding and winged-helix domains associate with dsDNA, there are two probable geometries for these spikes. Each involves RecQ binding non-neighboring parts of the DNA substrate, likely due to strong thermal kicks briefly bringing these parts close enough together to both interact with RecQ. The first solely involves the RecA-like domains binding to non-consecutive nucleotides, forming a loop of tensionless ssDNA. The second involves the winged-helix domain; if it can rotate up to 90° like in the homolog structure (83), it could bind faraway dsDNA such as the left handle or distant parts of the hairpin, contracting the tether extension and leading to the observed drops. A

simple way to discover if this geometry is right would be to use RecQ^{ΔWH}, the RecQ mutant with both its HDRC and winged-helix domains deleted, and see if the spikes persist. Sadly, as I could not obtain these enzymes myself, I have not performed this experiment.

Another strange interaction between RecQ and its DNA substrate often occurred just before the end of hairpin unwinding: a pause followed by the sudden unzipping of the rest of the hairpin (Figure 4.14A). Unlike the spikes, this behavior is rather common; for instance, it can be seen in multiple previous plots in this thesis (c.g., Figures 4.4 and 4.6). In addition, it has also been observed by an independent group using a completely different DNA hairpin and type of RecQ (Figure 3b in Ref. (134), using a plant RecQ from *A. thaliana*). Clearly, force-induced unzipping of the remaining short hairpin stem causes the sudden opening, as discussed in section 4.2; that in itself is not surprising. The surprising part is that these events are preceded by notable pauses, even at saturating [ATP] where pauses are nearly non-existent. Why? If the RecQ simply unwound the hairpin stem until it could no longer resist the tension, one would expect a pop to occur instantaneously. Instead there are significant dwells in the traces. Quantifying the sizes of the pops and dwells may help elucidate these events.

Given that helicase pausing and unwinding distances can typically both be modulated by applied force, I collected top extension changes (Figure 4.14B) and stall times (Figure 4.14C) from both 8 pN (red, N = 41) and 10 pN (grey, N = 52) data sets using 1 mM ATP. The distributions for the top pops could both be well-fit by Gaussians: the 8 pN distribution has a Gaussian fit of 6.1 ± 1.7 nm (mean \pm s.d.), while the 10 pN one has a fit of 7.0 ± 1.3 nm (mean \pm s.d.). While these means are within one standard deviation, the overall distributions are clearly distinct from one another. To further investigate whether they could be related, I tried converting the extension changes into unwound base pairs. This conversion had to account for the difference

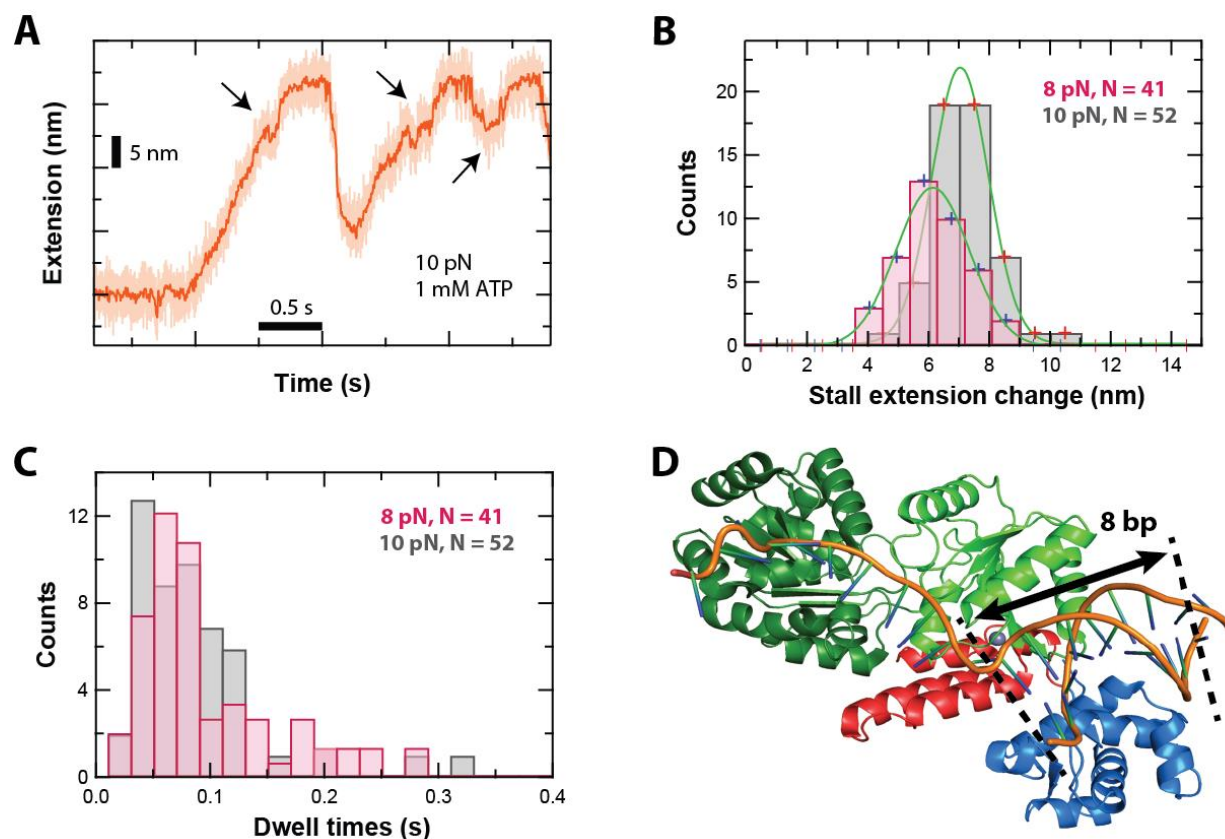


Figure 4.14: RecQ can stall force-induced hairpin unzipping.

A) During processive unwinding, RecQ^{ΔH} will often stall before the hairpin completely unzips, followed by a sharp unzipping event. The extension change between the stall position and the completely unwound hairpin is relatively consistent. B) Measuring extension pops after stalls at 8 pN (pink, N = 41) and 10 pN (grey, N = 52). Both distributions produce a similar mean value when converted into force-independent base pairs. C) The dwell time distributions for the stalls from (B). They appear to have a roughly exponential decay. D) If *E. coli* RecQ has a similar binding structure as the *C. Sakazakii* homolog, its translocation might stall when its dsDNA-binding domains encounter the hairpin loop. After a time, the applied force may then open the remaining hairpin stem.

in 8 pN vs. 10 pN extension, as well as the extension change brought about by unwinding the last base pair in the hairpin (2 nt from the base pair + 4 nt from the loop are added; 2 nm from the fixed stem width are subtracted). Interestingly, unwinding the last 9 bp of the hairpin at 8 pN results in a total extension change of 6.25 nm, very close to the 6.1 nm fit mean. Moreover, unwinding the last 9 bp at 10 pN results in an extension change of 7.1 nm, also very close to the 7.0 nm fit mean. Therefore, both distributions could be interpreted as being the *same* distribution, with the extension values shifted due to applied force. This would implicate a force-independent mechanism somehow related to the 9 bp value of both means.

The dwell time distributions for the two forces are more similar than the corresponding extension ones, although they do not have a well-defined shape. Looking at the bulk of the data, most dwells appear to last 25 to 100 ms, which is a non-trivial amount of time on the single-molecule level. To instigate such dwells, the cause must present a significant barrier to normal unwinding, and must be able to do so repeatedly given the frequency of the events. On that note, the above data sets were collected with the intent of investigating the pause-then-pop phenomenon; therefore, traces not exhibiting that behavior were excluded. While common, this phenomena was by no means universal; many traces unwound the entire hairpin without any pause or pop. Whether or not this was a helicase-dependent effect – that traces either had top popping or they did not – has not been quantitatively analyzed. However, my qualitative answer is no: unwinding runs from a single molecule could both complete the hairpin without incident or undergo a pause-then-pop.

Given this information, what conclusions can we draw? The relative force-independence of both the dwell time and pop size distributions suggests that the substrate parts under tension, the dsDNA handles and the ssDNA sections, are not the source of the pauses. Since the source

must involve RecQ interactions with DNA in some way, that leaves only the hairpin itself as a potential cause. And this leads us to revisit an interesting fact about the RecQ homolog structure from Ref. (83). When the homolog binds to the forked substrate, it unwinds 2 bp of the original 10 bp hairpin stem, leaving 8 bp associated with the enzyme (Figure 4.14D). This conformation likely arises from packing constraints in the protein crystal; in other words, this amount of hairpin stem somehow fits well with the protein, perhaps by limiting the stem length jutting out from the bulk of the protein. This would put the hairpin loop right next to the RecQ domains. Could the hairpin loop serve as an obstacle to further unwinding, perhaps because the geometry of the loop differs so much from the double helix? This is my current imagined model for how these top popping events take place, given the striking similarity of the crystal's 8 bp stem length to the current assumed 9 bp stem unwinding. RecQ unwinds processively until its dsDNA-associating domains encounter the hairpin loop, whose geometry makes it more difficult to associate with. Depending on thermal fluctuations, the helicase can either stall here or overcome the kinetic barrier and continue unwinding. If it stalls, the tension across the tether is sufficient to eventually unzip the remaining hairpin, allowing RecQ to continue translocation.

Obviously this is a speculative model; my current data does not allow me to determine a more definitive one. Like the other strange phenomena discussed in this and the prior section, collecting data with RecQ^{WT} and RecQ^{ΔWH} would be very informative. The addition or loss of a dsDNA-associating domain could dramatically affect this behavior, especially if it is indeed due to helicase domains being blocked by the hairpin loop.

Bibliography

1. S. B. Smith, L. Finzi, C. Bustamante, Direct Mechanical Measurements of the Elasticity of Single DNA-Molecules by Using Magnetic Beads. *Science* **258**, 1122 (Nov 13, 1992).
2. C. Bustamante, J. F. Marko, E. D. Siggia, S. Smith, Entropic elasticity of lambda-phage DNA. *Science* **265**, 1599 (Sep 9, 1994).
3. S. B. Smith, Y. J. Cui, C. Bustamante, Overstretching B-DNA: The elastic response of individual double-stranded and single-stranded DNA molecules. *Science* **271**, 795 (Feb 9, 1996).
4. P. Cluzel *et al.*, DNA: An extensible molecule. *Science* **271**, 792 (Feb 9, 1996).
5. M. D. Wang, H. Yin, R. Landick, J. Gelles, S. M. Block, Stretching DNA with optical tweezers. *Biophys J* **72**, 1335 (Mar, 1997).
6. J. F. Allemand, D. Bensimon, R. Lavery, V. Croquette, Stretched and overwound DNA forms a Pauling-like structure with exposed bases. *P Natl Acad Sci USA* **95**, 14152 (Nov 24, 1998).
7. C. Bouchiat *et al.*, Estimating the persistence length of a worm-like chain molecule from force-extension measurements. *Biophys J* **76**, 409 (Jan, 1999).
8. J. F. Leger *et al.*, Structural transitions of a twisted and stretched DNA molecule. *Phys Rev Lett* **83**, 1066 (Aug 2, 1999).
9. Y. Zhang, H. Zhou, Z. C. Ou-Yang, Stretching single-stranded DNA: interplay of electrostatic, base-pairing, and base-pair stacking interactions. *Biophysical Journal* **81**, 1133 (Aug, 2001).
10. C. Bustamante, Z. Bryant, S. B. Smith, Ten years of tension: single-molecule DNA mechanics. *Nature* **421**, 423 (Jan 23, 2003).
11. Y. Seol, J. Li, P. C. Nelson, T. T. Perkins, M. D. Betterton, Elasticity of Short DNA Molecules: Theory and Experiment for Contour Lengths of 0.6–7 μ m. *Biophys J* **93**, 4360 (2007).
12. T. R. Strick, J. F. Allemand, D. Bensimon, A. Bensimon, V. Croquette, The elasticity of a single supercoiled DNA molecule. *Science* **271**, 1835 (Mar 29, 1996).
13. E. L. Florin, V. T. Moy, H. E. Gaub, Adhesion forces between individual ligand-receptor pairs. *Science* **264**, 415 (Apr 15, 1994).
14. V. T. Moy, E. L. Florin, H. E. Gaub, Intermolecular forces and energies between ligands and receptors. *Science* **266**, 257 (Oct 14, 1994).
15. R. Merkel, P. Nassoy, A. Leung, K. Ritchie, E. Evans, Energy landscapes of receptor-ligand bonds explored with dynamic force spectroscopy. *Nature* **397**, 50 (Jan 7, 1999).
16. E. Evans, Probing the relation between force--lifetime--and chemistry in single molecular bonds. *Annu Rev Biophys Biomol Struct* **30**, 105 (2001).

17. J. Liphardt, B. Onoa, S. B. Smith, I. Tinoco, Jr., C. Bustamante, Reversible unfolding of single RNA molecules by mechanical force. *Science* **292**, 733 (Apr 27, 2001).
18. G. Neuert, C. Albrecht, E. Pamir, H. E. Gaub, Dynamic force spectroscopy of the digoxigenin-antibody complex. *Febs Lett* **580**, 505 (Jan 23, 2006).
19. M. T. Woodside *et al.*, Direct measurement of the full, sequence-dependent folding landscape of a nucleic acid. *Science* **314**, 1001 (Nov 10, 2006).
20. M. T. Woodside *et al.*, Nanomechanical measurements of the sequence-dependent folding landscapes of single nucleic acid hairpins. *P Natl Acad Sci USA* **103**, 6190 (Apr 18, 2006).
21. O. K. Dudko, G. Hummer, A. Szabo, Theory, analysis, and interpretation of single-molecule force spectroscopy experiments. *Proc Natl Acad Sci U S A* **105**, 15755 (Oct 14, 2008).
22. J. P. Junker, F. Ziegler, M. Rief, Ligand-Dependent Equilibrium Fluctuations of Single Calmodulin Molecules. *Science* **323**, 633 (Jan 30, 2009).
23. H. Yu, M. G. Siewny, D. T. Edwards, A. W. Sanders, T. T. Perkins, Hidden dynamics in the unfolding of individual bacteriorhodopsin proteins. *Science* **355**, 945 (Mar 03, 2017).
24. K. Svoboda, C. F. Schmidt, B. J. Schnapp, S. M. Block, Direct observation of kinesin stepping by optical trapping interferometry. *Nature* **365**, 721 (Oct 21, 1993).
25. J. T. Finer, R. M. Simmons, J. A. Spudich, Single myosin molecule mechanics: piconewton forces and nanometre steps. *Nature* **368**, 113 (Mar 10, 1994).
26. K. Visscher, M. J. Schnitzer, S. M. Block, Single kinesin molecules studied with a molecular force clamp. *Nature* **400**, 184 (Jul 8, 1999).
27. G. J. L. Wuite, S. B. Smith, M. Young, D. Keller, C. Bustamante, Single-molecule studies of the effect of template tension on T7 DNA polymerase activity. *Nature* **404**, 103 (Mar 2, 2000).
28. D. E. Smith *et al.*, The bacteriophage straight phi29 portal motor can package DNA against a large internal force. *Nature* **413**, 748 (Oct 18, 2001).
29. C. L. Asbury, A. N. Fehr, S. M. Block, Kinesin moves by an asymmetric hand-over-hand mechanism. *Science* **302**, 2130 (Dec 19, 2003).
30. T. T. Perkins, R. V. Dalal, P. G. Mitsis, S. M. Block, Sequence-dependent pausing of single lambda exonuclease molecules. *Science* **301**, 1914 (Sep 26, 2003).
31. M. N. Dessinges, T. Lionnet, X. G. Xi, D. Bensimon, V. Croquette, Single-molecule assay reveals strand switching and enhanced processivity of UvrD. *P Natl Acad Sci USA* **101**, 6439 (Apr 27, 2004).
32. E. A. Abbondanzieri, W. J. Greenleaf, J. W. Shaevitz, R. Landick, S. M. Block, Direct observation of base-pair stepping by RNA polymerase. *Nature* **438**, 460 (Nov 24, 2005).
33. S. Dumont *et al.*, RNA translocation and unwinding mechanism of HCV NS3 helicase and its coordination by ATP. *Nature* **439**, 105 (Jan 5, 2006).
34. J. D. Wen *et al.*, Following translation by single ribosomes one codon at a time. *Nature* **452**, 598 (Apr 3, 2008).
35. W. Cheng, S. G. Arunajadai, J. R. Moffitt, I. Tinoco, Jr., C. Bustamante, Single-base pair unwinding and asynchronous RNA release by the hepatitis C virus NS3 helicase. *Science* **333**, 1746 (Sep 23, 2011).
36. K. C. Neuman, A. Nagy, Single-molecule force spectroscopy: optical tweezers, magnetic tweezers and atomic force microscopy. *Nat Methods* **5**, 491 (Jun, 2008).

37. K. Svoboda, S. M. Block, Biological Applications of Optical Forces. *Annu Rev Biophys Biom* **23**, 247 (1994).
38. K. Visscher, S. P. Gross, S. M. Block, Construction of multiple-beam optical traps with nanometer-resolution position sensing. *Ieee J Sel Top Quant* **2**, 1066 (Dec, 1996).
39. K. C. Neuman, S. M. Block, Optical trapping. *Rev Sci Instrum* **75**, 2787 (Sep, 2004).
40. J. R. Moffitt, Y. R. Chemla, S. B. Smith, C. Bustamante, Recent advances in optical tweezers. *Annu Rev Biochem* **77**, 205 (2008).
41. T. T. Perkins, Optical traps for single molecule biophysics: a primer. *Laser Photonics Rev* **3**, 203 (Mar, 2009).
42. T. T. Perkins, Angstrom-precision optical traps and applications. *Annu Rev Biophys* **43**, 279 (2014).
43. A. Gennerich, Ed., *Optical Tweezers: Methods and Protocols*, vol. 1486 (Humana Press, New York, 2017), vol. 1486.
44. A. Ashkin, J. M. Dziedzic, J. E. Bjorkholm, S. Chu, Observation of a Single-Beam Gradient Force Optical Trap for Dielectric Particles. *Opt Lett* **11**, 288 (May, 1986).
45. J. D. Jackson, *Classical Electrodynamics*. (Wiley, New York, ed. 3rd, 1999).
46. R. K. Montange, M. S. Bull, E. R. Shanblatt, T. T. Perkins, Optimizing bead size reduces errors in force measurements in optical traps. *Opt Express* **21**, 39 (Jan 14, 2013).
47. J. SantaLucia, Jr., A unified view of polymer, dumbbell, and oligonucleotide DNA nearest-neighbor thermodynamics. *P Natl Acad Sci USA* **95**, 1460 (Feb 17, 1998).
48. J. D. Watson, F. H. Crick, Molecular structure of nucleic acids; a structure for deoxyribose nucleic acid. *Nature* **171**, 737 (Apr 25, 1953).
49. W. Saenger, *Principles of Nucleic Acid Structure*. C. R. Cantor, Ed., Springer Advanced Texts in Chemistry (Springer-Verlag, New York, 1984).
50. M. J. McCauley, M. C. Williams, Mechanisms of DNA binding determined in optical tweezers experiments. *Biopolymers* **85**, 154 (Feb 05, 2007).
51. A. Bosco, J. Camunas-Soler, F. Ritort, Elastic properties and secondary structure formation of single-stranded DNA at monovalent and divalent salt conditions. *Nucleic acids research* **42**, 2064 (Feb, 2014).
52. P. Gross *et al.*, Quantifying how DNA stretches, melts and changes twist under tension. *Nat Phys* **7**, 731 (Sep, 2011).
53. M. Rief, H. Clausen-Schaumann, H. E. Gaub, Sequence-dependent mechanics of single DNA molecules. *Nat Struct Biol* **6**, 346 (Apr, 1999).
54. H. Clausen-Schaumann, M. Rief, C. Tolksdorf, H. E. Gaub, Mechanical stability of single DNA molecules. *Biophys J* **78**, 1997 (Apr, 2000).
55. S. Cocco, J. Yan, J. F. Leger, D. Chatenay, J. F. Marko, Overstretching and force-driven strand separation of double-helix DNA. *Physical review E, Statistical, nonlinear, and soft matter physics* **70**, 011910 (Jul, 2004).
56. S. Whitelam, S. Pronk, P. L. Geissler, There and (slowly) back again: entropy-driven hysteresis in a model of DNA overstretching. *Biophys J* **94**, 2452 (Apr 1, 2008).
57. C. P. Calderon, W. H. Chen, K. J. Lin, N. C. Harris, C. H. Kiang, Quantifying DNA melting transitions using single-molecule force spectroscopy. *J Phys Condens Matter* **21**, 34114 (Jan 21, 2009).
58. J. van Mameren *et al.*, Unraveling the structure of DNA during overstretching by using multicolor, single-molecule fluorescence imaging. *Proc Natl Acad Sci U S A* **106**, 18231 (Oct 27, 2009).

59. D. H. Paik, T. T. Perkins, Overstretching DNA at 65 pN Does Not Require Peeling from Free Ends or Nicks. *J Am Chem Soc* **133**, 3219 (Mar 16, 2011).
60. X. H. Zhang *et al.*, Revealing the competition between peeled ssDNA, melting bubbles, and S-DNA during DNA overstretching by single-molecule calorimetry. *P Natl Acad Sci USA* **110**, 3865 (Mar 5, 2013).
61. G. A. King *et al.*, Revealing the competition between peeled ssDNA, melting bubbles, and S-DNA during DNA overstretching using fluorescence microscopy. *P Natl Acad Sci USA* **110**, 3859 (Mar 5, 2013).
62. L. Bongini, L. Melli, V. Lombardi, P. Bianco, Transient kinetics measured with force steps discriminate between double-stranded DNA elongation and melting and define the reaction energetics. *Nucleic acids research* **42**, 3436 (Mar, 2014).
63. X. Zhang *et al.*, Interconversion between three overstretched DNA structures. *J Am Chem Soc* **136**, 16073 (Nov 12, 2014).
64. I. D. Hickson, RecQ helicases: caretakers of the genome. *Nat Rev Cancer* **3**, 169 (Mar, 2003).
65. K. A. Bernstein, S. Gangloff, R. Rothstein, The RecQ DNA helicases in DNA repair. *Annu Rev Genet* **44**, 393 (2010).
66. D. L. Croteau, V. Popuri, P. L. Opresko, V. A. Bohr, Human RecQ helicases in DNA repair, recombination, and replication. *Annu Rev Biochem* **83**, 519 (2014).
67. M. R. Singleton, M. S. Dillingham, D. B. Wigley, Structure and mechanism of helicases and nucleic acid translocases. *Annu Rev Biochem* **76**, 23 (2007).
68. D. C. Beyer, M. K. Ghoneim, M. Spies, Structure and Mechanisms of SF2 DNA Helicases. *Adv Exp Med Biol* **767**, 47 (2013).
69. A. K. Byrd, K. D. Raney, Superfamily 2 helicases. *Front Biosci (Landmark Ed)* **17**, 2070 (Jun 1, 2012).
70. K. Umezū, K. Nakayama, H. Nakayama, Escherichia coli RecQ protein is a DNA helicase. *P Natl Acad Sci USA* **87**, 5363 (Jul, 1990).
71. K. Sarlos, M. Gyimesi, M. Kovacs, RecQ helicase translocates along single-stranded DNA with a moderate processivity and tight mechanochemical coupling. *P Natl Acad Sci USA* **109**, 9804 (Jun 19, 2012).
72. G. M. Harami, N. T. Nagy, M. Martina, K. C. Neuman, M. Kovacs, The HRDC domain of E. coli RecQ helicase controls single-stranded DNA translocation and double-stranded DNA unwinding rates without affecting mechanoenzymatic coupling. *Sci Rep* **5**, 11091 (2015).
73. K. Hanada *et al.*, RecQ DNA helicase is a suppressor of illegitimate recombination in Escherichia coli. *P Natl Acad Sci USA* **94**, 3860 (Apr 15, 1997).
74. F. G. Harmon, S. C. Kowalczykowski, RecQ helicase, in concert with RecA and SSB proteins, initiates and disrupts DNA recombination. *Genes Dev* **12**, 1134 (Apr 15, 1998).
75. F. G. Harmon, R. J. DiGate, S. C. Kowalczykowski, RecQ helicase and topoisomerase III comprise a novel DNA strand passage function: a conserved mechanism for control of DNA recombination. *Molecular cell* **3**, 611 (May, 1999).
76. F. G. Harmon, S. C. Kowalczykowski, Biochemical characterization of the DNA helicase activity of the escherichia coli RecQ helicase. *The Journal of biological chemistry* **276**, 232 (Jan 5, 2001).
77. D. A. Bernstein, M. C. Zittel, J. L. Keck, High-resolution structure of the E.coli RecQ helicase catalytic core. *Embo J* **22**, 4910 (Oct 1, 2003).

78. D. A. Bernstein, J. L. Keck, Conferring substrate specificity to DNA helicases: role of the RecQ HRDC domain. *Structure* **13**, 1173 (Aug, 2005).
79. A. Vindigni, F. Marino, O. Gileadi, Probing the structural basis of RecQ helicase function. *Biophys Chem* **149**, 67 (Jul, 2010).
80. M. C. Zittel, J. L. Keck, Coupling DNA-binding and ATP hydrolysis in Escherichia coli RecQ: role of a highly conserved aromatic-rich sequence. *Nucleic acids research* **33**, 6982 (2005).
81. R. D. Shereda, D. A. Bernstein, J. L. Keck, A central role for SSB in Escherichia coli RecQ DNA helicase function. *The Journal of biological chemistry* **282**, 19247 (Jun 29, 2007).
82. R. D. Shereda, N. J. Reiter, S. E. Butcher, J. L. Keck, Identification of the SSB binding site on E. coli RecQ reveals a conserved surface for binding SSB's C terminus. *J Mol Biol* **386**, 612 (Feb 27, 2009).
83. K. A. Manthei, M. C. Hill, J. E. Burke, S. E. Butcher, J. L. Keck, Structural mechanisms of DNA binding and unwinding in bacterial RecQ helicases. *P Natl Acad Sci USA* **112**, 4292 (Apr 7, 2015).
84. A. C. Pike *et al.*, Human RECQ1 helicase-driven DNA unwinding, annealing, and branch migration: insights from DNA complex structures. *P Natl Acad Sci USA* **112**, 4286 (Apr 7, 2015).
85. H. Q. Xu *et al.*, The Escherichia coli RecQ helicase functions as a monomer. *The Journal of biological chemistry* **278**, 34925 (Sep 12, 2003).
86. S. X. Dou, P. Y. Wang, H. Q. Xu, X. G. Xi, The DNA binding properties of the Escherichia coli RecQ helicase. *The Journal of biological chemistry* **279**, 6354 (Feb 20, 2004).
87. X. D. Zhang *et al.*, Escherichia coli RecQ is a rapid, efficient, and monomeric helicase. *J Biol Chem* **281**, 12655 (May 5, 2006).
88. N. Li *et al.*, Multiple Escherichia coli RecQ helicase monomers cooperate to unwind long DNA substrates: a fluorescence cross-correlation spectroscopy study. *The Journal of biological chemistry* **285**, 6922 (Mar 5, 2010).
89. B. Rad, S. C. Kowalczykowski, Translocation of E. coli RecQ helicase on single-stranded DNA. *Biochemistry* **51**, 2921 (Apr 3, 2012).
90. B. Rad, A. L. Forget, R. J. Baskin, S. C. Kowalczykowski, Single-molecule visualization of RecQ helicase reveals DNA melting, nucleation, and assembly are required for processive DNA unwinding. *P Natl Acad Sci USA* **112**, E6852 (Dec 15, 2015).
91. Y. Seol, G. M. Harami, M. Kovacs, K. C. Neuman, Homology sensing via non-linear amplification of sequence-dependent pausing by RecQ helicase. *Elife* **8**, (Aug 29, 2019).
92. J. B. Ma *et al.*, Asynchrony of Base-Pair Breaking and Nucleotide Releasing of Helicases in DNA Unwinding. *J Phys Chem B* **122**, 5790 (Jun 7, 2018).
93. G. M. Harami *et al.*, Shuttling along DNA and directed processing of D-loops by RecQ helicase support quality control of homologous recombination. *P Natl Acad Sci USA*, (Jan 09, 2017).
94. T. Hishida *et al.*, Role of the Escherichia coli RecQ DNA helicase in SOS signaling and genome stabilization at stalled replication forks. *Genes Dev* **18**, 1886 (Aug 1, 2004).
95. Z. S. Kocsis, K. Sarlos, G. M. Harami, M. Martina, M. Kovacs, A nucleotide-dependent and HRDC domain-dependent structural transition in DNA-bound RecQ helicase. *The Journal of biological chemistry* **289**, 5938 (Feb 28, 2014).

96. F. Gittes, C. F. Schmidt, Interference model for back-focal-plane displacement detection in optical tweezers. *Opt Lett* **23**, 7 (Jan 1, 1998).
97. A. Pralle, M. Prummer, E. L. Florin, E. H. K. Stelzer, J. K. H. Horber, Three-dimensional high-resolution particle tracking for optical tweezers by forward scattered light. *Microsc Res Techniq* **44**, 378 (Mar 1, 1999).
98. R. Walder, D. H. Paik, M. S. Bull, C. Sauer, T. T. Perkins, Ultrastable measurement platform: sub-nm drift over hours in 3D at room temperature. *Opt Express* **23**, 16554 (Jun 29, 2015).
99. R. Walder *et al.*, Rapid Characterization of a Mechanically Labile alpha-Helical Protein Enabled by Efficient Site-Specific Bioconjugation. *J Am Chem Soc* **139**, 9867 (Jul 26, 2017).
100. T. T. Perkins, H. W. Li, R. V. Dalal, J. Gelles, S. M. Block, Forward and reverse motion of single RecBCD molecules on DNA. *Biophys J* **86**, 1640 (Mar, 2004).
101. Y. Seol, M. P. Strub, K. C. Neuman, Single molecule measurements of DNA helicase activity with magnetic tweezers and t-test based step-finding analysis. *Methods* **105**, 119 (Aug 1, 2016).
102. P. Janscak *et al.*, Characterization and mutational analysis of the RecQ core of the bloom syndrome protein. *J Mol Biol* **330**, 29 (Jun 27, 2003).
103. K. C. Neuman, E. A. Abbondanzieri, S. M. Block, Measurement of the effective focal shift in an optical trap. *Opt Lett* **30**, 1318 (Jun 1, 2005).
104. K. Berg-Sorensen, H. Flyvbjerg, Power spectrum analysis for optical tweezers. *Rev Sci Instrum* **75**, 594 (Mar, 2004).
105. J. Happel, H. Brenner, *Low Reynolds Number Hydrodynamics*. (Nijhoff, The Hague, 1983), pp. 327.
106. E. Schaffer, S. F. Norrelykke, J. Howard, Surface forces and drag coefficients of microspheres near a plane surface measured with optical tweezers. *Langmuir* **23**, 3654 (Mar 27, 2007).
107. M. P. Landry, P. M. McCall, Z. Qi, Y. R. Chemla, Characterization of photoactivated singlet oxygen damage in single-molecule optical trap experiments. *Biophys J* **97**, 2128 (Oct 21, 2009).
108. W. J. Greenleaf, M. T. Woodside, E. A. Abbondanzieri, S. M. Block, Passive all-optical force clamp for high-resolution laser trapping. *Phys Rev Lett* **95**, 208102 (Nov 11, 2005).
109. S. R. Okoniewski, L. Uyetake, T. T. Perkins, Force-activated DNA substrates for probing individual proteins interacting with single-stranded DNA. *Nucleic acids research* **45**, 10775 (Oct 13, 2017).
110. H. Yin *et al.*, Transcription against an Applied Force. *Science* **270**, 1653 (Dec 8, 1995).
111. J. A. Morin *et al.*, Active DNA unwinding dynamics during processive DNA replication. *P Natl Acad Sci USA* **109**, 8115 (May 22, 2012).
112. Z. Qi, R. A. Pugh, M. Spies, Y. R. Chemla, Sequence-dependent base pair stepping dynamics in XPD helicase unwinding. *Elife* **2**, e00334 (May 28, 2013).
113. N. Ribeck, D. L. Kaplan, I. Bruck, O. A. Saleh, DnaB helicase activity is modulated by DNA geometry and force. *Biophys J* **99**, 2170 (Oct 06, 2010).
114. J. Lipfert, D. A. Koster, I. D. Vilfan, S. Hage, N. H. Dekker, Single-molecule magnetic tweezers studies of type IB topoisomerases. *Methods in molecular biology* **582**, 71 (2009).

115. D. H. Paik, V. A. Roskens, T. T. Perkins, Torsionally constrained DNA for single-molecule assays: an efficient, ligation-free method. *Nucleic Acids Res* **41**, e179 (Oct, 2013).
116. A. Candelli *et al.*, A toolbox for generating single-stranded DNA in optical tweezers experiments. *Biopolymers* **99**, 611 (Sep, 2013).
117. J. Morfill *et al.*, B-S transition in short oligonucleotides. *Biophys J* **93**, 2400 (Oct 01, 2007).
118. T. Odijk, Stiff Chains and Filaments under Tension. *Macromolecules* **28**, 7016 (Sep 25, 1995).
119. J. K. Karow, R. K. Chakraverty, I. D. Hickson, The Bloom's syndrome gene product is a 3'-5' DNA helicase. *The Journal of biological chemistry* **272**, 30611 (Dec 5, 1997).
120. M. J. Comstock *et al.*, Direct observation of structure-function relationship in a nucleic acid-processing enzyme. *Science* **348**, 352 (Apr 17, 2015).
121. P. H. von Hippel, O. G. Berg, Facilitated target location in biological systems. *The Journal of biological chemistry* **264**, 675 (Jan 15, 1989).
122. M. Manosas, X. G. Xi, D. Bensimon, V. Croquette, Active and passive mechanisms of helicases. *Nucleic Acids Research* **38**, 5518 (Sep, 2010).
123. K. C. Neuman, E. A. Abbondanzieri, R. Landick, J. Gelles, S. M. Block, Ubiquitous transcriptional pausing is independent of RNA polymerase backtracking. *Cell* **115**, 437 (Nov 14, 2003).
124. B. Liu, R. J. Baskin, S. C. Kowalczykowski, DNA unwinding heterogeneity by RecBCD results from static molecules able to equilibrate. *Nature* **500**, 482 (Aug 22, 2013).
125. A. R. Carter, Y. Seol, T. T. Perkins, Precision Surface-Coupled Optical-Trapping Assay with One-Basepair Resolution. *Biophys J* **96**, 2926 (Apr 8, 2009).
126. K. Sarlos, M. Gyimesi, Z. Kele, M. Kovacs, Mechanism of RecQ helicase mechanoenzymatic coupling reveals that the DNA interactions of the ADP-bound enzyme control translocation run terminations. *Nucleic acids research* **43**, 1090 (Jan, 2015).
127. P. M. Burgers, F. Eckstein, A study of the mechanism of DNA polymerase I from *Escherichia coli* with diastereomeric phosphorothioate analogs of deoxyadenosine triphosphate. *The Journal of biological chemistry* **254**, 6889 (Aug 10, 1979).
128. C. Lee, R. J. Suhadolnik, 2',5'-Oligoadenylates chiral at phosphorus: enzymatic synthesis, properties, and biological activities of 2',5'-phosphorothioate trimer and tetramer analogues synthesized from (SP)-ATP alpha S. *Biochemistry* **24**, 551 (Jan 29, 1985).
129. B. Gharizadeh, T. Nordstrom, A. Ahmadian, M. Ronaghi, P. Nyren, Long-read pyrosequencing using pure 2'-deoxyadenosine-5'-O'-(1-thiotriphosphate) Sp-isomer. *Anal Biochem* **301**, 82 (Feb 1, 2002).
130. G. M. Weinstock, K. McEntee, I. R. Lehman, Hydrolysis of nucleoside triphosphates catalyzed by the recA protein of *Escherichia coli*. Hydrolysis of UTP. *The Journal of biological chemistry* **256**, 8856 (Aug 25, 1981).
131. A. K. Vashishtha, J. Wang, W. H. Konigsberg, Different Divalent Cations Alter the Kinetics and Fidelity of DNA Polymerases. *The Journal of biological chemistry* **291**, 20869 (Sep 30, 2016).
132. A. C. Holland, University of Canterbury (1928).

133. T. Dudev, C. Grauffel, C. Lim, How Native and Alien Metal Cations Bind ATP: Implications for Lithium as a Therapeutic Agent. *Scientific reports* **7**, 42377 (Feb 14, 2017).
134. D. Klaue *et al.*, Fork sensing and strand switching control antagonistic activities of RecQ helicases. *Nature communications* **4**, 2024 (2013).
135. Q. Yang, M. Del Campo, A. M. Lambowitz, E. Jankowsky, DEAD-box proteins unwind duplexes by local strand separation. *Molecular cell* **28**, 253 (Oct 26, 2007).
136. E. Jankowsky, M. E. Fairman, RNA helicases--one fold for many functions. *Curr Opin Struct Biol* **17**, 316 (Jun, 2007).
137. M. J. Comstock, T. Ha, Y. R. Chemla, Ultrahigh-resolution optical trap with single-fluorophore sensitivity. *Nat Methods* **8**, 335 (Apr, 2011).
138. M. Hashemi Shabestari, A. E. C. Meijering, W. H. Roos, G. J. L. Wuite, E. J. G. Peterman, Recent Advances in Biological Single-Molecule Applications of Optical Tweezers and Fluorescence Microscopy. *Methods in enzymology* **582**, 85 (2017).

Appendix A

Acronym / Abbreviation Index

%GC	percent guanine-cytosine content
1D, 2D, 3D	one, two, or three dimensional
A	adenine
AC	alternating current
ADC	analog-to-digital converter
ADP	adenosine diphosphate
AFM	atomic force microscopy
AOM	acousto-optic modulator
ASCII	American standard code for information interchange
ATP	adenosine triphosphate
ATP γ S	adenosine 5'-O-(3-thiotriphosphate)
BME	β -mercaptoethanol; 2-mercaptoethanol
BNC	Bayonet Neill–Concelman connector
bp	base pair
BSA	bovine serum albumin
C	cytosine

CAD	computer-assisted design
CCD	charge-coupled device
DAC	digital-to-analog converter
DAQ	data acquisition
DBCO	dibenzocyclooctyl
DC	direct current
DNA	deoxyribonucleic acid
dsDNA	double-stranded DNA
DTT	dithiothreitol
EDTA	ethylenediaminetetraacetic acid
<i>F-x</i>	force-extension
FFT	fast Fourier transform
FJC	freely-jointed chain (e prefix: extensible)
FPGA	field-programmable gate array
FRET	Förster resonance energy transfer
G	guanine
GPIO	general purpose interface bus
GTP	guanidine triphosphate
HRDC	helicase-and-RNaseD–C terminal domain
HSQ	hydrogen silsesquioxane
KOH	potassium hydroxide
LV	LabVIEW
MAX	Measurement & Automation Explorer

MTWB	molecular tweezer wash buffer
MW	molecular weight
NA	numerical aperture
NI	National Instruments
NIH	National Institutes of Health
NIM	nuclear instrumentation module
NPGS	Nanometer Pattern Generation System
NSF	National Science Foundation
nt	nucleotide
OS	overstretching
OT	optical trapping, optical tweezers
PBS	phosphate buffered saline
PBS	polarizing beam splitter
PCA	Protocatechuic acid (3,4 – Dihydroxybenzoic acid)
PCD	P8279 – Protocatechuate 3,4 – Dioxygenase from <i>Pseudomonas sp.</i>
PCI	peripheral component interconnect bus
PCR	polymerase chain reaction
PDB	Protein Database
PEG	polyethylene glycol
PIN	p-type, intrinsic, n-type semiconductor
PIO	parallel input-output
PXI	PCI eXtensions for Instrumentation
PZT	lead zirconate titanate piezo-electric transducer

QPD	quadrant photodiode
RF	radio frequency
RNA	ribonucleic acid
SA	streptavidin
SD	standard deviation
SDS-PAGE	sodium dodecyl sulfate–polyacrylamide gel electrophoresis
SEM	scanning electron microscope
SF	superfamily
SMFS	single-molecule force spectroscopy
S/N	signal-to-noise ratio
SSB	single-stranded DNA binding protein
ssDNA	single-stranded DNA
T	thymine
TEM ₀₀	transverse electromagnetic mode (0,0)
TEV	tobacco etch virus (a source for the associated protease)
TMAH	tetramethylammonium hydroxide
UTP	uridine triphosphate
UV	ultraviolet
VI	virtual instrument
WLC	worm-like chain (e prefix: extensible)

Appendix B

Protocols Index

In this section, I provide some of the common protocols I utilized during my thesis work. They are reproduced in their original formatting for ease-of-use. The components for the bolded buffer solutions used in many are given below.

DNA Dil:	20 mM HEPES pH 7.5, 20 mM KCl, 1 mM Na ⁺ -EDTA pH 8
MES-Tw:	100 mM MES pH 5, 0.3% Tween-20
MTWB-150:	20 mM Tris-HCL pH 7.5, 150 mM NaCl, 0.4% Tween-20
Phos:	81 mM Na ₂ HPO ₄ , 19 mM NaH ₂ PO ₄
Phos-Tw:	Phos with 0.3% Tween-20

Streptavidin to CML beads: Coupling Procedure

CML: Carboxylate Modified Latex

(Based on protocol in Section 14.4.3 of Bioconjugate Techniques, 2nd Ed.)

Buffers:	MES-Tw	Phos	Phos-Tw	
Reagents:	Sulfo-NHS	EDC	BME	1 M Glycine

Notes: Make Sulfo-NHS and EDC solutions fresh every time. Easiest to make two batches at a time. This procedure will take *at least* 7 hours to complete: schedule day appropriately.

Procedure

Prep Beads and SA

1. Take out a new 1 mg bottle of Streptavidin (Vector Lab), so that it can warm up while you work.
2. To a 1.5 mL microfuge tube, add 100-200 μL CML latex beads (~4.0%) and 150 μL **MES-Tw** buffer (200 μL for 750 nm beads; 100 μL for 500 nm beads).

Wash and Sonicate Beads

3. Pipette mix and spin at 14K for 4 min. Take supernatant out, and resuspend in 200 μL **MES-Tw**.
4. Repeat Step 2 two more times, for a total of 3 washes.
5. After resuspending in 200 μL **MES-Tw**, sonicate the beads (sonicate until you complete Steps 6 and 7).

Make Special Solutions

6. Make 0.1 M sulpho-NHS sol. (21 mg/mL). Dissolve 4.2 mg of NHS (in 4 C fridge) in 200 μL **MES-Tw**.
Note: If you measure out more than 4.2 mg, use the ratio $21 \text{ mg} / 1000 \mu\text{L} = M \text{ mg} / V \mu\text{L}$ to find the needed suspension volume V. Do not measure out less than 4.2 mg (for at least 200 μL).
7. Make EDC sol. (5 mg/100 μL). Dissolve 10 mg EDC (-20 C fridge) in 200 μL **MES-Tw**.

Add Special Solutions and Mix

8. End sonication. Add 700 μL **MES-Tw** to the bead solution, for a total volume of 900 μL .
9. Add 100 μL of sulpho-NHS solution to the 900 μL bead solution. Briefly vortex.
10. Add 100 μL of EDC to the 1000 μL bead/ NHS solution. Briefly vortex (*Total volume = 1100 μL*).
11. Put on rotator for 30-45 min at room temperature. Do not exceed 45 minutes.

Quench EDC with BME

12. After rotating, add 1 μL β -mercaptoethanol (BME) to the bead solution (**under the hood**). Briefly vortex and rotate for 10 min at room temp (parafilm the tube first). (*This quenches the rxn of EDC*).

Make SA Solution and Wash Beads Again

13. While the bead sol. rotates, make streptavidin (SA) sol. by adding 1 mL **Phos** to SA bottle. Mix on rotator for 20 min. After rotating, transfer the SA solution to a new 1.5 mL microfuge tube. (*Total SA volume = 1000 μL*).

14. After the bead solution rotates for 10 min, spin down for at least 5 min at 14K. Pull off as much of the supernatant as possible without taking a significant amount of beads.
15. Resuspend beads in 200 μL **Phos-Tw**, and do three 3 minute washes with 200 μL **Phos-Tw**.
16. For final resuspension, bring beads up in 500 μL **Phos-Tw**.
17. *Optional Step:* Add 1 μL beads to 100 μL **Phos-Tw** and flow 20 μL of this solution through flow cell. Check for clumping under a microscope. If clumped, sonicate 8 min or until unclumped.

Add SA Solution and Mix

18. Add beads to SA sol. and quickly mix with pipette (need to monodisperse quickly). Vortex briefly. (Total SA/bead volume = 1500 μL).
19. Place on rotator for at least 2 hours at room temperature. 2 ½ hours is ideal, 4 hours is too much. If desperate and pressed for time, leave in 4 deg C fridge's rotator overnight.

Quench SA-CML Reaction

20. Quench reaction with glycine by adding 30 μL 1 M glycine (MW=75 g/mol). This step is critical.
21. Vortex and let sit on rotator for 10 min at room temperature.

Spin Down and Wash Final Product

22. Spin down sol. for at least 15 minutes at 14K. Extract supernatant and resuspend in 200 μL **Phos-Tw**.
23. Wash 5 times with **Phos-Tw**. Change tubes after 3 washes.
24. For final resuspension bring up in 200 μL **Phos-Tw** (If doing multiple batches, combine all finished batches into one tube). Label final tube and store in 4 deg C fridge.

Cleaning Coverslips

1. Put large stir bar into 1 L washed beaker, zero out on scale, and weigh out 50 g KOH pellets into it (+/- 1 g). Fill beaker with 170 mL EtOH and 80 mL dH₂O. Cover with aluminum foil. Label with contents, initials, and date.
2. Put on the stirrer/hot plate in the fume hood. Mix at 200 rpm until you're done preparing the other components.
3. Load coverslip basket with Corning coverslips, and attach handle (we typically do 3 at a time).
4. Place two 1 L washed beakers ½ full of dH₂O in Branson 5200 sonicating waterbath, as well as KOH solution beaker and a 1 L beaker with ~ 300 mL acetone.
5. Fill water bath 1/4 full with water from sink. Turn on sonicator (but no heat).
6. Using coverslip basket, place coverslips in acetone for 3 min.
7. Rinse over sink with ethanol (remember: alcohol washes alcohol).
8. Place coverslips in KOH solution for 3 min.
9. Rinse coverslips over sink with dH₂O squirt bottle.
10. Place coverslips in beaker of dH₂O in waterbath for 3 minutes. Rinse over sink with dH₂O. Place in other beaker of dH₂O for 3 min. Rinse over sink with dH₂O again.
11. Rinse over sink with ethyl alcohol. Dry in microwave. High power, 2 min.
12. Wash coverslip container with ethanol, remove handle, place coverslips in, and cover with parafilm. Write your initials, the date, and "KOH cleaned" on lid.
13. Repeat steps 6-12 for the rest of the coverslips, changing the ddH₂O in the beakers in the waterbath every three baskets.*
14. Clean-up. Dispose of:
 - dH₂O in sink
 - Acetone in organic hazardous waste (jar is labeled, use funnel)
 - Solution of KOH and alcohol in organic hazardous waste (jar is labeled, use funnel)
 - Empty waterbath in sink (use the plug in its back or just pour out)Put empty beakers, etc. in "needs cleaning" tray

*It's most efficient to parallel process three baskets at a time. Once the first basket is in the KOH, wait no less than 1:30 (less than that and you will hate life as it takes about 90 seconds to get all of the KOH rinsed off the coverslips with a squirt bottle) and start the next basket in acetone.

Making HSQ Post Coverslips

Most important steps: (1) spin coat process [amount of HSQ and introduction speed], (2) correct picoammeter readings, and (3) development process.

1 *Preparation for lithography*

1. Use diamond scribe to mark lower right corner of each coverslip with “P” to indicate post side.
2. KOH clean coverslips.
3. Gather materials needed to spin coat. Bring into clean room if not already there.
 - a. HSQ (FOx16). Acquire from 4 C fridge in B1B12. Take 210 uL/slide in microfuge tubes. Return HSQ bottle to fridge as quickly as possible.
 - b. Coverslips in Teflon rack in box.
 - c. 200 uL pipette.
 - d. Clean room box: contains 200 uL tips, tweezers, and SEM mount.
 - e. Diamond scribe from SEM room.
4. Turn on the spin coater bench’s power and activate its nitrogen ventilation. Turn on the spin coater itself and the hot plate. Heat to 180 C. Place faux-paper towel in front of hot plate.
5. Find usable spin chuck for coverslips and insert into spinner (O-ring on chuck needs to be smaller than coverslip width, so that vacuum suction can hold slip in place).
6. Set spin coater acceleration to 3000 rpm/s, velocity to 2000 rpm, and spin time to 45 s. On newer spin coater, these values are (sometimes) saved in Program 20. On older one, manually turn the dials until the electronic displays show the right values.
7. Place coverslip on chuck with tweezers, and load pipette with 200 uL HSQ. For new model, go into Run Mode, press Vacuum, then Start to start spin. On old model, use foot pedal to start spin.
8. Immediately dispense HSQ onto middle of slip. After 45 s spin, disengage vacuum and remove slip with tweezers.
9. Heat coverslip (dry side down) for 4 min at 180 C.
10. Use diamond scribe to mark an “X” in corner beneath the “P”.
11. Lay finished coverslip on paper towel to cool, then place in rack. Repeat process as necessary.
12. Clean up area, and shut off hot plate, spinner, nitrogen, and bench.

2 *Electron beam lithography*

1. Vent the SEM, and open up the chamber.
2. Install the Helix LVD for LoVac mode. First, vertically slide the aperture up and in, then twist cw until tight. Then slide the chip gently into the slot. Ask David for help if you are unsure.
3. Install mount into SEM. Loosen locking nut with hex wrench if mount pin doesn’t slide in fully. Align so that long edge of mount is parallel to door, and the permanently depressed metal pin is nearest the computer. Tighten until the mount cannot be rotated by hand.
4. Close the chamber door and pump down in LoVac mode (hold door closed until door gap minimizes). Put LVD in 2nd quadrant. If LVD is not an option, detector was not installed properly.
5. While pumping down, open NPGS and go into Matt Bull’s files. On the top bar, select ‘Commands’ and choose ‘Calibrate DACs’.
6. Once pump is done (chamber icon is green), activate 30 kV HV and put spot size at 3-4. Check that Contrast is 60-90 and Brightness is 30-70. Unpause 2nd quadrant.
7. Use the stage panel to move to (0,0). Type values into X and Y boxes, then hit Enter.
8. At ~100x Magnification, manually move stage in XY (click on 1st quad and hold mid mouse button) until you find the inside edge of the mount’s metal washer.
9. Bring stage up in Z to 7-9 mm by clicking on CCD quad and using mid mouse button (can also use Z input box, but only do so when far away from LVD; hitting Esc stops motion).
10. Magnify on washer edge to ~2000x, and change dwell time to ~0.8 μ s. Adjust fine focus knob until image is crisp (striations visible on edge, etc). This will change the listed working distance (WD). Once a good image is obtained, link WD to z-height.
11. Zoom out to ~200x and find the mount’s center. Look for an FIB-ed “X”. Zoom to 2500x, put the quad center cursor over it, and record the XY coordinates in Notepad.

12. Turn off HV, vent the chamber, and open the door. Lower the loading pin and lift the central metal washer. Slide coverslip in, ensuring that the registry corner of the slip (the one with the "P") is in the corner with the two fixed pins. Lower metal washer.
13. Close door and pump down in LoVac mode. Once done, navigate stage to (-10 mm, 18 mm), which should be close to registry corner.
14. Raise the stage to ~5 mm. Activate 30 kV HV and set spot size to 1.8 (or whatever results in 0.800 – 1.100 nA on the picoammeter during the write program's run). Unpause 2nd quad.
15. Move in XY until you find the registry corner (or something easy to focus on). Zoom to ~2000x, and see if you can get a decent image by adjusting fine focus. If not, astigmatism could be really bad.
16. If image is okay, adjust fine focus to 5 mm WD. Raise stage until image is focused. Link WD to z-height.
17. Move off registry mark to featureless area. Zoom in by couple 1000x and look for small marks. Zoom in on one of them, fine focus adjusting as you go for best image quality.
18. At 80000x, fine focus adjust as best you can, then switch to 4x50 ns dwell and Live image (not 4 frame average). On 1st right-hand panel, hit Lens Align modulator button.
 - a. If whole image moves in XY, lens alignment is off. Move Lens box cursor until it stops.
 - b. If image blurs in orthogonal directions, astigmatism present. Move Stig box cursor until it stop.
19. Zoom in to ~120000x, increase dwell to ~1.5 μ s, and fine focus for best image. Then use Stig knobs to improve image as best you can.
20. On 2nd quad, hit pause button. On box left of computer screen, turn knob from "on" to "ext". In NPGS, click "NPGS mode" ("external" appears on quads, indicating switch from SEM to NPGS mode). Check that the picoammeter reads 0. Unpause CCD screen and navigate to center point using XY input boxes.
21. Highlight 2nd quad and unclick beam blank icon.
22. In bullm's folder, select post file "7x7_15umLateral_700nm.RF6". Right click and select "Process run file". Screen will go black. Check that current is now flowing. If not, hit "Esc" twice.
23. Let the program run (~15 min), then turn off HV. Switch back to SEM mode, and change beam blanker box knob back to "on".
24. Vent the chamber and repeat the process as necessary.
25. When finished, uninstall LVD and mount. Close door and pump down in HiVac mode.

3 Development

1. In B1B12, gather three 1 L beakers. Fill two with 500 mL filtered water each.
2. Put the beakers in the fume hood. Fill the third with MF CD-26 solution stored below the hood.
3. Get a timer, and attach a handle to the coverslip rack. Submerge the coverslips in the MF CD-26 solution for 15 min, agitating them gently every 2-3 min.
4. Remove rack, let excess MF CD-26 drip back into beaker, and submerge into water #1 for 3 min.
5. Repeat with water beaker #2.
6. Dry coverslips with nitrogen gas gun.
7. Put MF CD-26 back into its container, and store under the hood.

4 O₂ Plasma Cleaning (optional)

1. Use clean room username and pin to logon to PlasmaStar computer if David's not logged in.
2. Press the big green button.
3. Turn hot water valve (out) 90 degrees ccw and cold water (in) 45 degrees ccw.
4. Open the O₂ tank in valve MF2 by rotating counterclockwise (take care to not open all the way).
5. Open PlasmaStar program. Wait for it to set up. Login: "user" with password "rie".
6. Allow startup to complete. Open door and place coverslips on lower surface. Close door.
7. Select "Recipe management", then "Open recipe". On the prompt, type in "SRO_posts". The full recipe name should auto-fill; select it. Recipe values: MF2 sccm 25, 300 W, and 30 s.
8. When prompted, select "Execute recipe". The recipe will run, and will notify you when it's done.
9. Remove coverslips, close door, and exit Plasmastar program (it will pump down before closing).

Turn off oxygen gas and water valves (turn cw). Press the big red button. Logout if you logged in.

Silane-PEG-Azide Functionalization Protocol

Reagent source: PG2-AZSL-600 (200 mg).

1. Check that enough of each solvent is available: > 500 mL toluene (50 mL isopropanol).
2. UV-irradiate desired coverslips with ozone chamber for 30-45 min.
 - a. Place down large kimwipe in hood. Work over it.
 - b. Place coverslips in large petri dish bottom. Make sure "P" side is up.
 - c. Place dish in chamber, shut, and press power. When time is over, hold button to turn chamber idle.
3. Prepare reagents for silane-PEG-azide (SPA) / toluene solution.
 - a. Gather equipment: *Cylinders*: 100 mL, 10 mL. *Beakers*: (4) mid-sized for toluene / iso stock and waste. *Covers*: Watch glass, petri dish top. Tiny, small, and medium stir bars. Metal spatula.
 - i. **Holder version**: Get holder, glass hook, holder bottom spacer, cut 600 mL beaker
 - b. Fill stock beakers. Keep toluene bottle in hood.
 - c. Condition all equipment 2x. Spatula, 10 mL cylinder, tiny stir bar get isopropanol, all else toluene.
 - d. Set large hot plate to 60°C solution temp. For Talboys, turn the heat knob. For Omega, press Enter (Set), 1 (Plate Temp), temperature number, then Enter.
 - e. Take out SPA aliquot from -20°C freezer. Thaw for ~5 min (moisture condenses if opened cold).
 - f. Calculate the volume needed for 0.15 mg/mL solution ($V = m/0.15$). Should be < 70 mL.
 - i. **Holder version**: Will need 100 mL to cover holder
 - g. Measure 2 mL isopropanol into 10 mL cylinder, then V-2 mL toluene into 100 mL cylinder.
4. Prepare SPA / toluene solution.
 - a. Pour 2 mL isopropanol into SPA aliquot vial. Agitate with spatula to aid dissolving process.
 - b. Put in tiny stir bar, re-cap, and place on hot plate. Stir at 800 rpm for 2 min.
 - c. Pour 2 mL toluene into 10 mL cylinder, then into vial. Stir at 800 rpm, 2 min. Shake to mix better.
 - d. Pour vial into now emptied toluene stock beaker, as well as toluene from 100 mL cylinder. Put in medium stir bar, cover with watch glass, and put on hot plate. Stir at 600 rpm for 5 min.
 - i. **Holder version**: Use 600 mL beaker instead of toluene stock beaker.
5. Remove coverslips from chamber and prepare them for deposition.
 - a. Place petri dish on hot plate. Put small stir bar in middle. Slowly pour SPA solution into dish. Try not to move coverslips. Cover with petri dish top. Spin at 400 rpm.
 - i. **Holder version**: Put coverslips into holder. Place Teflon spacer and small stir bar into 600 mL beaker, then place holder. Cover with watch glass, spin at 800 rpm.
6. Let deposition proceed for 30 min.
7. Clean and dry functionalized coverslips.
 - a. Gather (4) 250 mL beakers. Fill toluene into first, isopropanol into second, and deionized water into third and fourth. Fill enough to easily dunk coverslips.
 - i. **Holder version**: Use 1 L beakers instead.
 - b. Use two tweezers to fish out coverslips, then dunk each in the four beakers (20 s each). Transfer through air *very* quickly, as clumps can form otherwise. Put into 10-fold Teflon holder.
 - i. **Holder version**: Dunk entire holder instead of individual coverslips.
 - c. Tape down large kimwipe on counter and turn on N₂ gas.

Dry each coverslip. Once done, cover 10-fold box with parafilm and store at 4°C.

Tethered Bead Assay: DBCO Edition

Buffers: **DNA Dil** **MTWB-150** **PBS 1X**

Procedure

1. Make flow cells and allow epoxy to dry. Make sure functionalized “P” side points inwards.
2. Pre-wash slides with 200 μ L **DNA Dil**.
3. Dilute DNA in **DNA Dil** (~100 pM). Flow 15 μ L DNA per slide.
-- Let sit 30 min in humidity chamber at room temperature (up to 4 h is fine).
4. While DNA incubates, prepare 15 μ L SA-coated beads per slide.
 - A. Briefly vortex SA bead stock.
 - B. To 1.5 mL tube, add 0.5 μ L bead stock.
 - C. Add 100 μ L **MTWB-150**. Centrifuge for 5 min at 14 krpm and remove supernatant.
 - D. Resuspend in 50 μ L **MTWB-150** and transfer to a 0.5 mL thin-wall tube.
 - E. Sonicate ~60 min (~two rounds of program 2 in sonicator).
5. Wash slides with 200 μ L **PBS 1X** and 200 μ L **MTWB-150**.
6. Flow 15 μ L of bead solution into each slide.
-- Let sit 1 h at room temperature in humidity chamber.
7. Wash slides with 400 mL **MTWB-150**.

RecQ Protein Purification

We obtained our RecQ plasmid (RecQ Δ HRDC-TEV- pET-15b) from Keir Neuman and Yeonee Seol at the NIH.

I Transform plasmid into *Rosetta2-DE3 pLys competent cells (E. coli)*

1. Thaw the Rosetta 2 competent cells on ice for 10 min.
2. Add 1-2 μ L of plasmid (~5-50 ng) and mix well by flicking the microcentrifuge tube for about 10 s. Keep on ice undisturbed for 30 min.
3. Transfer the tube to 42 °C for exactly 30 second and then chill on ice for 2 min.
4. Add 500 μ L of SOC recovery media and let shake at 37 °C for 1 h.
5. Spread 100 μ L of this onto LB-agar-ampicillin plate and incubate at 37 °C overnight.
6. The next day, take a single colony from plate and grow up in 5 mL LB with ampicillin overnight.
7. The next day, add 2 mL of this overnight culture to 150 mL of Terrific Broth (Sambrook, CSH, opennetware) with ampicillin and grow for about 2.5 h at 37 °C in a shaker until the OD at 600 nm is ~0.6.
8. Cool culture on ice for 5 min and grow in a shaker at 23 °C for 30 min.
9. Express protein by adding 1 M IPTG to culture (0.2 mM final concentration). Continue growing for 4 h.
10. Pellet bacteria by centrifugation at 6000 g for 30 min. Discard supernatant and store at -80 °C until ready for purification.

II Harvest protein from bacteria (all steps performed at 4 °C)

1. Resuspend bacteria pellet in cold equilibration buffer (20 mM Tris-HCl pH 8.0, 300 mM NaCl, 10% glycerol, 20 mM imidazole, 1 mM beta-mercaptoethanol), with Halt Protease Inhibitor Cocktail (Thermo Scientific 87785).
2. Sonicate lysate in a Branson Digital Sonifer 450 with a 1/8" Branson Microtip 101148062 (six 30 s pulses at 25% amplitude).
3. Centrifuge at 16000 g for 30 min to remove cellular debris.
4. Load supernatant onto two Ni-NTA spin columns (Thermo Fisher PI88224 preequilibrated in equilibration buffer). Mix vigorously to resuspend the Ni-NTA matrix and incubate on a rotator for 30 min.
5. Remove lysate by briefly spinning in a benchtop microcentrifuge. Repeat process until all remaining lysate is exposed to Ni-NTA matrix.
6. Wash Ni-NTA 6 times with 2.5x column bed volume (500 μ L) equilibration buffer on a vacuum manifold.
7. Elute protein from Ni-NTA by adding one bed volume (200 μ L) of elution buffer (equilibration buffer with 500 mM imidazole) and briefly spinning in a benchtop microcentrifuge. The flow thru containing the RecQ was saved. Repeat elution process twice more.
8. Measure elution protein concentrations on a nanodrop at A280. Pool peak fractions and dialyze in equilibration buffer without imidazole (uncleaved MW=61600, A280 ϵ = 47300). Two rounds of dialysis were performed for 2 h at 4 °C with 300 mL.
9. A portion of the fraction was incubated with TEV-his protease (Promega) overnight at 4 °C to cleave off the his-TEV tag.
10. Clean cleaved RecQ by adding 20 mM imidazole to solution and incubating again in a preequilibrated Ni-NTA spin column for 30 min. Keep RecQ-containing lysate after centrifugation. Repeat process once.
11. Dialyze the highly purified RecQ in equilibration buffer with no imidazole as before.
12. Aliquot RecQ, freeze in liquid nitrogen, and store at -80 °C. Verify RecQ size on a 10% SDS-PAGE. Look for band at ~58 kD (cleaved MW=58459, A280 ϵ = 45800).